FACULTY OF ENGINEERING
AND ARCHITECTURE

Frequency-Synchronous Distributed Antenna Systems Enabled by Sigma-Delta-over-Fiber for 5G and Beyond

Chia-Yi Wu

Doctoral dissertation submitted to obtain the academic degree of
Doctor of Electrical Engineering

Supervisors
Prof. Guy Torfs, PhD - Prof. Piet Demeester, PhD
Department of Information Technology
Faculty of Engineering and Architecture, Ghent University

August 2022

GHENT
UNIVERSITY

ISBN 978-94-6355-616-3
NUR 959
Wettelijk depot: D/2022/10.500/57

Members of the Examination Board

Chair

Prof. Em. Luc Taerwe, PhD, Ghent University

Other members entitled to vote

Prof. Johan Bauwelinck, PhD, Ghent University
Prof. Ingrid Moerman, PhD, Ghent University
Prof. Nele Noels, PhD, Ghent University
Prof. Sofie Pollin, PhD, KU Leuven
Prof. Liesbet Van der Perre, PhD, KU Leuven

Supervisors

Prof. Guy Torfs, PhD, Ghent University
Prof. Piet Demeester, PhD, Ghent University

Dankwoord

爸爸，希望你為我驕傲。

To my dad, who always wanted me to pursue a PhD degree.
I hope he would be proud of me.

Without the assistance, guidance, support, and encouragement of many people, it would not have been possible for me to complete my PhD. Before presenting my work of the past five years, I would like to express my gratitude to them.

First of all, I would like to express my gratitude to my supervisors, Prof. Guy Torfs and Prof. Piet Demeester, for the opportunity to start my PhD at IDLab. I would like to thank them for the abundant resources and the opportunities to participate in important projects. I want to thank Prof. Guy Torfs for his guidance and especially for the research freedom he gave me.

I would like to thank the professors from the IDLab Design group, Prof. Johan Bauwelinck, Prof. Xin Yin, and Prof. Peter Ossieur, for all the helpful and/or interesting discussions related to work or life. Prof. Johan Bauwelinck and Prof. Xin Yin, thank you for interviewing me (five years ago) and letting me join IDLab-Design. Also, special thanks to Prof. Peter Ossieur for arranging the equipment for the ECOC demo in Dublin. I would like to thank my professors at National (Yang Ming) Chiao Tung University, Taiwan, Prof. Shyh-Jye Jou and Prof. Feng-Tsun Chien, for the nice reference letters they wrote when I applied for this PhD position. I would also like to thank all the professors who are part of the jury of my doctoral dissertation for their time and valuable comments.

I want to thank all my colleagues and ex-colleagues at IDLab-Design for the nice office atmosphere. The colleagues who worked closely with me, Haolin and Joris, I cannot imagine completing my publications without your help in building the setups. It is difficult to put my appreciation into words and it has always been nice to work within a team instead of working alone. Laurens (José), thank you so much for proofreading several of my papers and my dissertation and for helping me with the confusing submission process patiently. I have learned a lot from you. It was always nice to chat with you while getting coffee. Caro, thank you for the nice PCIe implementation. Hubert, Hannes, and Manolo, thank you for the nice conference experience in Rome—I will always remember that it is (probably) better to buy yoghurt instead of apples for homeless people ;) . Hubert and Laurens (Bogaert), thanks again for helping me with the demo in Dublin.

I want to thank my family and friends.

媽媽，謝謝你一直支持我，讓我做自己。

Thank you, Mama, for being supportive and for letting me be me.
Ming-Syuan and Wei-Hsin, thank you for always being encouraging and being there for me. My best friends and travel mates—Yi-Hsuan, Yi-Ju, and Wan-Yu, thank you for listening to me, replying to my LINE messages, and encouraging me. So many times, I could not stop myself from laughing out loud when reading your messages. My Taiwanese friends in Belgium and the Netherlands—Linda, Justine, and Chin-Yin, it is relaxing to chat with you. I also want to thank my friends from the book club for all the good coffee and amazing discussions we had and going to have.

Most importantly, thank you, Maarten. For proofreading my work and for writing the Dutch summary and for taking over all the housework when I was fully occupied by work. For being supportive from the beginning to the end and for being encouraging when I doubted myself. For always being there for me.

Gent, 2022

Chia-Yi Wu

佳怡

Table of Contents

Dankwoord **v**

Table of contents **vii**

Nederlandstalige Samenvatting **xvii**

English Summary **xxi**

List of Publications **xxv**

1 Introduction **1**
1.1 Future of Wireless Communication Systems 1
1.1.1 Multiple-Input Multiple-Output (MIMO) Technologies 3
1.1.2 Frequency Bands above 24 GHz 5
1.2 Objective of the Work 6
1.3 Outline of the Dissertation 7

I Radio-over-Fiber Technologies **15**

2 Next-Generation Radio Access Networks **17**
2.1 Radio Access Network Evolution 17
2.2 Function Split Options for Next-Generation Radio Access Networks 20
2.3 Radio Access Networks for Cell-Free Massive MIMO 23

3 Radio-over-Fiber Technologies **29**
3.1 Introduction 29
3.1.1 Sigma-Delta ($\Sigma\Delta$) Modulator 30
3.1.2 Legend of Figures 33
3.2 Radio-over-Fiber Downlink 34
3.2.1 Radio-Frequency Signal over Fiber (RFoF) 34

3.2.2 Intermediate-Frequency Signal over Fiber (IFoF) . . . 35
3.2.3 Baseband Signal over Fiber (BBoF) 37
3.3 Radio-over-Fiber Uplink 39
3.4 Comparison 41
3.5 Conclusion 45

II Distributed Antenna Systems (DASs) Enabled by Sigma-Delta-over-Fiber (SDoF) Technologies 53

4 Sigma-Delta RFoF Based DAS for Sub-6 GHz Bands 55
4.1 Introduction 56
4.2 System Architecture and Experimental Methodology 57
4.2.1 SD-RFoF-Based Distributed Antenna System 57
4.2.2 Multi-User MIMO OFDM Signal 60
4.3 Measurement Results 62
4.3.1 Link Performance 62
4.3.2 Distributed MIMO Performance 65
4.3.3 Impact of Frequency Asynchronism 68
4.4 Conclusion 69

5 Sigma-Delta IFoF Based DAS for the 28 GHz Bands 75
5.1 Introduction 76
5.2 System Architecture and Experimental Methodology 77
5.2.1 SD-IFoF-Based Distributed Antenna System 77
5.2.2 Multiple-Input Single-Output OFDM Signals 82
5.3 Measurement Results 82
5.3.1 Link Performance 83
5.3.2 Remote Radio Unit Synchronism 84
5.3.3 Distributed Multiple-Input Single-Output Performance 85
5.3.4 Impact of Asynchronous Phase Noise 88
5.4 Conclusion 89

6 Bit-Interleaved SDoF Based DAS for Sub-6 GHz Bands 95
6.1 Introduction 96
6.2 System Architecture 98
6.2.1 Downlink Data Path 100
6.2.2 Uplink Data Path 101
6.2.3 Synchronization Circuit 101
6.3 Experimental Methodology and Measurement Results 102

6.3.1 Link Performance 102
6.3.2 Remote Radio Unit Synchronism 104
6.3.2.1 Jitter Measurement 105
6.3.2.2 Spectrum Measurement 106
6.3.2.3 Phase Difference Measurement 109
6.3.3 Single-Input Multiple-Output Uplink Performance . . 112
6.3.4 Multiple-Input Single-Output Downlink Performance . 113
6.4 Conclusion 113

III Impacts of Asynchronous Phase Noise on Distributed Antenna Systems (DASs) 117

7 Impacts of Asynchronous Phase Noise on DASs 119
7.1 Introduction 119
7.2 Impact of Inaccurate Digital Beamforming Phases 120
7.3 DAS Exploiting Time-Division Duplex (TDD) Reciprocity . . 123
7.3.1 Exact versus Relative TDD Reciprocity Calibration . . 123
7.3.2 Challenges for DASs 125
7.3.3 Workflow 126
7.4 Experimental Methodology and Results 128
7.4.1 Calibration Coefficient Stability 128
7.4.2 Precoding Accuracy 132
7.4.3 DAS Performance Stability 136
7.5 Conclusion 138

8 Conclusions 141
8.1 Summary of the Results 141
8.2 Future Work 143

A OFDM Signals 149
A.1 Signal Parameters 149
A.2 Frequency-Interleaved OFDM Signals 150

B Error Vector Magnitude (EVM) 155

C Derivation of the Expectation of $cos(\phi)$ for $\phi \sim \mathcal{N}(0, \sigma_\phi^2)$ 157

D Impact of Inaccurate Precoding Phases on a 2-by-2 Multi-User MIMO System 161

Glossary

Symbols

$\Sigma\Delta$	sigma-delta
3GPP	3rd Generation Partnership Project

A

ADC	analog-to-digital converter
ARoF	analog radio-over-fiber
ASIC	application-specific integrated circuit
AWG	arbitrary waveform generator
AWGN	additive white Gaussian noise

B

BBoF	baseband signal over fiber
BBU	baseband unit
BER	bit-error rate
BPF	band-pass filter
bps	bit per second

C

C-RAN	centralized radio access network
CDR	clock-and-data recovery module
CFO	carrier frequency offset

CFR	channel frequency response
CoMP	coordinated multi-point
CP	cyclic prefix
CPRI	Common Public Radio Interface
CPU	central processing unit
CSI	channel state information
CU	central unit

D

DAC	digital-to-analog converter
DAS	distributed antenna system
DFB	distributed feedback (laser)
DL	downlink
DML	directly modulated laser
DRoF	digitized radio-over-fiber
DSP	digital signal processing
DU	distributed unit

E

eCPRI	enhanced CPRI
EML	externally modulated laser
EVM	error vector magnitude

F

FDD	frequency-division duplex
FFT	fast Fourier transform
FIR	finite impulse response
FPGA	field-programmable gate array

G

Gbps	gigabit per second

GSps	gigasample per second

H

HPF	high-pass filter

I

IF	intermediate frequency
IFFT	inverse fast Fourier transform
IFoF	intermediate-frequency signal over fiber
IIR	infinite impulse response
IMT	International Mobile Telecommunications
IQR	interquartile range
ITU	International Telecommunication Union

L

LNA	low-noise amplifier
LoS	line-of-sight
LPF	low-pass filter
LTE	Long-Term Evolution

M

Mbps	megabit per second
MIMO	multiple-input multiple-output
MISO	multiple-input single-output
MMF	multi-mode fiber
mmWave	millimeter-wave
MSps	megasample per second
MU-MIMO	multi-user MIMO

N

NG-RAN	next-generation radio access network
NGFI	next-generation fronthaul interface
NLoS	non-line-of-sight
NRZ	non-return-to-zero

O

OFDM	orthogonal frequency-division multiplexing
OSR	oversampling ratio

P

PA	power amplifier
PCB	printed circuit board
PCIe	peripheral component interconnect express
PLL	phase lock loop
PRBS	pseudorandom binary sequence
PSD	power spectral density

Q

QAM	quadrature amplitude modulation
QSFP	quad small form-factor pluggable

R

RAN	radio access network
RF	radio frequency
RFoF	radio-frequency signal over fiber
RoF	radio-over-fiber
RRU	remote radio unit
RTO	real-time oscilloscope

S

SDM	sigma-delta modulator
SDoF	sigma-delta-over-fiber
SFP	small form-factor pluggable
SIMO	single-input multiple-output
SISO	single-input single-output
SMF	single-mode fiber
SNR	signal-to-noise ratio
SQNR	signal-to-quantization-noise ratio

T

TDD	time-division duplex

U

UL	uplink

V

VCSEL	vertical-cavity surface-emitting laser

Z

ZF	zero-forcing
ZOH	zero-order hold

Nederlandstalige Samenvatting –Dutch Summary–

De hoeveelheid mobiel dataverkeer is het laatste decennium jaarlijks met 50% tot 100% gegroeid. Streamingdiensten en videorijke toepassingen hebben het mobiel dataverbruik sterk doen toenemen. Een nog hogere groei wordt verwacht door immersieve media zoals virtuele en aangevulde realiteit. De COVID-19-pandemie heeft het belang aangetoond om verbonden te blijven en heeft ook de werkomgeving herschapen. Telewerken is het nieuwe normaal geworden. Telewerk en videoconferentie dragen nog verder bij aan de rijzende vraag naar alom beschikbaar, betrouwbaar internet aan hoge snelheid. Zulke vraag voedt de voortdurende evolutie van communicatiesystemen.

Opeenvolgende generaties van communicatiesystemen zorgen voor steeds grotere uitdagingen om aan performantievereisten te voldoen. *Multiple-input multiple-output* (MIMO) en millimetergolf (mmWave) technologieën zijn twee technieken die het mogelijk maken om te voldoen aan de beoogde piekdatasnelheid, de door elke gebruiker ervaren datasnelheid, kanaalcapaciteit en spectrale efficiëntie. Deze activerende technologieën vereisen aanpassingen aan de architectuur van de huidige radiotoegangsnetwerken (RAN). Meer informatie over deze twee technologieën is te vinden in hoofdstuk 1.

Dit werk bouwt voort op het onderzoek van de IDLab Design groep naar *sigma-delta-over-fiber* (SDoF) technologieën, en biedt enkele mogelijke oplossingen voor RANs gebaseerd op *radio-over-fiber* (RoF). De focus ligt in het bijzonder op de combinatie van SDoF-technologieën en gedistribueerde antennesystemen. Drie verschillende prototypes voor uiteenlopende scenario's worden voorgesteld in dit werk.

Het eerste deel van dit proefschrift beschrijft de evolutie van RANs en vergelijkt enkele RoF technologieën. Hoofdstuk 2 begint met een historisch overzicht van deze evolutie. Voor 4G werden gecentraliseerde of *cloud* RANs (C-RANs) ontwikkeld. In C-RANs worden meerdere basisbandeenheden, die basisbandsignalen aanmaken om te verzenden en ontvangen basisbandsigna-

len verwerken, samen geplaatst in één centrale eenheid. Als gevolg hiervan kunnen de afgezonderde eenheden eenvoudiger worden en beperkt worden tot voornamelijk analoge en hoogfrequente hardware. Data tussen de centrale eenheid en de bijhorende afgezonderde eenheden wordt verzonden via het *fronthaul* netwerk, dat vaak wordt geïmplementeerd met gedigitaliseerde RoF (DRoF) technologieën. Voor de *downlink* verbinding (van een basisstation naar een gebruiker) voorziet het fronthaul netwerk de basisbandsignalen voor alle zenders van de afgezonderde eenheid. Voor de *uplink* verbinding (van een gebruiker naar een basisstation) worden de basisbandsignalen van alle ontvangers in de afgezonderde eenheid teruggestuurd naar de centrale eenheid via het fronthaul netwerk. Het fronthaul dataverkeer van C-RANs stijgt evenredig met het aantal zender-ontvangers. Omwille van de voor 5G beloofde massale MIMO-technologieën (MIMO met meer zenders en ontvangers) werd de evolutie naar *next-generation* RANs (NG-RANs) ingezet om zulke groei aan dataverkeer te vermijden.

Er is al veel onderzoek gedaan naar analoge RoF (ARoF) en SDoF-technologieën voor de fronthaul netwerken van NG-RANs. DRoF blijft echter in gebruik voor 5G NG-RANs. De nieuwe DRoF-architectuur kan het dataverkeer voor massale MIMO-technologieën aan, maar ten koste van complexere afgezonderde eenheden. Hoofstuk 3 geeft een overzicht en vergelijking van deze RoF-technologieën.

Met de commercialisering van 5G begon ook het onderzoek naar 6G. Gedistribueerde massale MIMO (ook gekend als celvrije massale MIMO) combineert de gedistribueerde plaatsing van groot aantal zender-ontvangers. In een gedistribueerd massaal MIMO-systeem werken alle afzonderlijk geplaatste zender-ontvangers samen om alle gebruikers binnen hun gezamelijke netwerkdekkingsgebied te bedienen. De gedistribueerde opstelling verhoogt de ruimtelijke diversiteit en daarmee ook de kanaalcapaciteit. Centrale architecturen maken het intuïtief eenvoudiger om zender-ontvangers te coördineren. In plaats van een beperkt aantal afgezonderde eenheden met elk een grote hoeveelheid zender-ontvangers wordt een opstelling verwacht met meer afgezonderde eenheden met elk minder zender-ontvangers. Anticiperend op deze toename genieten ongecompliceerde afgezonderde eenheden dus weer de voorkeur.

Deze nieuwe ontwerpoverwegingen kunnen de start betekenen van een nieuwe evolutie van RANs. SDoF-technologieën zijn hierbij volgens ons zeker haalbaar. SDoF-technologieën zijn interessant vanwege de soepelere voorwaarden die ze stellen aan de lineariteit van de componenten, de hoge tolerantie tegen bitfouten en de mogelijkheid tot eenvoudige afgezonderde eenheden. Ze bieden meer marge in de afweging tussen efficiëntie van de optische bitsnelheid en

complexiteit van afgezonderde eenheden. Gecombineerd met gedistribueerde antennesystemen bieden SDoFs nog enkele bijkomende voordelen: de architecturen zijn meer gecentraliseerd en vereenvoudigen daarom de coördinatie tussen afgezonderde eenheden. Gebruik makende van klok-en-data extractie modules kunnen SDoF-architecturen de frequenties van meerdere afgezonderde eenheden synchroniseren. Bovendien garanderen de eenvoudige architecturen constante vertragingverschillen tussen downlink (en uplink) paden van verschillende afgezonderde eenheden.

Het tweede deel geeft een uiteenzetting van drie gedistribueerde antennesystemen die gebruik maken van SDoF. Alledrie de hoofdstukken demonstreren de goede signaalkwaliteit en frequentiesynchroniciteit van SDoF-verbindingen.

Hoofdstuk 4 beschrijft een gedistribueerd antennesysteem met twee antennes voor de 3,5 GHz-band. De architectuur is extreem gecentraliseerd. Door de downlinksignalen aan de centrale eenheid te upconverteren naar hoge frequenties worden de afgezonderde eenheden volledig gesynchroniseerd wat betreft hun (transmissie)tijd, frequentie en fase. De vergelijking met een *single-input single-output* (SISO) scenario vertoont weinig tot geen prestatievermindering in het geval van de 2×2 multi-gebruiker MIMO-transmissie, wat een verdubbelde draadloze kanaalcapaciteit impliceert. De architectuur is in staat om de kanaalcapaciteit te verhogen voor hotspot scenario's. Bovendien zijn door de gecentraliseerde architectuur de afgezonderde eenheden erg eenvoudig en energie-efficiënt.

Hoofdstuk 5 past het gedistribueerde antennesysteem van hoofdstuk 4 aan om toepassingen in de 28 GHz-band mogelijk te maken. Bij deze architectuur worden sigma-delta gemoduleerde basisbandsignalen upgeconverteerd naar een tussenliggende frequentie om vervolgens te worden verzonden over optische vezel. Elke afgezonderde eenheid maakt gebruik van een klok-en-data extractie module om de informatie van de klok te herkrijgen die vervat zit in de downlink *non-return-to-zero* (NRZ) bitstroom. Hierdoor wordt de synchroniciteit van frequenties tussen afgezonderde eenheden gegarandeerd zonder bijkomend referentiekloksignaal. Complexere afgezonderde eenheden verschaffen twee voordelen: een verbeterde efficiëntie van de optische bitsnelheid en een flexibelere draagfrequentie. De 2×1 transmissie met digitale bundelvorming toont aan dat de twee antennes zorgen voor een antennewinst en dat de gedistribueerde opstelling het bereik verbetert. De upconvertors (die naar de millimetergolffrequentie upconverteren) in de afgezonderde eenheden introduceren echter een asynchrone faseruis. Dit resulteert in een merkbare degradatie van de nauwkeurigheid van de bundelvorming.

De focus van hoofdstuk 6 ligt op schaalbaarheid, zowel van het aantal afgezonderde eenheden als van het aantal zender-ontvangers per afgezonderde eenheid. De sigma-delta gemoduleerde basisbandsignalen zijn in de tijd verweven, zodat elke optische vezel signalen kan verzenden of ontvangen van meerdere antennes. De architectuur is bijgevolg beter schaalbaar naar celvrije massale MIMO. Teneinde de frequenties van de afgezonderde eenheden te synchroniseren gebruikt deze architectuur ook klok-en-data extractie modules. Er is hierdoor geen bijkomend referentiekloksignaal nodig. De experimentele resultaten laten een goede signaalkwaliteit zien voor zowel downlink als uplink.

Het laatste deel (hoofdstuk 7) gaat de impact van asynchroniciteit na. Weinig gedistribueerde antennesystemen kunnen alle soorten van asynchroniciteit (in frequentie, tijd en fase) vermijden. Het hoofdstuk begint met een afleiding van het verwachte verlies in performantie vanwege inaccurate bundelvormingfasen, en gebruikt de 2×1 digitale bundelvorming transmissie als voorbeeld. Vervolgens wordt *time-division duplex* (TDD) wederzijdse kalibratie geïntroduceerd, een belangrijke techniek voor massale MIMO-systemen. Het belang van deze kalibratie en de impact op tijd- en fase-asynchroniciteit worden bevestigd door het resultaat van zowel simulaties als metingen. Uit de experimentele resultaten blijkt dat de opstelling van hoofdstuk 6 geen frequente TDD wederzijdse kalibratie vereist. Zulke stabiliteit maakt het een goede kandidaat voor celvrije massale MIMO-netwerken.

English Summary

Mobile data traffic volume has been growing 50% to 100% yearly over the last decade. Streaming services and video-rich applications have been driving up mobile data usage. Higher growth owing to immersive consumer services using virtual reality or augmented reality is predicted. The COVID-19 pandemic demonstrated the importance of staying connected. It has also reshaped the work ecosystem—teleworking has become the new normal. Teleworking and video conferences further strengthen the burgeoning demands for ubiquitous, reliable, and high-speed internet access. Such demands continuously fuel the evolution of communication systems.

As communication systems evolve from one generation to another, performance requirements become more challenging to reach. Multiple-input multiple-output (MIMO) and millimeter-wave (mmWave) technologies are two main enablers to achieve the expected peak and user-experienced data rates, traffic capacity, and spectral efficiency. These enabling technologies demand the current radio access network (RAN) architecture to evolve. More details on these two technologies are given in Chapter 1.

This work proposes several viable solutions for radio-over-fiber (RoF) based RANs, built upon the research of the IDLab Design group in sigma-delta-over-fiber (SDoF) technologies. It focuses especially on the combination of SDoF technologies and distributed antenna systems. Throughout the work, three different prototype systems have been demonstrated for distinct scenarios.

The first part of the dissertation introduces the RAN evolution and compares several RoF technologies. Chapter 2 starts with the historical background of the evolution. For 4G, centralized or cloud RANs (C-RANs) were proposed and deployed. In C-RANs, several baseband units, which generate the baseband signals for transmission and process the received baseband signals, are aggregated at one central unit. As a result, remote units become simpler and contain mainly analog and radio-frequency hardware. Between a central unit and the remote units it serves, data is transmitted via the fronthaul network, which is often implemented with digitized RoF (DRoF) technologies. For

downlink transmission (from a base station to a user), the baseband signals for all transmitters at a remote unit are provided via the fronthaul network. For uplink transmission (from a user to a base station), the baseband signals from all receivers at a remote unit are sent back to the central unit via the fronthaul network. The fronthaul data traffic of C-RANs grows proportionally to the number of transceivers. As massive MIMO technologies—MIMO with more transmitters or receivers—are promised for 5G, the evolution toward next-generation RANs (NG-RANs) was started in order to avoid the proportionally growing traffic.

There have been many publications about analog RoF (ARoF) and SDoF technologies for the fronthaul networks of NG-RANs. However, DRoF continues to be deployed for 5G NG-RANs. The new DRoF architecture can accommodate the data traffic for massive MIMO technologies at the cost of more complicated remote units. Chapter 3 gives an overview and comparisons of these RoF technologies.

Together with the commercialization of 5G came the dawn of 6G research. Distributed massive MIMO—also branded as cell-free massive MIMO —combines a large number of transceivers with distributed deployment schemes. For a distributed massive MIMO system, all separately located transceivers coordinate to serve all users together within their combined coverage area. The distributed scheme increases the spatial diversity and can therefore increase the channel capacity. Intuitively, centralized architectures are easier to coordinate the transceivers. Instead of having few remote units with a large number of transceivers, a deployment scheme with more remote units having fewer transceivers is expected. Anticipating an increase in the number of remote units, low-complexity remote units are again in favor.

The new design considerations may start another RAN evolution and we consider SDoF technologies highly feasible. SDoF technologies are appealing for their relaxed requirements on device linearities, high tolerance on bit errors, and the possibility of having simple remote units. They provide more freedom for the trade-offs between optical bitrate efficiency and remote unit complexities. When combined with distributed antenna systems, SDoF has some additional benefits: The architectures are more centralized and make the coordination between remote units easier. With clock-and-data recovery modules, SDoF architectures can synchronize the frequencies of multiple remote units. Furthermore, the straightforward architectures guarantee fixed delay differences between the downlink (and uplink) paths of different remote units.

In the second part, three distributed antenna systems enabled by SDoF links are described. The three chapters of this part collectively demonstrate the good signal quality and the frequency synchronism of SDoF links.

Chapter 4 demonstrates a two-antenna distributed antenna system for the 3.5 GHz bands. The architecture is extremely centralized. By up-converting the downlink signals to the radio frequency at a central unit, the remote units are perfectly synchronized in (transmission) time, frequency, and phase. Compared with the single-input single-output (SISO) scenario, the demonstrated 2×2 multi-user MIMO transmission had little performance degradation, implying that the wireless capacity was doubled. The architecture is suitable to increase the channel capacity for hot-spot scenarios. Moreover, the centralized architecture makes the remote units extremely simple and power-efficient.

Chapter 5 modifies the distributed antenna system of Chapter 4 to allow for applications in the 28 GHz bands. For this architecture, sigma-delta modulated baseband signals are up-converted to an intermediate frequency and transmitted over fiber. At each remote unit, the clock information contained in the downlink non-return-to-zero (NRZ) bitstream is retrieved using a clock-and-data recovery module. Thus, the frequency synchronism between remote units is guaranteed with no extra reference clock signal. The more complicated remote units bring two main benefits: improved optical bitrate efficiency and carrier-frequency flexibility. The 2×1 digital beamforming transmission showed that the two antennas provided an antenna gain and the distributed scheme improved the coverage. However, the up-converters (to the mmWave radio frequency) located at the remote units introduced asynchronous phase noise. The loss in the beamforming performance, due to the asynchronous phase noise, is noticeable.

In Chapter 6, we focus on the scalability with respect to both the number of remote units and the number of transceivers per remote unit. The sigma-delta modulated baseband signals are time-interleaved, so each fiber can provide signals to or receive signals from more antennas. The architecture is therefore more scalable toward cell-free massive MIMO. To synchronize the frequencies of remote units, this architecture also uses clock-and-data recovery modules and, therefore, requires no extra reference clock signal. With experimental results, the good signal qualities for both the downlink and uplink have been demonstrated.

The last part (Chapter 7) dives into the impact of asynchronism. Few distributed antenna systems can avoid all types of asynchronism—in frequency, time, and phase—between remote units. Using 2×1 digital beamforming transmission as an example, the chapter begins with the derivation of the expected performance degradation due to inaccurate beamforming phases. The chapter then introduces the time-division duplex (TDD) reciprocity calibration, which is an important process for massive MIMO systems. Through simulation and measurement results, the importance of the calibration and the impacts of time and phase asynchronism have been demonstrated. From the experimental results, the setup proposed in Chapter 6 does not require frequent TDD reciprocity calibration. Such stability makes it a viable candidate for cell-free massive MIMO networks.

List of Publications

Publications in International Journals

1. **Chia-Yi Wu**, Haolin Li, Olivier Caytan, Joris Van Kerrebrouck, Laurens Breyne, Johan Bauwelinck, Piet Demeester, and Guy Torfs, "Distributed Multi-User MIMO Transmission Using Real-Time Sigma-Delta-over-Fiber for Next Generation Fronthaul Interface," *Journal of Lightwave Technology*, vol. 38, no. 4, pp. 705–713, 2020.

2. **Chia-Yi Wu**, Haolin Li, Joris Van Kerrebrouck, Achim Vandierendonck, Igor Lima de Paula, Laurens Breyne, Olivier Caytan, Sam Lemey, Hendrik Rogier, Johan Bauwelinck, Piet Demeester, and Guy Torfs, "Distributed Antenna System Using Sigma-Delta Intermediate-Frequency-over-Fiber for Frequency Bands Above 24 GHz" [Invited], *Journal of Lightwave Technology*, vol. 38, no. 10, pp. 2765–2773, 2020.

3. **Chia-Yi Wu**, Haolin Li, Joris Van Kerrebrouck, Caro Meysmans, Piet Demeester, and Guy Torfs, "A Bit-Interleaved Sigma-Delta-over-Fiber Fronthaul Network for Frequency-Synchronous Distributed Antenna Systems" [Invited], *Applied Sciences*, vol. 11, no. 23, pp. 11471:1–14, 2021.

4. Kasper Van Gasse, Laurens Bogaert, Laurens Breyne, Joris Van Kerrebrouck, Sören Dhoore, Camiel Op de Beeck, Andrew Katumba, **Chia-Yi Wu**, Haolin Li, Jochem Verbist, Abdul Rahim, Amin Abbasi, Bart Moeneclaey, Zhechao Wang, Hongtao Chen, Joris Van Campenhout, Xin Yin, Bart Kuyken, Geert Morthier, Johan Bauwelinck, Guy Torfs, and Günther Roelkens, "Analog Radio-over-Fiber Transceivers Based on III-V-on-Silicon Photonics," in *IEEE Photonics Technology Letters*, vol. 30, no. 21, pp. 1818–1821, 2018.

5. Haolin Li, Laurens Breyne, Joris Van Kerrebrouck, Michiel Verplaetse, **Chia-Yi Wu**, Piet Demeester, and Guy Torfs, "A 21-GS/s Single-Bit

Second-Order Delta-Sigma Modulator for FPGAs," *IEEE Transactions on Circuits and Systems II: Express Briefs*, vol. 66, no. 3, pp. 482–486, 2019.

6. Haolin Li, Johan Bauwelinck, Piet Demeester, Guy Torfs, Michiel Verplaetse, Jochem Verbist, Joris Van Kerrebrouck, Laurens Breyne, **Chia-Yi Wu**, Laurens Bogaert, Bart Moeneclaey, and Xin Yin, "Real-Time 100-GS/s Sigma-Delta Modulator for All-Digital Radio-over-Fiber Transmission," *Journal of Lightwave Technology*, vol. 38, no. 2, pp. 386–393, 2020.

7. Laurens Bogaert, Joris Van Kerrebrouck, Haolin Li, Igor Lima de Paula, Kasper Van Gasse, **Chia-Yi Wu**, Peter Ossieur, Sam Lemey, Hendrik Rogier, Piet Demeester, Günther Roelkens, Johan Bauwelinck, and Guy Torfs, "SiPhotonics/GaAs 28-GHz Transceiver with Reflective EAM for Laser-Less mmWave-over-Fiber," *Journal of Lightwave Technology*, vol. 39, no. 3, pp. 779–786, 2021.

8. Jakob Declercq, Haolin Li, Joris Van Kerrebrouck, Michiel Verplaetse, Hannes Ramon, Laurens Bogaert, Joris Lambrecht, **Chia-Yi Wu**, Laurens Breyne, Olivier Caytan, Sam Lemey, Johan Bauwelinck, Xin Yin, Peter Ossieur, Piet Demeester, Guy Torfs, "Low Power All-Digital Radio-over-Fiber Transmission for 28-GHz Band Using Parallel Electro-Absorption Modulators," *Journal of Lightwave Technology*, vol. 39, no. 4, pp. 1125–1131, 2021.

Publications in International Conferences

1. **Chia-Yi Wu**, Haolin Li, Joris Van Kerrebrouck, Laurens Breyne, Laurens Bogaert, Piet Demeester, and Guy Torfs, "Real-Time 4×3.5 Gbps Sigma Delta Radio-over-Fiber for a Low-Cost 5G C-RAN Downlink," in *Proceedings of the 44th European Conference on Optical Communication (ECOC 2018)*, Rome, Italy, 2018.

2. **Chia-Yi Wu**, Haolin Li, Olivier Caytan, Joris Van Kerrebrouck, Laurens Breyne, Sam Lemey, Hendrik Rogier, Johan Bauwelinck, Piet Demeester, and Guy Torfs, "Distributed MU-MIMO Demonstration Using FPGA-Based Sigma-Delta-over-Fiber" [Best Demo Award], in *Proceedings of the 45th European Conference on Optical Communication (ECOC 2019)*, Dublin, Ireland, 2019.

3. **Chia-Yi Wu**, Caro Meysmans, Haolin Li, Joris Van Kerrebrouck, Olivier Caytan, Sam Lemey, Johan Bauwelinck, Piet Demeester, and Guy Torfs, "Demonstration of a Scalable Distributed Antenna System Using Real-Time Bit-Interleaved Sigma-Delta-over-Fiber Architectures" [Invited Demo], in *Proceedings of the 46th European Conference on Optical Communication (ECOC 2020)*, Brussels (online), Belgium, 2020.

4. Guy Torfs, Haolin Li, Laurens Breyne, Joris Van Kerrebrouck, **Chia-Yi Wu**, Johan Bauwelinck, Piet Wambacq, and Piet Demeester, "Sigma-Delta Modulated Radio over Fiber Transmission" [Invited], in *Proceedings of the 2018 Progress In Electromagnetics Research Symposium (PIERS)*, Toyama, Japan, 2018.

5. Haolin Li, Olivier Caytan, Joris Van Kerrebrouck, Laurens Bogaert, **Chia-Yi Wu**, Laurens Breyne, Johan Bauwelinck, Hendrik Rogier, Piet Demeester, and Guy Torfs, "Sigma-Delta Radio-over-Fiber with Passive Opto-Antenna for Low-Power Short-Reach Optical-Wireless Downlink," in *Proceedings of the 23rd Annual Symposium of the IEEE Photonics Benelux Chapter*, Brussels, Belgium. 2018.

6. Haolin Li, Michiel Verplaetse, Jochem Verbist, Joris Van Kerrebrouck, Laurens Breyne, **Chia-Yi Wu**, Laurens Bogaert, Xin Yin, Johan Bauwelinck, Piet Demeester, and Guy Torfs, "Real-Time 100-GS/s Sigma-Delta All-Digital Radio-over-Fiber Transmitter for 22.75–27.5 GHz Band," in *Proceedings of the 2019 Optical Fiber Communication Conference (OFC)*, San Diego, USA, 2019.

7. Haolin Li, Laurens Breyne, Joris Van Kerrebrouck, Michiel Verplaetse, **Chia-Yi Wu**, Piet Demeester, and Guy Torfs, "A 21-GS/s Single-Bit Second-Order Delta-Sigma Modulator for FPGAs," in *Proceedings of the IEEE International symposium on Circuits and Systems (ISCAS 2019)*, Sapporo, Japan, 2019.

8. Joris Van Kerrebrouck, Laurens Bogaert, Haolin Li, **Chia-Yi Wu**, Piet Demeester, Günther Roelkens, and Guy Torfs, "Monolithically Integrated Quadrature EAM Structure for 28 GHz Full Duplex Radio over Fiber," in *Proceedings of the 24th Annual Symposium of the IEEE Photonics Benelux Chapter*, Amsterdam, the Netherlands, 2019.

9. Haolin Li, Joris Van Kerrebrouck, Hannes Ramon, Laurens Bogaert, Joris Lambrecht, **Chia-Yi Wu**, Laurens Breyne, Jakob Declercq, Jo-

han Bauwelinck, Xin Yin, Peter Ossieur, Piet Demeester, and Guy Torfs, "Low Power All-Digital Radio-over-Fiber Transmission for 28-GHz Band Using Parallel Electro-Absorption Modulators," in *Proceedings of the 2020 Optical Fiber Communication Conference (OFC)*, San Diego, USA, 2020.

Awards

1. The best demo award of the *45th European Conference on Optical Communication (ECOC 2019)*.

1
Introduction

1.1 Future of Wireless Communication Systems

There has been a 50% to 100% yearly growth in mobile data traffic volume over the last decade [1]. Streaming services and video-rich applications, such as mobile gaming, have been driving up mobile data usage. Immersive consumer services using virtual reality (VR) or augmented reality (AR) are expected to lead to even higher growth in the near future.

The COVID-19 pandemic demonstrated the importance of staying connected by boosting the growth of the number of internet users by 10.2% in 2020[1]. It has also reshaped the work ecosystem[2]. Remote working and video conferences further strengthen the burgeoning demands for ubiquitous, reliable, and high-speed internet access.

Such demands have been fueling the evolution of communication systems. As communication systems evolve from one generation to another, expectations for system capacity, energy efficiency, and cost continuously become more challenging to reach [4–8]. Fig. 1.1 summarizes the key capabilities of 4G[3], 5G, and 6G.

[1] In 2021, the growth has returned to 5.8%, in line with pre-crisis rates [2].

[2] In March 2020, only 1 in 67 paid U.S. jobs on LinkedIn offered remote work, but now that number has drastically increased and is up to nearly 1 in 6 [3].

[3] 4G is also known as Long-Term Evolution (LTE).

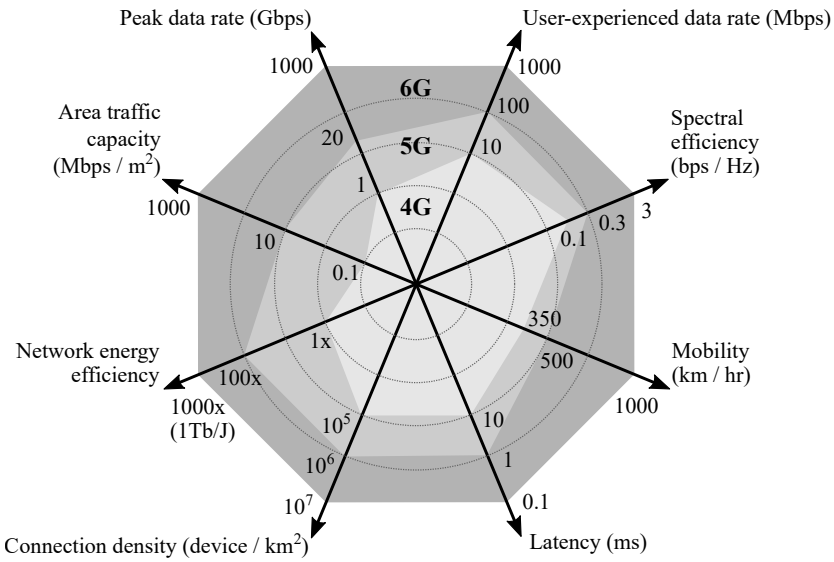

Figure 1.1: Key capabilities of 4G, 5G, and 6G[4].

Among these key performance indicators (KPIs), this work focuses on those that can be achieved by increasing the channel capacity, namely the peak data rate, the user-experienced data rate, and traffic capacity. The channel capacity C, defined by the Shannon-Hartley theorem, is the information rate of data that can be communicated at an arbitrarily low error rate using an average transmitted power P through a channel subject to additive white Gaussian noise (AWGN), whose power spectral density (PSD) is N_0 [9].

$$C = W \log_2 \left(1 + \frac{P}{W\, N_0} \right) \tag{1.1}$$

where W is the signal bandwidth of an ideal band-limited signal. Allocating wider frequency bands, i.e. increasing W, is the most straightforward way to increase the amount of data that can be transmitted. However, radio spectra, especially the frequency bands below 6 GHz, are very scarce resources [7, 10]. This scarcity triggers the advent of millimeter-wave (mmWave) applications.

On the other hand, using the available bands more efficiently is equally important. Therefore, the requirement on (wireless) spectral efficiency, defined as

[4]The key capabilities of 4G and 5G correspond to those of IMT-Advanced and IMT-2020 in FIGURE 3 of [4], respectively. The key capabilities of 6G are listed in TABLE 1 of [6]. The energy efficiency of 6G is expected to improve 10–100 times compared to the one of 5G [8].

the data traffic (bit per second; bps) that can be transmitted over a certain bandwidth (Hz), becomes ever more stringent. Using multiple transmit or receive antennas—multiple-input multiple-output (MIMO)—is the most common way to increase wireless spectral efficiency [11].

Accordingly, MIMO and mmWave technologies are two common methods to achieve the expected peak and user-experienced data rates, traffic capacity, and spectral efficiency.

1.1.1 Multiple-Input Multiple-Output (MIMO) Technologies

MIMO increases wireless spectral efficiency by exploiting spatial diversity, also often referred to as antenna diversity [11]. Both 4G and Wi-Fi[5] support MIMO. Fig. 1.2a is an illustration of a MIMO system with a four-antenna base station. Spatial diversity brings two types of gains: transmit diversity and spatial multiplexing gains [12, 13].

When multiple transmit antennas serve one user simultaneously, the transmitted signals arrive at the user via different wireless paths. Coding techniques such as space-time block codes (STBCs) [11] or space-frequency block codes (SFBCs) [14] can increase the probability that the transmitted signals arrive at the user with a good signal-to-noise ratio (SNR) compared to single-antenna systems. Techniques such as maximum ratio transmission (MRT) [15] can be applied to make the signals combine constructively at the user and therefore improve the received SNR. As the received signal quality improves—owing to the **transmit diversity**, it is possible to increase the data rate for the user, e.g. by using higher-order modulation schemes. A similar gain can be observed when users transmit uplink signals to base stations with multiple receive antennas.

With proper precoding or decoding techniques, the receiving side can distinguish the signals arriving via different wireless paths. Thus, it is possible to transmit different data over the same time-frequency resources for different users (or different receivers of one user) and further increase the overall data traffic. This technique is called **spatial multiplexing**.

Various MIMO technologies have been proposed to further boost the spectral efficiency. Scaling up the number of antennas to massive MIMO (Fig. 1.2 b) is a key technology for 5G [16–19]. With a large number of transmit antennas for downlink or receive antennas for uplink, a massive MIMO system can rely on computationally inexpensive signal processing.

Distributed (and collaborated) MIMO (Fig. 1.2c) can further improve the channel capacity [20]. The distributed scheme allows the signals from the transmit antennas to arrive at a user or the signals from a user to arrive at

[5] Wi-Fi 4 (802.11n) and higher standards.

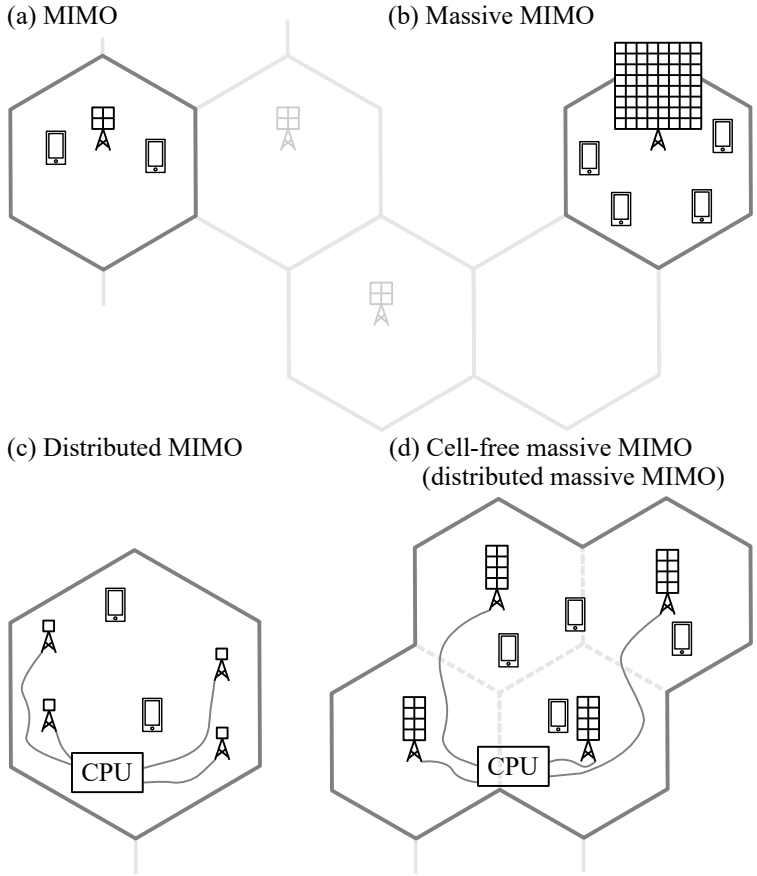

Figure 1.2: Different MIMO technologies. The hexagons[6] illustrate the coverage ranges of the antenna arrays or the sets of distributed and collaborated antennas. (CPU: central processing unit. A CPU processes the signals of the remote sites it serves.)

the receive antennas via more diverse wireless paths. Accordingly, the spatial diversity is increased. Besides, when the line-of-sight (LoS) path between a transmit antenna and a user is blocked, the chance is small that all other transmit antennas are simultaneously blocked [21]. However, synchronization between separately distributed transceivers is not trivial. To coordinate transceivers, extra data needs to be exchanged.

[6]The cells are illustrated as hexagons for aesthetic reasons. The actual coverage areas of mobile signals have organic shapes [22].

Eventually, a combination of both—distributed massive MIMO, also named cell-free massive MIMO—is envisioned for 6G [23, 24]. A large number of antennas are placed separately and operate collaboratively to serve all users as illustrated in Fig. 1.2d. This solution combines the benefits of both the above-mentioned MIMO technologies. Needless to say, the challenges of both technologies need to be overcome: cell-free massive MIMO needs a network that can accommodate the required data traffic and synchronize the remote units.

1.1.2 Frequency Bands above 24 GHz

Due to the scarcity of available bands below 6 GHz and the increasing difficulty to realize international harmonization, it is necessary to seek spectra above 6 GHz [10]. For 5G, the frequency bands between 3 GHz and 4 GHz—the so-called 3.5 GHz bands—and the bands between 24 GHz and 30 GHz—the so-called 26 GHz (in Europe), 28 GHz (worldwide), or mmWave bands—are allocated. The 3.5 GHz and 28 GHz bands correspond to the frequency range 1 (FR1) and the frequency range 2 (FR2) defined by the 3rd Generation Partnership Project (3GPP) [27].

It can be easily observed from Fig. 1.3 that much more frequency bands above 24 GHz are available. There are multiple reasons that these bands lay idle until recently. Compared to sub-6 GHz bands, mmWave bands suffer from larger attenuation over the air [28, 29]. The design of mmWave transceivers is nontrivial [17, 18].

The scarcity of available bands below 6 GHz reflects also on their prices. In the United States, the total net bids for the access licenses in the 3.55–3.65 GHz band (100 MHz) are about 4.5 billion USD (45 million USD per MHz) [30].

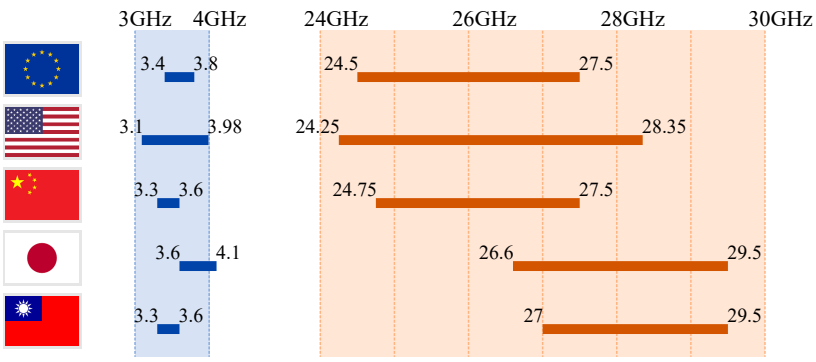

Figure 1.3: The allocated 3.5 GHz and 28 GHz bands for 5G in the EU, the US, China, Japan, and Taiwan. [25, 26].

The 24.25–25.25 GHz (1 GHz) and 27.5–28.35 GHz (850 MHz) bands raised only 2 billion USD (2 million USD per MHz) and 0.7 billion USD (0.8 million USD per MHz), respectively [31, 32].

For 6G, applications for the frequency bands around 60 GHz and even the terahertz bands (0.1–10 THz) are envisioned [7].

1.2 Objective of the Work

MIMO technologies and high-frequency applications bring challenges to the designs of base station transceivers as well as the (fixed) networks that link the base stations, especially the radio access networks (RANs). "RAN" is a collective term for the networks and equipment that connect mobile devices to

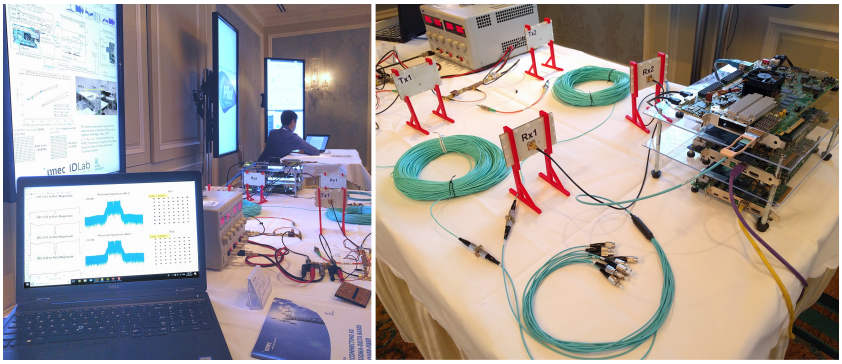

Figure 1.4: Live demonstration of a 2-by-2 multi-user MIMO (MU-MIMO) setup at the 45th ECOC in 2019 [33]. This demonstration won the the Best Demo Award.

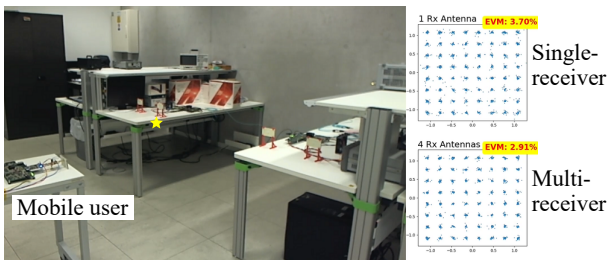

Figure 1.5: Online demonstration (due to the pandemic) of a 4-by-1 distributed antenna system at the 46th ECOC in 2020 [34]. The single-receiver performance is measured by the receiver marked with the yellow star.

core networks, which connect to the data networks, e.g. the internet.

The RAN evolution has started in the 4G era. The centralized RAN (C-RAN) architecture, which aggregates signal processing units at a central unit, has been proposed and deployed for 4G. A central unit serves several remote units, which contain less hardware than traditional non-centralized base stations. It is easier to maintain the co-located signal processing units and to deploy the smaller remote units [35]. It also eases some requirements to coordinate multiple base stations to function as one distributed MIMO system [36].

For 5G, with massive MIMO and mmWave applications, the networks face a large challenge: The data traffic increases considerably because of both the increased number of data streams, which grows proportionally to the number of transmitters or receivers, and the wider signal bandwidths owing to the wide available spectra in the 28 GHz bands. The RANs need to be modified to accommodate the data. To enable cell-free massive MIMO for 6G, the RANs also need to synchronize multiple separately located remote units. Anticipating an increase in the number of remote units, low-complexity remote units are in favor.

This work started with the aim to reshape the network architecture for 5G. It focuses on the combination of radio-over-fiber (RoF) based networks and distributed antenna systems. The main part of this work consists of three implemented prototype systems: a distributed multi-user MIMO (MU-MIMO) system [37], a distributed antenna system for frequency bands above 24 GHz [38], and a distributed antenna system with improved scalability aiming for cell-free massive MIMO [39]. Two prototypes have been demonstrated at the European Conference on Optical Communication (ECOC) (Fig. 1.4 and 1.5). The system performance has been evaluated based on experimental results.

This work was supported by the European Research Council (ERC) Advanced Grant ATTO project (No.695495) [40], EU H2020 5G-PHOS project (No.761989), EU H2020 ERC Proof of Concept Grant BI-SDMoF project (No. 839200), and EU H2020 Int5Gent project (No. 957403) [41].

1.3 Outline of the Dissertation

This dissertation is divided into three parts. Fig. 1.6 shows the outline graphically. The first part of the dissertation is dedicated to radio-over-fiber (RoF) technologies. The second part consists of three chapters based on the three implemented distributed antenna systems (DASs) [37–39]. The last part focuses on the importance of synchronization between remote units.

Chapter 2 describes the evolution of radio access networks (RANs) from 3G to 5G. It focuses specifically on fronthaul networks, which are one of the common use cases of RoF technologies.

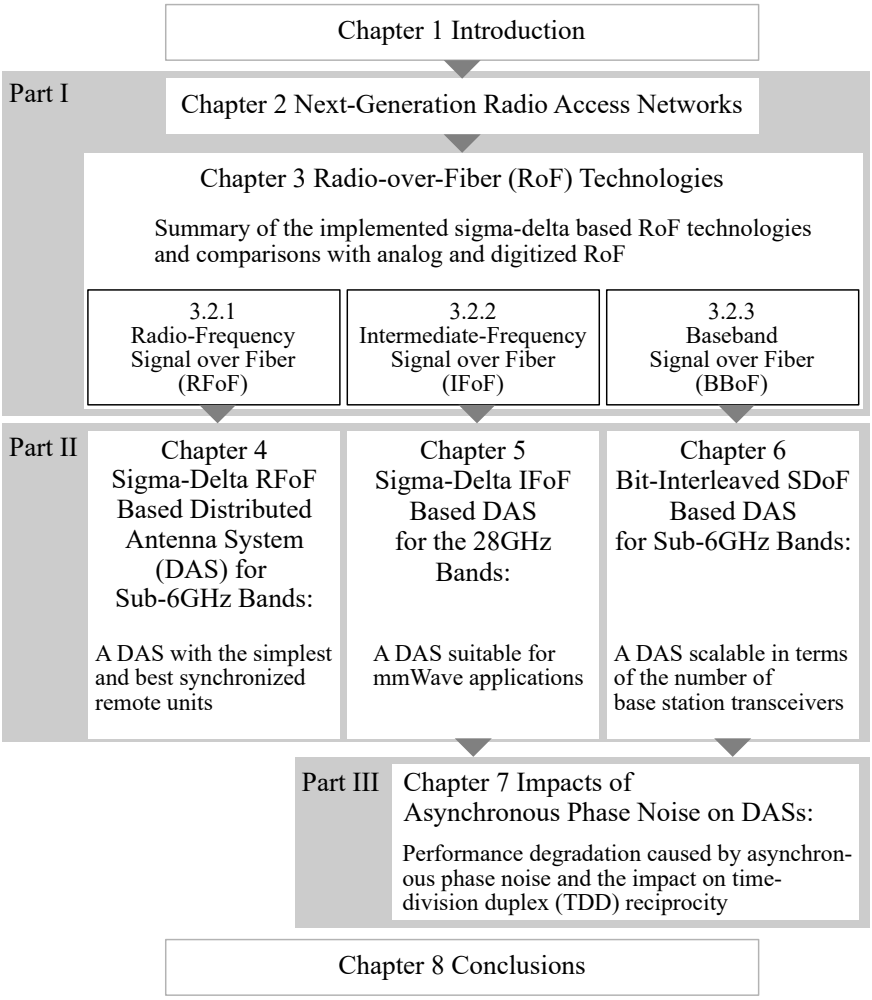

Figure 1.6: Graphical outline of this dissertation.

In Chapter 3, various RoF technologies are divided into three categories based on the carrier frequency of the signals over fiber: radio-frequency signal over fiber (RFoF), intermediate-frequency signal over fiber (IFoF), and baseband signal over fiber (BBoF). For ease of comparison, Chapter 3 groups the three different sigma-delta based RoF technologies that were proposed based on the distinct design considerations of our DASs. Each of the three technologies corresponds to one of the abovementioned categories.

- Sigma-delta RFoF (SD-RFoF): sigma-delta modulated baseband signals are up-converted to the radio frequency and transmitted over fiber. SD-RFoF is the most centralized architecture among the three. It features a simple remote unit architecture.
- Sigma-delta IFoF (SD-IFoF): sigma-delta modulated baseband signals are up-converted to an intermediate frequency and transmitted over fiber. SD-IFoF is more suitable for mmWave applications.
- Bit-interleaved sigma-delta-over-fiber (BI-SDoF): sigma-delta modulated baseband signals are (time-)interleaved and transmitted over fiber. By interleaving multiple signals, each fiber can provide signals to more antennas. The architecture is therefore more suitable for massive MIMO.

Comparisons with analog and digitized RoF are included in this chapter to give an overview of the RAN design trade-offs.

Chapter 4 demonstrates an SD-RFoF based distributed MU-MIMO system for sub-6 GHz bands with the simplest remote units. Chapter 5 proposes an SD-IFoF based DAS for the 28 GHz bands. Chapter 6 focuses on the scalability of the network and proposes the BI-SDoF concept to increase the optical bitrate efficiency; the network architecture is therefore more suitable for cell-free massive MIMO.

The three DASs were implemented collaboratively with my colleagues at IDLab. All DASs use sigma-delta based RoF technologies; the sigma-delta modulators were previously implemented by Dr. Haolin Li [42]. Several printed circuit boards (PCBs) were designed and fabricated for the systems by Dr. Joris Van Kerrebrouck, Dr. Haolin Li, and Dr. Laurens Breyne. The antennas were designed and fabricated by Dr. Olivier Caytan and Mr. Igor Lima de Paula from the EM group of IDLab. My main responsibilities include FPGA design and integration, digital signal processing (MATLAB and Python), and experimental methodology.

As will be briefly discussed in Chapter 5 and Chapter 6, we have observed asynchronous phase noise between remote units. The last part (Chapter 7) discusses the impact of asynchronous phase noise on DASs. It focuses on a 2-by-1 DAS, which has two operating transceivers at the base station and one

user. Both simplified derivations and experimental results are presented. The chapter evaluates the performance of DASs using time-division duplex (TDD) reciprocity in detail since the reciprocity is often exploited in massive MIMO systems [16].

Chapter 8 concludes this work and discusses the possible future research directions.

Four short chapters are included in the appendix. Appendix A summarizes the orthogonal frequency-division multiplexing (OFDM) signal parameters used in this dissertation. Appendix B lists the 3GPP requirements for error vector magnitude (EVM) values and explains the EVM measurement criteria. Appendix C provides the mathematical derivation of an expectation required in Chapter 7. Appendix D extends the derivation in Chapter 7 from a 2-by-1 DAS to a 2-by-2 MU-MIMO system.

References

[1] "Ericsson Mobility Report," 2021, last accessed on Jul. 6, 2022. Available on URL: https://www.ericsson.com/en/reports-and-papers/mobility-report/reports/november-2021

[2] International Telecommunication Union (ITU), "Measuring Digital Development Facts and figures 2021," 2021, last accessed on Jul. 6, 2022. Available on URL: https://www.itu.int/en/ITU-D/Statistics/Documents/facts/FactsFigures2021.pdf

[3] Karin Kimbrough (Chief Economist at LinkedIn), "What Will the World of Work Look Like in 2022? Expect Employees to Remain in the Driver's Seat, Demanding More Out of Work," 2021, last accessed on Jul. 6, 2022. Available on URL: https://www.linkedin.com/pulse/what-world-work-look-like-2022-expect-employees-remain-kimbrough/

[4] International Telecommunication Union (ITU), "IMT Vision – Framework and Overall Objectives of the Future Development of IMT for 2020 and Beyond (ITU-R M.2083-0)," 2015, last accessed on Jul. 6, 2022. Available on URL: https://www.itu.int/dms_pubrec/itu-r/rec/m/R-REC-M.2083-0-201509-I!!PDF-E.pdf

[5] A. Gupta and R. K. Jha, "A Survey of 5G Network: Architecture and Emerging Technologies," *IEEE Access*, vol. 3, pp. 1206–1232, 2015.

[6] I. F. Akyildiz *et al.*, "6G and Beyond: The Future of Wireless Communications Systems," *IEEE Access*, vol. 8, pp. 133 995–134 030, 2020.

[7] The 5G Infrastructure Public Private Partnership (5G PPP), "European Vision for the 6G Network Ecosystem," 2021, last accessed on Jul. 6, 2022. Available on URL: https://5g-ppp.eu/wp-content/uploads/2021/06/WhitePaper-6G-Europe.pdf

[8] R. Bassoli *et al.*, "Why Do We Need 6G?" *ITU Journal on Future and Evolving Technologies*, vol. 2, no. 6, 2021.

[9] J. Proakis and M. Salehi, *Digital Communications*, Chapter 1: Introduction, Fifth ed. McGraw-Hill Education, 2007.

[10] T. Wang *et al.*, "Spectrum Analysis and Regulations for 5G," in *5G Mobile Communications*, W. Xiang *et al.*, Eds. Switzerland: Springer International Publishing, 2017, pp. 27–50.

[11] J. Proakis and M. Salehi, *Digital Communications*, Chapter 15: Multiple-Antenna Systems, Fifth ed. McGraw-Hill Education, 2007.

[12] L. Zheng and D. N. C. Tse, "Diversity and Multiplexing: a Fundamental Tradeoff in Multiple-Antenna Channels," *IEEE Transactions on Information Theory*, vol. 49, no. 5, pp. 1073–1096, 2003.

[13] A. Lozano and N. Jindal, "Transmit Diversity vs. Spatial Multiplexing in Modern MIMO Systems," *IEEE Transactions on Wireless Communications*, vol. 9, no. 1, pp. 186–197, 2010.

[14] H. Bolcskei and A. J. Paulraj, "Space-Frequency Coded Broadband OFDM Systems," in *Proc. 2000 IEEE Wireless Communications and Networking Conference*, vol. 1, 2000, pp. 1–6.

[15] T. L. Marzetta, E. G. Larsson, H. Yang, and H. Q. Ngo, *Fundamentals of Massive MIMO*, First ed. Cambridge, United Kingdom: Cambridge University Press, 2016.

[16] E. G. Larsson *et al.*, "Massive MIMO for Next Generation Wireless Systems," *IEEE Communications Magazine*, vol. 52, no. 2, pp. 186–195, 2014.

[17] F. Boccardi *et al.*, "Five Disruptive Technology Directions for 5G," *IEEE Communications Magazine*, vol. 52, no. 2, pp. 74–80, 2014.

[18] J. G. Andrews *et al.*, "What Will 5G Be?" *IEEE Journal on Selected Areas in Communications*, vol. 32, no. 6, pp. 1065–1082, 2014.

[19] S. Ahmadi, *5G NR*, Chapter 4: New Radio Access Physical Layer Aspects (Part 2), First ed. London, United Kingdom: Academic Press, Elsevier, 2019.

[20] J. Wang and L. Dai, "Asymptotic Rate Analysis of Downlink Multi-User Systems with Co-Located and Distributed Antennas," *IEEE Transactions on Wireless Communications*, vol. 14, no. 6, pp. 3046–3058, 2015.

[21] N. Rajatheva *et al.*, "White Paper on Broadband Connectivity in 6G," 2020, last accessed on Jul. 6, 2022. Available on URL: https://arxiv.org/pdf/2004.14247.pdf

[22] R. Schoenen *et al.*, "Capacity and Coverage Analysis of a 3GPP-LTE Multihop Deployment Scenario," in *Proc. 2008 IEEE International Conference on Communications (ICC) Workshops*, 2008, pp. 31–36.

[23] H. Ngo *et al.*, "Cell-Free Massive MIMO Versus Small Cells," *IEEE Transactions on Wireless Communications*, vol. 16, no. 3, pp. 1834–1850, 2017.

[24] J. Zhang *et al.*, "Cell-Free Massive MIMO: A New Next-Generation Paradigm," *IEEE Access*, vol. 7, pp. 99 878–99 888, 2019.

[25] Qualcomm, "Global Update on Spectrum for 4G & 5G," 2020, last accessed on Jul. 6, 2022. Available on URL: https://www.qualcomm.com/media/documents/files/spectrum-for-4g-and-5g.pdf

[26] National Communications Commission (Taiwan), "NCC Concludes Assignment Stage of 5G Auction," 2020, in Traditional Chinese. Last accessed on Jul. 6, 2022. Available on URL: https://www.ncc.gov.tw/chinese/files/20022/8_42757_200221_1.pdf

[27] "3GPP TS 38.104. New Radio (NR): Base Station (BS) Radio Transmission and Reception (Release 17) (V17.6.0)," June 2022.

[28] T. S. Rappaport *et al.*, "State of the Art in 60-GHz Integrated Circuits and Systems for Wireless Communications," *Proceedings of the IEEE*, vol. 99, no. 8, pp. 1390–1436, 2011.

[29] F. Huang *et al.*, "Propagation Characteristics of Indoor Radio Channel from 3.5 GHz to 28 GHz," in *Proc. 2016 IEEE 84th Vehicular Technology Conference (VTC)*, 2016, pp. 1–5.

[30] Federal Communications Commission, "Wireless Telecommunications Bureau Grants Additional Auction 105 Priority Access Licenses," 2021, last accessed on Jul. 6, 2022. Available on URL: https://www.fcc.gov/auction/105

[31] ——, "Winning Bidders Announced for Auction of 28 GHz Upper Microwave Flexible Use Service Licenses (Auction 101)," 2019, last accessed on Jul. 6, 2022. Available on URL: https://www.fcc.gov/auction/101

[32] ——, "Auction of 24 GHz Upper Microwave Flexible Use Service Licenses Closes Winning Bidders Announced for Auction 102," 2019, last accessed on Jul. 6, 2022. Available on URL: https://www.fcc.gov/auction/102

[33] C.-Y. Wu *et al.*, "Distributed MU-MIMO Demonstration Using FPGA-Based Sigma-Delta-over-Fiber," in *Proc. 45th European Conference on Optical Communication (ECOC 2019)*, 2019, pp. 1–4.

[34] ——, "Demonstration of a Scalable Distributed Antenna System Using Real-Time Bit-Interleaved Sigma-Delta-over-Fiber Architectures," in *Proc. 46th European Conference on Optical Communication (ECOC 2020)*, 2020, pp. 1–4.

[35] A. de la Oliva *et al.*, "An Overview of the CPRI Specification and Its Application to C-RAN-Based LTE Scenarios," *IEEE Communications Magazine*, vol. 54, no. 2, pp. 152–159, 2016.

[36] T. Pfeiffer, "Next Generation Mobile Fronthaul and Midhaul Architectures [Invited]," *Journal of Optical Communications and Networking*, vol. 7, no. 11, pp. B38–B45, 2015.

[37] C.-Y. Wu *et al.*, "Distributed Multi-User MIMO Transmission Using Real-Time Sigma-Delta-over-Fiber for Next Generation Fronthaul Interface," *Journal of Lightwave Technology*, vol. 38, no. 4, pp. 705–713, 2020.

[38] ——, "Distributed Antenna System Using Sigma-Delta Intermediate-Frequency-over-Fiber for Frequency Bands above 24 GHz," *Journal of Lightwave Technology*, vol. 38, no. 10, pp. 2765–2773, 2020.

[39] ——, "A Bit-Interleaved Sigma-Delta-over-Fiber Fronthaul Network for Frequency-Synchronous Distributed Antenna Systems," *Applied Sciences*, no. 23, 2021.

[40] "ATTO: Ultra High Capacity Wireless Networking," last accessed on Jul. 6, 2022. Available on URL: https://atto.ugent.be/

[41] "Int5Gent - EU Project," last accessed on Jul. 6, 2022. Available on URL: https://int5gent.eu/

[42] H. Li *et al.*, "A 21-GS/s Single-Bit Second-Order Delta-Sigma Modulator for FPGAs," *IEEE Transactions on Circuits and Systems II: Express Briefs*, vol. 66, no. 3, pp. 482–486, 2019.

Part I

Radio-over-Fiber Technologies

2

Next-Generation Radio Access Networks

This chapter summarizes the evolution of radio access networks (RANs) and introduces the function split options for the 5G next-generation RANs (NG-RANs). RANs are the main applications that our proposed radio-over-fiber (RoF) technologies target. This chapter intends to provide the background of our research.

2.1 Radio Access Network Evolution

"Radio access network (RAN)" is a collective term for the networks and equipment that connect mobile devices to core networks, which connect to data networks, e.g. the internet. Along with the evolution of communication systems from one generation to the next, RANs have also evolved from the conventional distributed RANs for 3G, the centralized RANs (C-RANs) for 4G, to the next-generation RANs (NG-RANs) for 5G. High-capacity, low-cost, and energy-efficient RANs are always desirable [1, 2].

In the conventional RAN architecture (Fig. 2.1a), each base station contains its baseband unit (BBU), which consists of baseband signal processing hardware. The hardware generates baseband signals for wireless transmission from the data to be transmitted to users, e.g. a picture from a webpage. It also processes / demodulates the received baseband signals, which are sent by

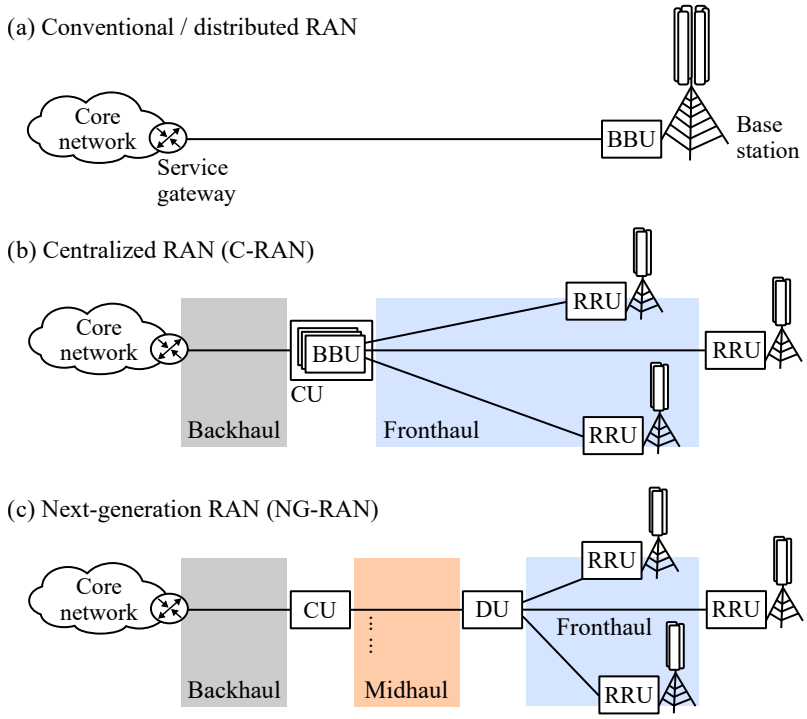

Figure 2.1: Radio access network (RAN) evolution from (a) conventional / distributed RAN, (b) centralized RAN (C-RAN), to (c) next-generation RAN (NG-RAN).

users, back to data. Each base station handles only the mobile data traffic in its coverage area, i.e. its cell.

The centralized architecture, C-RAN, was proposed for 4G [1]. As illustrated in Fig. 2.1b, the BBUs of several base stations are aggregated at one central unit (CU). The remote radio units (RRUs), located with the antennas, contain mainly analog and radio-frequency hardware. The CU generates baseband signals and provides the signals for several RRUs via the fronthaul network. Also, each CU processes the baseband signals received by the RRUs it serves.

In the 4G era, C-RANs have demonstrated several advantages [2, 3]. First of all, with centralization, a large part of hardware can be located in one single room or building and therefore make the deployment and maintenance easier and cheaper. Secondly, smaller RRUs are also easier to install. Moreover, sharing resources, such as cooling systems, can decrease the power consumption considerably.

When the coordinated multipoint (CoMP) concept—coordinating multiple base stations to operate like a distributed multiple-input multiple-output (MIMO) system—was proposed for 4G, the (backhaul or core) network traffic growth due to the extra data for coordination is a large disadvantage [4]. If the CoMP concept is combined with a C-RAN, the coordination can happen at the CU. The additional data required for coordination only need to pass the fronthaul network. As a result, both the latency requirement and the backhaul traffic congestion can be eased [5, 6].

The fronthaul networks need to have enough capacity to transmit the baseband signals to and receive the baseband signals from RRUs. Although the transmit and receive chains of C-RANs are split between CUs and RRUs, they are expected to function as if they are not split. The fronthaul networks should also have little loss. Therefore, the splitting should not introduce too much additional latency to the data paths. RoF technologies are often used for the fronthaul network because of their high capacity, low loss, and low latency [7]. To have multiple RRUs function collaboratively, the RRUs also need to be synchronized in time and frequency [3].

5G aims to have a spectral efficiency threefold the efficiency of 4G: 0.3 bps/Hz versus 0.1 bps/Hz [8]. To further improve wireless spectral efficiency, massive MIMO is expected [9, 10]. However, as will be explained in the next section, the traditional splits of the transmit and receive chains applied in C-RANs struggle to accommodate the data traffic required to enable massive MIMO [11]. The NG-RAN is therefore introduced.

For NG-RANs, the baseband processing functions, which correspond to the BBU blocks in Fig. 2.1b, are redistributed between CUs, distributed units (DUs), and RRUs. Different options to split the baseband functions between the CU, DU, and RRU have been proposed and will be discussed further in the next section. In a 5G NG-RAN (Fig. 2.1c), a CU is connected to several DUs via the midhaul network; each DU serves several RRUs via the fronthaul network.

The terms “distributed unit (DU)” and “remote radio unit (RRU)” are used throughout this dissertation to align with the 5G NG-RAN terminology. It should be noted that the architectures proposed in this work can be deployed for other networks connecting one central site and multiple remote sites, e.g. fiber-to-the-room (FttR) or customized radio access networks for hot spots.

2.2 Function Split Options for Next-Generation Radio Access Networks

For 5G, the 3rd Generation Partnership Project (3GPP) proposed many possible options to split the baseband functions between the CU, DU, and RRU [2, 12, 13]. Fig. 2.2 shows these possible function split options. For the downlink, data packets from the core network are processed by the functions of all layers (top-down) and transmitted by antennas. For the uplink, received signals are processed by the functions of all layers in the reverse order (bottom-up) and eventually form the data packets for the core network.

5G NG-RANs can have different deployment scenarios [14]. Depending on the use cases, a CU and its DUs, or a DU and its RRUs can be co-located. Generally, an NG-RAN may contain: the backhaul network, which connects the CU to the core networks; the midhaul network, which connects the CU and DUs; and the fronthaul network between DUs and RRUs as illustrated in Fig. 2.1c.

Midhaul Network

3GPP decided to split the CU and DU between the packet data convergence protocol (PDCP) and radio link control (RLC) layers [2, 12] (Option 2 in Fig. 2.2). This split option locates all real-time functions at the DU and RRU [15]. Therefore, the midhaul latency requirement can be relaxed if necessary [16].

E.g., for the 5G massive machine-type communication (mMTC) service, the latency requirement is not stringent [8], but a CU may need to coordinate the data to and from a large number of devices. Those devices may connect to different RRUs that are served by different DUs. The DU can spread over a large area. Since the midhaul network does not split any real-time processes, long CU-DU distances are allowed [16].

Fronthaul Network

For 4G C-RANs, fronthaul networks connect CUs and RRUs as illustrated in Fig. 2.1b. For 5G NG-RANs, fronthaul networks connect DUs and RRUs as illustrated in Fig. 2.1c.

Conventionally, the transmit and receive chains are split between the physical (PHY) and radio-frequency (RF) layers (Option 8 in Fig. 2.2) for 4G C-RANs. All function blocks above the dashed line marking Option 8 are located at CUs; the rest is placed at RRUs. The Common Public Radio Interface (CPRI) [17] is used to transmit baseband signals over fiber.

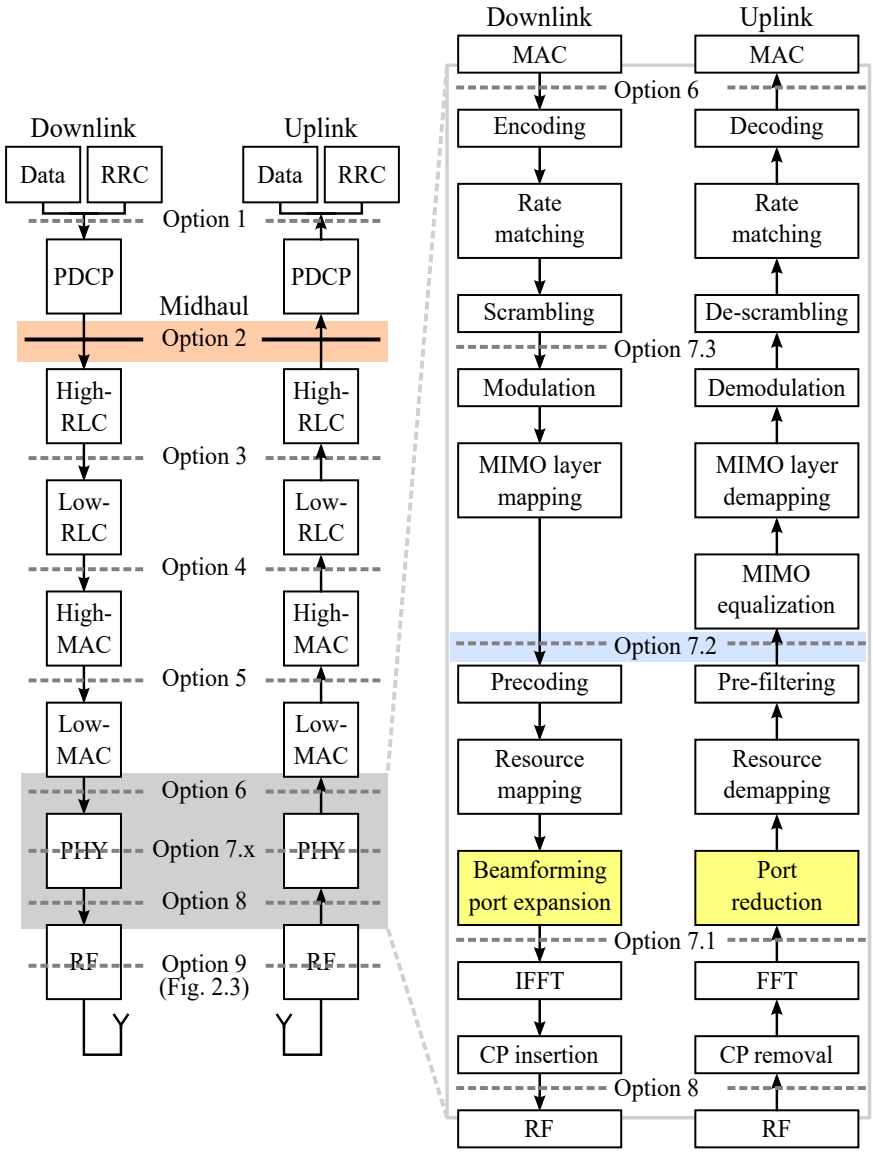

Figure 2.2: Function split options [12, 13]. (RRC: radio resource control; PDCP: packet data convergence protocol layer; RLC: radio link control layer; MAC: medium access control layer; PHY: physical layer; RF: radio-frequency layer; (I)FFT: (inverse) fast Fourier transform; CP: cyclic prefix.)

For downlink transmission, Option 8 leaves the "beamforming port expansion" function block (marked in yellow) at the (4G) CU; for each transmitter (or transmit antenna) at an RRU, a baseband signal needs to be provided via the fronthaul network. for uplink transmission, Option 8 keeps the "port reduction" function block (marked in yellow) at the (4G) CU. from each receiver (or receive antenna) at an RRU, a baseband signal is sent back to the (4G) CU via the fronthaul network. The required bitrate for C-RAN fronthaul networks grows proportionally to the number of transceivers. An example is included in [12]: sending 100 MHz-bandwidth LTE signals with 32 antenna ports requires a bitrate as high as 157.3 Gb/s. The option is obviously not suitable for massive MIMO applications.

When the fronthaul interface for the 5G NG-RANs was still being discussed, two approaches attracted intense interest: (1) intra-PHY layer split options (Option 7.x) with enhanced CPRI (eCPRI) [18]; (2) intra-RF layer split options (Option 9). Intra-PHY split options have been comprehensively discussed in [12] and [18]. Intra-RF split options were first introduced by [13]. As illustrated in Fig. 2.3, both analog and sigma-delta modulated signals centered at different carrier frequencies can be transmitted over the fronthaul networks. The advantages and disadvantages of these options will be further explained in Chapter 3.

As it can be seen from Fig. 2.2, the various options of the two approaches move in opposite directions. Intra-PHY layer split options place more baseband processing functions at the RRUs and result in an architecture more "dis-

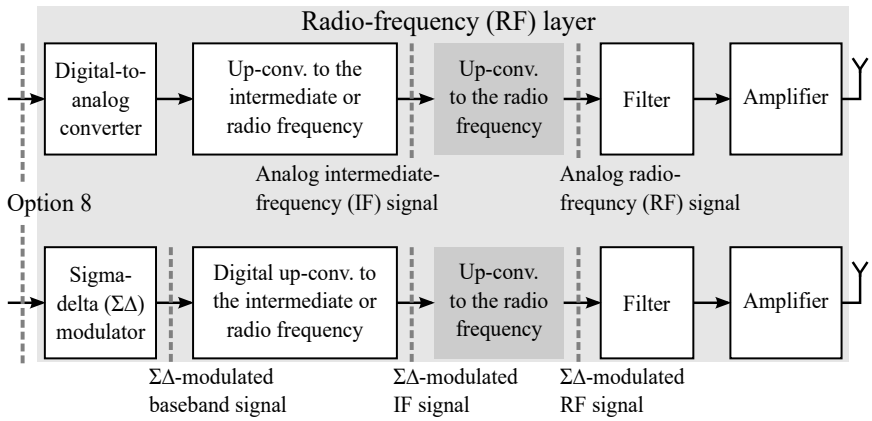

Figure 2.3: Examples of intra-RF function split options (Option 9). The signals transmited over the fronthaul networks can be analog IF / RF signals or sigma-delta ($\Sigma\Delta$) modulated baseband / IF / RF signals.

tributed" than Option 8, in which all PHY-layer functions locate at the DU. Intra-RF layer split options make the architecture even more centralized.

The DU-RRU function split of 5G sub-6 GHz bands eventually converged to Option 7.2 with eCPRI. By moving the precoding block to RRUs, the required bitrate no longer increases proportionally to the number of antennas. This option efficiently decreases the demanded data rate over fiber, however, at the cost of more complicated RRUs.

2.3 Radio Access Networks for Cell-Free Massive MIMO

Together with the commercialization of 5G came the dawn of 6G research. As wireless spectral efficiency became a 6G key performance indicator (KPI) [19], distributed / cell-free massive MIMO has accordingly attracted wide attention. Compared with massive MIMO, cell-free massive MIMO can further improve wireless spectral efficiency owing to the spatial diversity brought by the distributed scheme [20, 21].

Massive MIMO accelerated the RAN evolution from C-RANs to NG-RANs. Cell-free massive MIMO [22] is expected to trigger another evolution.

The distributed MIMO concept is not new. The 4G coordinated multipoint (CoMP) is a type of distributed MIMO system. CoMP coordinates multiple base stations to mitigate the inter-cell interference for the user devices at the cell edges [4]. As a result, the spatial reuse of timeslots or frequency bands relies less on the geographical distances between base stations. The base stations can be placed closer to each other because of the mitigation of inter-cell interference. The increase in the base station density increases the reusability of time-frequency resources and hence improves the spectral efficiency.

Instead of focusing on mitigating inter-cell interferences as 4G CoMP, one of the main goals of distributed / cell-free massive MIMO is to improve spatial diversity by having more multi-paths. Several base stations are coordinated to function as one MIMO system without any cell restrictions—as implied by the new name, "cell-free". All base stations coordinate to serve all users together, instead of only the cell-edge users.

Instead of having few remote units with a large number of transceivers, a deployment scheme with more remote units having fewer transceivers is expected [19], as shown in Fig. 2.4. In this scheme, the RRUs can be made smaller and most of the digital operations are carried out by the central processing unit located at a central site [23], e.g. a DU.

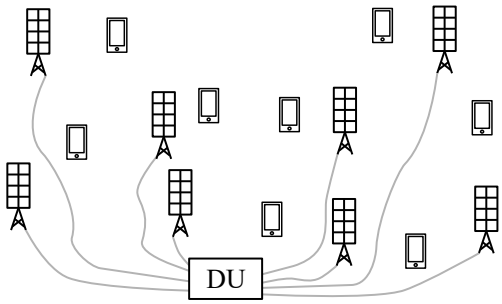

Figure 2.4: Cell-free massive MIMO. (DU: distributed unit (in 5G NG-RAN terminology).)

Certainly, the competent RAN architecture for cell-free MIMO should still have a high-capacity and low-latency fronthaul network. Because cell-free massive MIMO requires the use of a large number of RRUs, low-complexity RRUs are more suitable. Most importantly, the network should provide precise synchronization between different remote units in both time and frequency to enable the coordination [23, 24].

Intra-RF split options have simpler RRU architectures. The more centralized the network architecture, the easier it is to process all signals to and from RRUs together and to guarantee time synchronism. Therefore, we see the potential of intra-RF split options for cell-free massive MIMO. Chapter 3 will introduce several RoF technologies for intra-RF split options and compare their advantages and disadvantages.

References

[1] China Mobile Research Institute, "C-RAN: The Road Towards Green RAN (white paper, version 2.5)," 2011.

[2] C.-L. I *et al.*, "RAN Revolution with NGFI (xhaul) for 5G," *Journal of Lightwave Technology*, vol. 36, no. 2, pp. 541–550, 2018.

[3] A. de la Oliva *et al.*, "An Overview of the CPRI Specification and Its Application to C-RAN-Based LTE Scenarios," *IEEE Communications Magazine*, vol. 54, no. 2, pp. 152–159, 2016.

[4] R. Irmer *et al.*, "Coordinated Multipoint: Concepts, Performance, and Field Trial Results," *IEEE Communications Magazine*, vol. 49, no. 2, pp. 102–111, 2011.

[5] C.-L. I *et al.*, "Recent Progress on C-RAN Centralization and Cloudification," *IEEE Access*, vol. 2, pp. 1030–1039, 2014.

[6] T. Pfeiffer, "Next Generation Mobile Fronthaul and Midhaul Architectures [Invited]," *Journal of Optical Communications and Networking*, vol. 7, no. 11, pp. B38–B45, 2015.

[7] C. Ranaweera *et al.*, "5G C-RAN with Optical Fronthaul: an Analysis from a Deployment Perspective," *Journal of Lightwave Technology*, vol. 36, no. 11, pp. 2059–2068, 2018.

[8] International Telecommunication Union (ITU), "IMT Vision – Framework and Overall Objectives of the Future Development of IMT for 2020 and Beyond (ITU-R M.2083-0)," 2015, last accessed on Jul. 6, 2022. Available on URL: https://www.itu.int/dms_pubrec/itu-r/rec/m/R-REC-M.2083-0-201509-I!!PDF-E.pdf

[9] J. G. Andrews *et al.*, "What Will 5G Be?" *IEEE Journal on Selected Areas in Communications*, vol. 32, no. 6, pp. 1065–1082, 2014.

[10] S. Ahmadi, *5G NR*, Chapter 4: New Radio Access Physical Layer Aspects (Part 2), First ed. London, United Kingdom: Academic Press, Elsevier, 2019.

[11] China Mobile Research Institute, "White Paper of Next Generation Fronthaul Interface (version 1.0)," 2015.

[12] "3GPP TR 38.801. Study on New Radio Access Technology: Radio Access Architecture and Interfaces (Release 14) (V14.0.0)," March 2017.

[13] J. Wang *et al.*, "Delta-Sigma Modulation for Next Generation Fronthaul Interface," *Journal of Lightwave Technology*, vol. 37, no. 12, pp. 2838–2850, 2019.

[14] International Telecommunication Union (ITU), "ITU-T Technical Report on Transport Network Support of IMT-2020/5G," 2018.

[15] L. M. P. Larsen *et al.*, "A Survey of the Functional Splits Proposed for 5G Mobile Crosshaul Networks," *IEEE Communications Surveys & Tutorials*, vol. 21, no. 1, pp. 146–172, 2019.

[16] Y. Tsukamoto *et al.*, "Experimental Evaluation of RAN Slicing Architecture with Flexibly Located Functional Components of Base Station According to Diverse 5G Services," *IEEE Access*, vol. 7, pp. 76 470–76 479, 2019.

[17] "Common Public Radio Interface (CPRI) Specification V7.0," 2015, last accessed on Jul. 6, 2022. Available on URL: http://www.cpri.info/spec.html

[18] "Common Public Radio Interface: eCPRI Interface Specification V2.0," 2019, last accessed on Jul. 6, 2022. Available on URL: http://www.cpri.info/spec.html

[19] I. F. Akyildiz *et al.*, "6G and Beyond: The Future of Wireless Communications Systems," *IEEE Access*, vol. 8, pp. 133 995–134 030, 2020.

[20] R. Ibernon-Fernandez *et al.*, "Comparison Between Measurements and Simulations of Conventional and Distributed MIMO System," *IEEE Antennas and Wireless Propagation Letters*, vol. 7, pp. 546–549, 2008.

[21] I. C. Sezgin *et al.*, "A Low-Complexity Distributed-MIMO Testbed Based on High-Speed Sigma-Delta-over-Fiber," *IEEE Transactions on Microwave Theory and Techniques*, vol. 67, no. 7, pp. 2861–2872, 2019.

[22] H. Ngo *et al.*, "Cell-Free Massive MIMO Versus Small Cells," *IEEE Transactions on Wireless Communications*, vol. 16, no. 3, pp. 1834–1850, 2017.

[23] N. Rajatheva *et al.*, "White Paper on Broadband Connectivity in 6G," 2020, last accessed on Jul. 6, 2022. Available on URL: https://arxiv.org/pdf/2004.14247.pdf

[24] J. Zhang *et al.*, "Cell-Free Massive MIMO: A New Next-Generation Paradigm," *IEEE Access*, vol. 7, pp. 99 878–99 888, 2019.

3
Radio-over-Fiber Technologies

3.1 Introduction

Radio-over-fiber (RoF) technologies are among the most convincing candidates for fronthaul networks owing to their high capacity and low loss [1]. Currently, digitized RoF (DRoF) is often applied for the fronthaul networks of centralized radio access networks (C-RANs). By serializing the baseband signals, DRoF benefits from the non-return-to-zero (NRZ) signals over fiber and has therefore relaxed linearity requirements on both optical and electrical components. However, at remote units, these baseband signals need to be first converted to analog signals and then up-converted to the radio frequency. As a result, the remote unit complexity is high. On the other hand, one of the best attributes of analog RoF (ARoF) is the simple remote unit architecture because the digital-to-analog converters (DACs) are located at the central unit.

Transmitting sigma-delta modulated signals over fiber—sigma-delta-over-fiber (SDoF)—has been proposed as a solution combining both abovementioned advantages of DRoF and ARoF [2]. The bi-level sigma-delta modulated signals can tolerate low device linearities. By filtering the sigma-delta modulated signals, the analog signals can easily be constructed.

Three SDoF-based distributed antenna systems (DASs) construct the main part of this dissertation. Each proposed DAS targets either different wireless frequency bands or different numbers of supported antennas. Because of the distinct design considerations, the applied SDoF technologies differ accord-

ingly. The three applied technologies correspond to the three following categories based on the carrier frequency of the signals over fiber:

1. Radio-frequency signal over fiber (RFoF):
   C.-Y. Wu, H. Li, O. Caytan, *et al.*, "Distributed Multi-User MIMO Transmission Using Real-Time Sigma-Delta-over-Fiber for Next Generation Fronthaul Interface," *Journal of Lightwave Technology*, 2020.

2. Intermediate-frequency signal over fiber (IFoF):
   C.-Y. Wu, H. Li, J. Van Kerrebrouck, *et al.*, "Distributed Antenna System Using Sigma-Delta Intermediate-Frequency-over-Fiber for Frequency Bands Above 24 GHz,", *Journal of Lightwave Technology*, 2020.

3. Baseband signal over fiber (BBoF):
   C.-Y. Wu, H. Li, J. Van Kerrebrouck, *et al.*, "A Bit-Interleaved Sigma-Delta-over-Fiber Fronthaul Network for Frequency-Synchronous Distributed Antenna Systems," *Applied Sciences*, 2021.

For ease of comparison, this chapter summarizes the SDoF architectures and compares each with another RoF technology in the same category.

The chapter starts with an introduction of sigma-delta modulators: how they can encapsulate a multi-bit signal in an NRZ bitstream. Section 3.2 and 3.3 introduce several RoF technologies for downlink (DL) and uplink (UL), respectively. In Section 3.4, we summarize RoF-related publications to give an overview of design trade-offs.

3.1.1 Sigma-Delta ($\Sigma\Delta$) Modulator

A digital sigma-delta modulator (SDM) quantizes the input signal, typically oversampled, to a signal with lower resolution [3]. Fig. 3.1 is the block diagram of a first-order low-pass SDM [4]. The SDM modulates an N-bit input digital signal $x[n]$ into a 1-bit output signal $y[n]$. The 1-bit quantizer transforms the amplitude modulated signal to a pulse-shaped bi-level signal. The introduced quantization noise is denoted as $e[n]$.

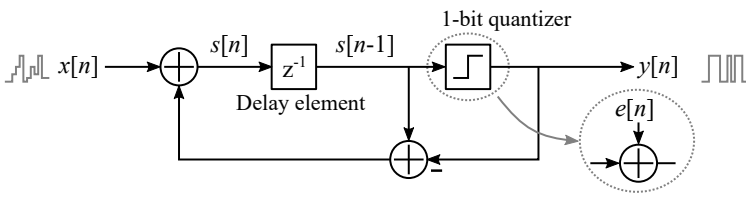

Figure 3.1: Block diagram of a first-order low-pass sigma-delta modulator [4].

We can derive the following equations from the block diagram:

$$y[n] = s[n-1] + e[n]\,. \tag{3.1}$$

$$s[n] = x[n] + s[n-1] - y[n] = x[n] - e[n]\,. \tag{3.2}$$

From Eq. (3.1) and Eq. (3.2), we can express $y[n]$ in $x[n]$ and $e[n]$:

$$y[n] = x[n-1] + e[n] - e[n-1]\,. \tag{3.3}$$

The equation can also be expressed in the Z-domain:

$$Y(z) = \underbrace{(z^{-1})}_{\mathrm{STF}(z)} X(z) + \underbrace{(1 - z^{-1})}_{\mathrm{NTF}(z)} E(z) \tag{3.4}$$

where $X(z)$, $Y(z)$, and $E(z)$ are the Z transforms of $x[n]$, $y[n]$, and $e[n]$, respectively. The signal transfer function, STF(z), only delays the input signal $x[n]$; the waveform of $x[n]$ remains undisturbed. The noise transfer function, NTF(z), is a high-pass filter (HPF). The NTF(z) suppresses the quantization noise at low frequencies where the input signal is located.

The NTFs of higher-order low-pass SDMs are generally expressed as

$$\mathrm{NTF}(z) = (1 - z^{-1})^L \tag{3.5}$$

where L is the SDM order. A higher-order NTF can have a steeper transition. It can provide more quantization noise suppression over the low-frequency signal band and push more noise power to the high frequencies. Thus, the signal-to-quantization-noise ratio (SQNR) in the signal band can be enhanced.

1-bit quantizers are applied since the goal is to encapsulate multi-bit signals into NRZ bitstreams. The maximum in-band SQNR achieved by an Lth-order modulator is given by

$$\begin{aligned}\mathrm{SQNR} = 6.02 + 1.76 - 10\log\left(\frac{\pi^{2L}}{2L+1}\right) \\ + 10\cdot(2L+1)\cdot\log\underbrace{\left(\frac{f_{\Sigma\Delta}/2}{\mathrm{BW}}\right)}_{\text{Oversampling ratio}} \quad (\mathrm{dB})\end{aligned} \tag{3.6}$$

where $f_{\Sigma\Delta}$ is the SDM sample rate and BW is the signal bandwidth [3]. Fig. 3.2 plots the maximum achievable SQNR versus the oversampling ratio (OSR). It is clear that both a higher OSR and a higher order (L) can enhance the SQNR.

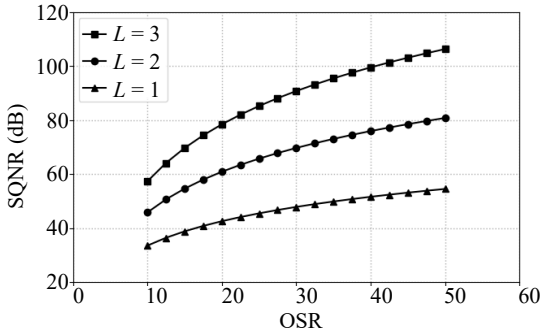

Figure 3.2: The maximum achievable SQNR versus the oversamping ratio.

All experiment setups mentioned in this dissertation use the high-speed second-order low-pass SDMs previously implemented by the IDLab Design group [5]. The real-time SDMs employ the parallel multi-stage scheme [6] to achieve the desired sample rates ($f_{\Sigma\Delta}$) ranging from 3.5 Gbps (gigabits per second) to 7 Gbps; these chosen sample rates are related to the requirements of our proposed setups. Note that the parallel scheme can achieve much higher sample rates. The SDMs used in [7] have a sample rate of 50 Gbps.

Fig. 3.3a illustrates the spectrum and in-phase (I) signal waveform of a 163.84 MHz OFDM baseband signal sampled at 327.68 MSps (megasample

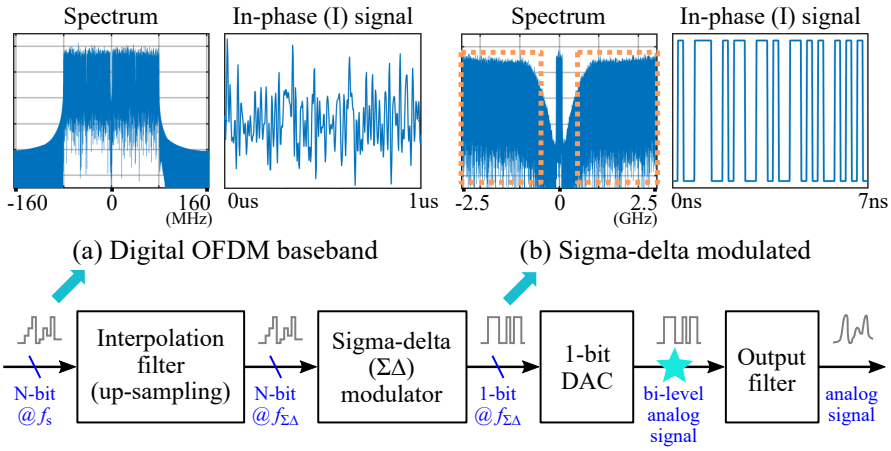

Figure 3.3: The spectra and waveforms of: (a) a 163.84 MHz OFDM baseband signal sampled at 327.68 MSps (f_s); (b) sigma-delta modulated (a) at 4.9152 Gbps ($f_{\Sigma\Delta}$). The lower half is the block diagram of a sigma-delta digital-to-analog converter (DAC).

per second). Fig. 3.3b is the simulated spectrum and I signal of the output of the SDM with a sample rate of 4.9152 Gbps ($f_{\Sigma\Delta}$). It is clear from the spectrum of Fig. 3.3b that the quantization noise, marked by the orange blocks, is pushed to the high frequencies. The bi-level I signal contains the original I signal and the shaped quantization noise. Therefore, by filtering out the quantization noise, the original signal can be reconstructed.

These processes—up-sampling the input digital signals, shaping the quantization noise, and filtering out the shaped quantization noise—also correspond to the hardware of sigma-delta DACs. As illustrated in Fig. 3.3, an interpolator and an SDM form the first part of a sigma-delta DAC [8]. When transmitting sigma-delta modulated signals over the fronthaul networks, the transmit chain splits at the turquoise star in Fig. 3.3. The DU-RRU function split is placed within the process of converting digital signals to analog signals. The part on the left of the star is located at the DUs. The sigma-delta modulated signals over the fronthaul network are bi-level, so the signals are robust against noise and nonlinear distortion. The analog signals contained in the bi-level signals can be easily reconstructed by filtering out the quantization noise at the RRUs.

3.1.2 Legend of Figures

To avoid repetitive explanations of the icons and abbreviations throughout this chapter, Fig. 3.4 shows the legend of all figures in the following sections.

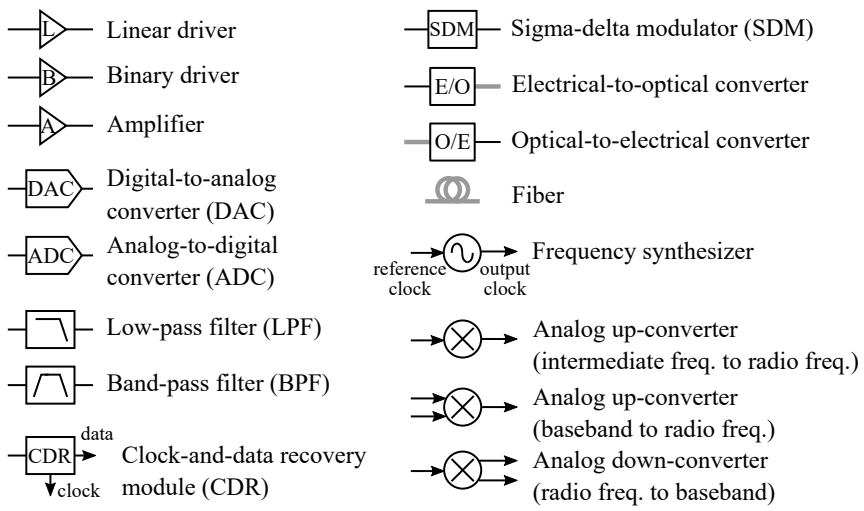

Figure 3.4: Legend of the figures in Chapter 3.

3.2 Radio-over-Fiber Downlink

In each corresponding subsection, an SDoF-based downlink is compared with another commonly used non-SDoF-based technology. Table 3.1 is the overview.

	Radio-frequency (3.2.1)	Intermediate-frequency (3.2.2)	Baseband (3.2.3)
DRoF			×
ARoF	×	×	
SDoF	×	×	×

Table 3.1: Overview of Section 3.2.

3.2.1 Radio-Frequency Signal over Fiber (RFoF)

Radio-frequency signal over fiber (RFoF) architectures centralize most hardware at the DU and benefit from remarkably simple and low-power RRU architectures as illustrated in Fig. 3.5. For both analog RFoF (A-RFoF) (Fig. 3.5a) and sigma-delta modulated RFoF (SD-RFoF) (Fig. 3.5b), the signals are up-converted to the radio frequency at the DUs. Therefore, the synchronization between transmitters, including time, frequency, and phase of the radio-frequency (RF) carrier, is inherently guaranteed—one of the large challenges for distributed multiple-input multiple-output (MIMO) transmission [9]. Distributed MIMO systems using RFoF architectures, e.g. [10, 11], suffer no performance degradation caused by the carrier asynchronism between transmitters. Hence, they need no sophisticated synchronization algorithm.

In addition to the simple RRU architecture, A-RFoF is often preferred for the high optical spectral efficiency, especially for applications with high signal bandwidths. However, the approach often relies on intensity modulation at the sender and direct detection at the receiver (IM-DD) [12]. Although the feasibility of such systems has been demonstrated, they are prone to distortion and non-linearities at both the DU and RRU sides [2]. Besides, the cost of the circuit to operate at high frequencies can be quite high.

In SD-RFoF architectures, the digital baseband in-phase (I) and quadrature (Q) signals are sigma-delta modulated. Then, digital up-conversion [13] is commonly used to convert the bi-level I and Q signals to one (bi-level) RF signal. The digital characteristic loosens the linearity requirements. At RRUs,

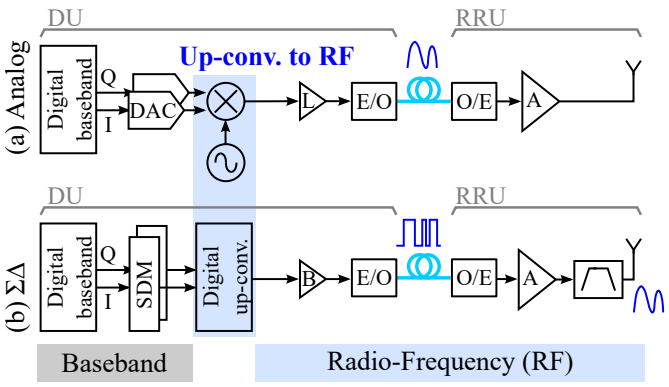

Figure 3.5: Radio-frequency signal over fiber (RFoF): (a) analog (A-RFoF); (b) sigma-delta ($\Sigma\Delta$) modulated (SD-RFoF).

the original analog signals can be easily reconstructed by filtering out the quantization noise.

Despite the advantages and good performance [14, 15], SDoF links are often challenged because the optical bitrate efficiency is not always improved compared to CPRI [16], the commonly used DRoF technology for 4G. Two main reasons limit the bitrate efficiency, defined as

$$\text{bitrate efficiency} = \frac{\text{signal bandwidth (MHz)}}{\text{optical bitrate (Gbps)}}. \tag{3.7}$$

First of all, as mentioned in the previous section, the oversampling ratio (OSR) of sigma-delta modulation directly affects the quality of the modulated signal.

Secondly, when up-converting the signals digitally to the desired carrier frequency at the DU, the bitrate over fiber must equal four times the desired carrier frequency [13]. Although [7] has demonstrated an all-digital SD-RFoF link for the frequency bands above 24 GHz, the required bitrate over fiber seems excessive.

For Sub-6 GHz networks which do not require high optical bitrate efficiency or need simple RRUs, SD-RFoF architectures can be a good candidate. Chapter 4 will introduce our SD-RFoF-based setup [10, 11].

3.2.2 Intermediate-Frequency Signal over Fiber (IFoF)

Two intermediate-frequency signal over fiber (IFoF) architectures—analog IFoF (A-IFoF) and sigma-delta modulated IFoF (SD-IFoF)—are illustrated in Fig. 3.6.

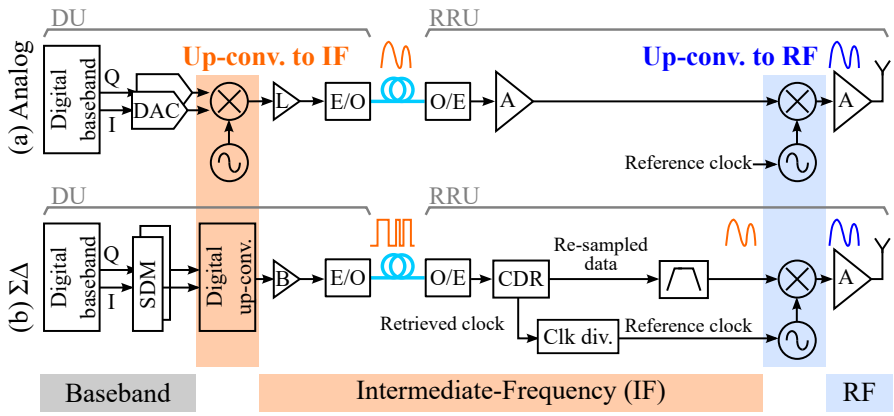

Figure 3.6: Intermediate-frequency signal over fiber (IFoF): (a) analog (A-IFoF); (b) sigma-delta (ΣΔ) modulated (SD-IFoF).

Signals are up-converted to an intermediate frequency at the DUs and then up-converted to the radio frequency at each RRU.

Especially for frequency bands above 24 GHz, A-IFoF can be more advantageous than A-RFoF for two reasons: (1) High-frequency signals suffer more power fading induced by fiber dispersion [17]. (2) The high RF carrier frequency results in the decrease of optical spectral efficiency [18]. While compromising the RRU complexity, A-IFoF architectures relax the hardware requirements at the DU and keep a high optical spectral efficiency [19].

For SD-IFoF, up-converting to the radio frequency at RRUs unbinds the fixed relationship between the carrier frequency and the bitrate over fiber. Therefore, SD-IFoF architectures have an adequately good bitrate efficiency and the carrier frequency can be easily changed by configuring the output frequency of the frequency synthesizer.

Furthermore, the clock information contained in the downlink bitstream can be used for frequency synchronization. As illustrated in Fig. 3.6b, a clock-and-data recovery module (CDR) retrieves the clock information. The retrieved clock signal serves as a reference signal to guarantee the frequency synchronism; hence, no extra reference signal is needed for frequency synchronization. This is an advantage over A-IFoF links, since providing high-quality reference clock signals is not trivial and the clock quality has a large impact on the performance [20]. It is important to mention that, for SD-IFoF, the quality of the retrieved reference clock also has a large impact on the jitter / phase noise of the generated carrier or sample clocks. High-quality CDRs or jitter cleaning circuits are indispensable.

The improved optical bitrate efficiency, however, comes with the cost of

higher RRU complexity. Besides, the oscillators at RRUs introduce asynchronous jitter / phase noise to the system which harms the performance of distributed antenna systems. The impact will be further discussed in Chapter 7. Chapter 5 will describe our SD-IFoF-based setup for the frequency bands above 24 GHz [21].

3.2.3 Baseband Signal over Fiber (BBoF)

Fig. 3.7 illustrates the commonly used RoF technology–digitized (baseband) signal over fiber (DRoF). The digitalized I and Q signals are serialized and transmitted. Common Public Radio Interface (CPRI) [16] and enhanced CPRI (eCPRI) [22] are existing standards for DRoF. Owing to the bi-level characteristic of the signals over fiber, DRoF has high immunity to nonlinearities and noise. However, as discussed in Chapter 2, serializing the signals results in the low optical bitrate efficiency. The RRU complexity is also not suitable to scale up toward distributed / cell-free massive MIMO.

For sigma-delta modulated baseband signal over fiber (SD-BBoF), the serializer is replaced by SDMs and an interleaver (Fig. 3.8). A control sequence can be interleaved together with the I-Q pairs, so it is easier to de-interleave the signals at RRUs and to provide commands from the DU to RRUs. More sigma-delta modulated I-Q pairs can be interleaved into one bi-level signal. In our implementation [23, 24], two I-Q pairs and one control sequence are interleaved into one bitstream. We therefore use the term bit-interleaved sigma-delta-over-fiber (BI-SDoF). At each RRU, the downlink bi-level signal from the DU is de-interleaved back to I_{SD} and Q_{SD} (the sigma-delta modulated I and Q signals).

For both DRoF and SD-BBoF, the clock information contained in the downlink bitstreams can be used for frequency synchronization as SD-IFoF.

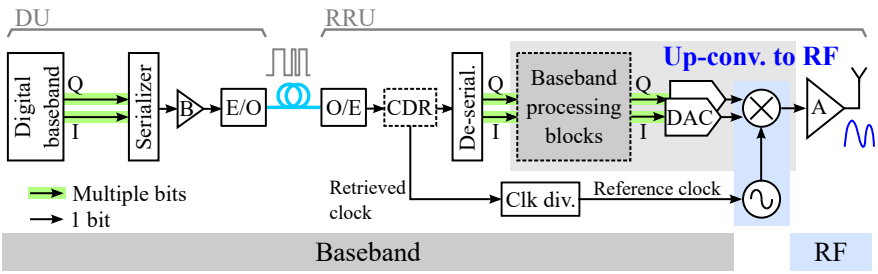

Figure 3.7: Digitized baseband signal over fiber (DRoF). The complexity of the baseband processing block depends on the selected function split option (Fig. 2.2).

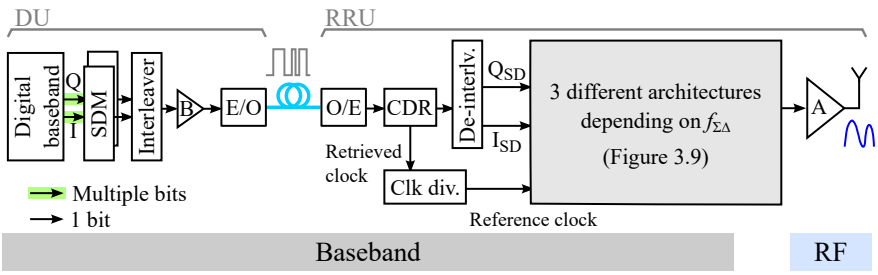

Figure 3.8: Sigma-delta modulated baseband signal over fiber (SD-BBoF). (I_{SD} and Q_{SD} denote the sigma-delta modulated I and Q signals, respectively; $f_{\Sigma\Delta}$ is the sample rate of the SDMs.)

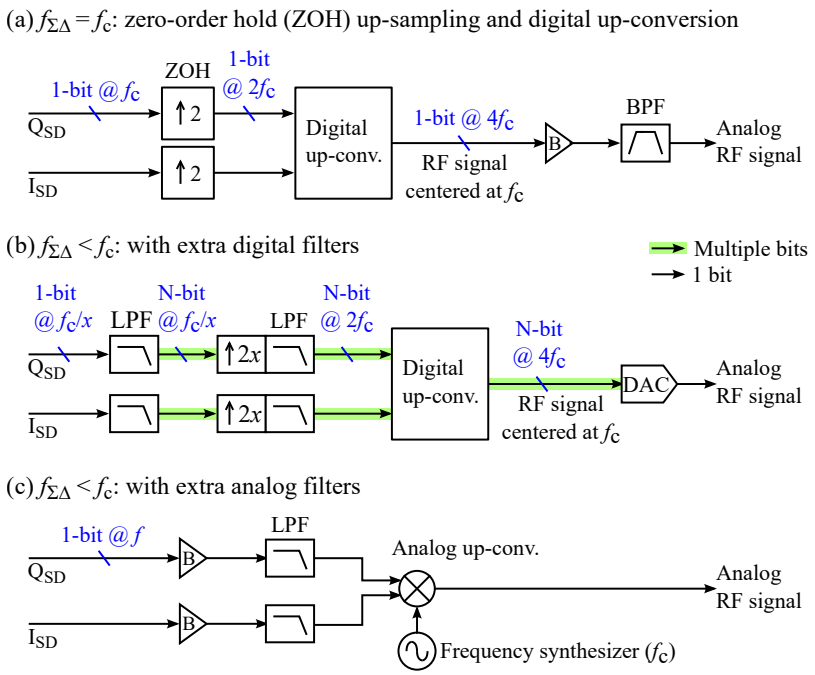

Figure 3.9: Different RRU architectures for SD-BBoF. (I_{SD} and Q_{SD} denote the sigma-delta modulated I and Q signals, respectively; $f_{\Sigma\Delta}$ is the sample rate of the SDMs; f_c is the carrier frequency.)

The RRU complexity of an SD-BBoF architecture depends on the selected sample rate of the SDMs ($f_{\Sigma\Delta}$). Three possible architectures are presented in Fig. 3.9.

The first architecture (Fig. 3.9a) chooses the same SDM sample rate ($f_{\Sigma\Delta}$) as the carrier frequency (f_c) in order to maintain the simple DL data path at RRUs. At RRUs, I_{SD} and Q_{SD} are $2\times$-up-sampled with the zero-order hold (ZOH) method and digitally up-converted for the wireless transmission. The simple RRU architecture comes with the cost of a mediocre optical bitrate efficiency.

Choosing a lower $f_{\Sigma\Delta}$ can lower the bitrate over fiber. However, it would not be possible to simply apply the ZOH up-sampling because the quantization noise will be too close to the band of interest. Extra filters must be added to remove the quantization noise.

In Fig. 3.9b, assume $f_{\Sigma\Delta}$ is lowered to f_c/x; x is an integer. After the first low-pass filter (LPF) pair removes the quantization noise, the I and Q signals are no longer bi-level. Performing digital up-conversion requires the I and Q signals to be sampled at $2f_c$. These signals are $2x\times$-up-sampled and pass the anti-aliasing (low-pass) filters. Since the output signals are no longer bi-level, DACs are required.

If analog filters are added (Fig. 3.9c), digital up-conversion is not possible and an analog up-converter must be included. In this option, $f_{\Sigma\Delta}$ can be chosen freely based on the signal quality requirement, thus simply denoted as f in the figure. Higher-order SDMs or advanced techniques can be applied to reach a high SQNR with an extremely low OSR [25]. Note that the clock divider in Fig. 3.8 provides the reference clock for the frequency synthesizer.

Adding either digital or analog filters largely increases the complexity. It is a design trade-off between the optical bitrate efficiency and the remote unit complexity.

SD-BBoF architectures provide more flexibility in the RRU complexity. Compared to DRoF, these more centralized architectures are also suitable for the coordination between RRUs. Furthermore, sigma-delta modulated signals have a high bit-error rate (BER) tolerance [26, 27]. A BER up to 2×10^{-4} can be tolerated in SDoF applications; the corresponding error vector magnitude (EVM) is about 0.56% (-45 dB) [27].

3.3 Radio-over-Fiber Uplink

Publications regarding RoF DLs are more common than uplinks (ULs). In this section, it is assumed that the received signals are filtered by anti-aliasing (band-pass) filters to remove out-of-band interferences. For RFoF ULs, the filtering happens before the electrical-to-optical conversion; for IFoF and BBoF

ULs, the filtering is done before the down-conversion.

Radio-Frequency Signal over Fiber (RFoF)

For RFoF ULs, the largest challenge is to maintain the signal quality. The RRU complexities are low in [28–30]; however, the signal qualities are mediocre. A phase-modulated link with interferometric detection (PM-ID) is proposed as an alternative by [31] with good (optical back-to-back) performance. However, the UL signals were generated by an arbitrary waveform generator (AWG) to have the most suitable signal ranges for the phase modulator (PM). Therefore, it may be fairer to compare the EVM values with other DL implementations.

When a sigma-delta based architecture is applied, the SDM sample rate must be sufficiently high with respect to the signal bandwidth to maintain the SQNR (Eq. (3.6)). Hence, sigma-delta-modulating RF signals directly is not practical even for sub-6 GHz bands.

A recently published work [32] proposes an SDoF-based system with all-digital pulse-width-modulation (PWM) based UL paths, whose RRU complexity is significantly low. The UL optical signals are generated by comparing the received RF signals with a tailored reference signal provided via the DL. However, the UL signal quality degradation with respect to the DL is not negligible: -30.0 dB for the DL and -25.5 dB for the UL. The degradation may limit the possibility to exploit channel reciprocity [33].

Intermediate-Frequency Signal over Fiber (IFoF)

Same as for DLs, RFoF links are not the most popular candidate for millimeter-wave (mmWave) applications. Down-converting the received RF signals to an intermediate frequency at RRUs is often preferred to relax the stringent device requirements [31, 34, 35]. Similar performance can be achieved for the DL and UL [36, 37]; the DL EVM is 1%–2% less than the UL case.

Baseband Signal over Fiber (BBoF)

Intuitively, BBoF architectures can be used in the UL data path by switching the hardware at the DU and RRUs.

The architecture illustrated in Fig. 3.9a is implemented for both the DL and UL of our proposed network [23, 24]. Placing down-converters at RRUs increases the complexity but achieves superior signal qualities compared to other RoF ULs. Note that the de-interleaved UL signals are only down-sampled at the central site; there is no need to up-convert them to the carrier frequency. It is possible to lower the SDM sample rate and interleave more I-Q pairs in one fiber; i.e. the bitrate efficiency can be significantly improved.

3.4 Comparison

Table 3.3 (for sub-6 GHz bands) and Table 3.4 (for high-frequency bands) summarize some RoF-related publications. The goal is to highlight the design trade-offs. Our publications that are included in this dissertation [11, 21, 24] are marked in bold.

For simplicity, some frequency bands are denoted with the commonly used terms. The exact frequency ranges corresponding to the frequency bands differ between regions / countries. The lowest channel starting frequency and the highest channel ending frequency are listed in Table 3.2.

	Frequency range	Corresponding 5G new radio (NR) band [38]
3.5 GHz	3.3–3.8 GHz	n78
28 GHz	24.25–29.5 GHz	n257 (26.5–29.5 GHz) n258 (24.25–27.5 GHz) n261 (27.5–28.35 GHz)
60 GHz	56–71 GHz[1]	

Table 3.2: Frequency bands.

For single-carrier (SC) signals, the bandwidth column lists the signal baudrate; unit: mega-baud (MBaud). For orthogonal frequency-division multiplexing (OFDM), LTE, and 5G signals, this column lists the signal bandwidth. The optical bitrate or bandwidth efficiency in the tables is calculated as follows:

1. If bi-level signals are transmitted over fiber, the efficiency is the transmitted signal bandwidth divided by the optical bitrate; unit: MHz/Gbps.

2. If analog signals are transmitted over fiber, the efficiency is the transmitted signal bandwidth (BW) divided by the full occupied optical bandwidth ($f_{\text{carrier}} + \text{BW}/2$); unit: MHz/GHz.

[1] The operating classes of IEEE 802.11ay [39] cover 56.16 GHz to 64.8 GHz. The unlicensed bands listed in 3GPP TR 38.807 [40] range from 57 GHz to 71 GHz. The frequency band 66–71 GHz is identified for use by administrations wishing to implement the terrestrial component of International Mobile Telecommunications (IMT).

Ref.	Freq. bands	Type		Optical			Max. signal bandwidth	Signal	EVM (%)	
				Tx-type	Fiber	Efficiency			DL	UL
[29] '16	2.4 GHz	A	RF	DFB	25 m SMF	61.39	152 MHz	OFDM	11.70	10.00[1]
[2] '17	1 GHz	A	RF	VCSEL	200 m MMF	76.92	80 MBaud	SC	4.47	-
		$\Sigma\Delta$				6.67	90 MBaud		3.98	-
[14] '18	3.5 GHz	$\Sigma\Delta$	RF	VCSEL	200 m MMF	15.89	218.75 MBaud	SC	2.80	-
[15] '19	960 MHz	$\Sigma\Delta$	RF	DFB, EAM	30 km SMF	36.00	180 MHz	LTE[2]	< 3.5	-
						39.60	198 MHz	5G	2.82	-
[41] '19	2.365 GHz	$\Sigma\Delta$	RF	VCSEL	30 m MMF	15.00	150 MBaud	SC	3.76	-
[31] '19	1.6 GHz	A	RF	PM[3]	20 km SMF	132.00	792 MHz	OFDM	-	~ 4
[11] '20	3.5 GHz	$\Sigma\Delta$	RF	VCSEL	100 m MMF	11.90	163.84 MHz	OFDM	3.50	-
[42] '20	< 10 GHz[4]	A	IF	LN-MZM[3]	20 km SMF	847.06	7.2 GHz	5G	3.14	-
[32] '21	2.365 GHz	$\Sigma\Delta$	RF	VCSEL	30 m MMF	2.00	20 MBaud	SC	3.16	5.31
[24] '21	3.5 GHz	$\Sigma\Delta$	BB	VCSEL	100 m MMF	4.44	40.96 MHz	OFDM	2.77	2.65

[1] The uplink (UL) performance degrades fast when the received signal power is not within a specific range.

[2] This is the performance when 10 LTE carriers are aggregated. With 14 carriers, the EVMs of 6 of them are less than 3.5% and 8 others are between 3.5% to 8%.

[3] PM: phase modulator; LN-MZM: lithium niobate Mach-Zehnder modulator.

[4] [42] aggregated 18 400 MHz 5G signals occupying the bandwidth from 0.1 GHz to 8.5 GHz including guard bands. All signals have EVMs between 3% to 4%.

Table 3.3: Radio-over-fiber technologies for sub-6 GHz bands.

Ref.	Freq. bands	Type	Optical			Wire-less	Max. signal bandwidth	Signal	EVM (%)	
			Tx-type	Fiber	Efficiency				DL	UL
[43] '18	12 GHz	ΣΔ RF	VCSEL	50 m MMF	7.81 31.25	-	250 MBaud 1 GBaud	SC	3.30 5.80	- -
[44] '18	20 GHz	A RF	DML	5 m SMF	181.82	-	4 GBaud	SC	7	-
[19] '19	28 GHz	A IF	DML	5 km SMF	333.33	N.A.	800 MHz	OFDM	~ 7	~ 5
[7] '20	28 GHz	ΣΔ RF	EAM	10 km SMF	3.91 7.81	-	390.63 MBaud 781.25 MBaud	SC	4.73 6.46	- -
[21] '20	28 GHz	ΣΔ IF	VCSEL	100 m MMF	30.44	-	299.20 MHz	OFDM	6.40	-
[45] '16	60 GHz	A RF	MZM	50 m SMF	0.33[1]	5 m	20 MHz	LTE	15.00	-
[46] '18	60 GHz	ΣΔ RF[2]	MZM	20 km SMF	- [2]	-	100 MBaud	SC	3.70	-
[47] '18	60 GHz	A IF	DFB	2.2 km SMF	171.49	6 m	281.25 MHz	OFDM	11.75	-
[36] '19	60 GHz	A IF	DFB, MZM EML	7 km SMF	909.09 909.09	5 m	6 GBaud 6 GBaud	SC	11.5 12	13 13
[48] '21	60 GHz	A IF	MZM	10 km SMF	41.32	1 m[3]	250 MBaud	SC	11.07	-
[37] '22	60 GHz	A IF	EML	25 km SMF	107.60	3 m	398 MHz	OFDM	12.5	-

[1] The efficiency is calculated based on the assumption that only the 20 MHz signal modulated around 60 GHz is transmitted over fiber.

[2] [46] converted the IF signal centered at 3.2 GHz to 56.8 GHz optically.

[3] The wireless signal is transmitted by a 32-element antenna array.

Table 3.4: Radio-over-fiber technologies for frequency bands > 6 GHz.

The "downlink (DL)" column provides the performance of signals which are generated, transmitted over fiber, and measured after being converted back to the electrical domain. Some publications use the term: fiber-wireless link. The "uplink (UL)" is the link in which received (electrical back-to-back or wireless) signals are transmitted over fiber and measured after being converted back to the electrical domain. It is also referred to as the wireless-fiber link.

It is important to mention that many parameters can have impacts on the performance, presented with EVM values in the tables. The tables summarize the most relevant information on the various works. Despite the difficulties to make fair comparisons, some remarks can be drawn from them.

Linearity of the optical transmitter / modulator

Owing to the bi-level characteristic, sigma-delta ($\Sigma\Delta$) based optical links are immune to nonlinear distortion. With re-sampling at the (optical) receiver side, the impacts of attenuation and noise are simply bit errors. The optical BER is usually low; e.g. for NRZ signals, a BER lower than 10^{-12} is usually guaranteed within the maximum fiber distance provided by the suppliers. $\Sigma\Delta$-based links often use direct intensity modulation with directly modulated lasers (DMLs) such as vertical-cavity surface-emitting lasers (VCSELs) and distributed feedback (DFB) lasers. The main advantages are the simple and compact architectures [49]. $\Sigma\Delta$-based links can provide good-quality signals even with VCSELs, which show limited linearity. Hence, it is possible to use commercial SFPs or QSFPs[2] [11, 14, 21, 24, 32, 41].

Externally modulated lasers (EMLs) are more common for ARoF because of the more stringent requirements on the optical signal quality. The two tables include publications using phase modulators (PMs), such as Mach-Zehnder modulators (MZMs), or intensity modulators (IMs), such as electro-absorption modulators (EAMs).

Optical bitrate or bandwidth efficiency

It can be easily observed from the tables that ARoF-based technologies achieve noticeably better optical bandwidth efficiency. For mmWave applications, there are much more IFoF-based architectures than RFoF-based ones.

$\Sigma\Delta$-based architectures have very different bitrate efficiency, depending on various design criteria, e.g. the carrier frequency or the RRU complexity. The

[2] A small form-factor pluggable (SFP) is a hot-pluggable network interface module often used for telecommunication and data communication applications. It contains an optical transmitter and an optical receiver. A quad small form-factor pluggable (QSFP) is the 4-lane expansion of an SFP.

efficiency is sometimes worse than CPRI, whose bitrate efficiency is around 20 MHz/Gbps [15]. However, as discussed in this chapter, for ΣΔ-based architectures, there is always the design trade-off between bitrate efficiency and the RRU complexity.

Achievable signal quality

Care should be taken when comparing the EVM values, given the different signal formats and bandwidths. Both ARoF- and ΣΔ-based DLs can achieve low EVMs. However, the scarcity of UL-related publications proves the challenge of RFoF ULs. It is worth mentioning that our BI-SDoF link provides good quality signals for both the DL and UL.

3.5 Conclusion

In this chapter, we introduced the concept of sigma-delta modulation and compared three sigma-delta based RoF technologies with others. Table 3.5 summarizes all RoF technologies introduced in the chapter. It can be clearly concluded from the table that no solution is perfect; i.e. none of them gets "green lights" in all columns.

		Remote radio unit complexity	Optical bitrate / bandwidth efficiency	Analog and optical device linearity requirements
ΣΔ	RFoF	low	low	low
A	RFoF	low	high	high
ΣΔ	IFoF	mid-low	mid	low
A	IFoF	mid	high	mid-high
ΣΔ	BBoF	mid-low[1]	mid	low
D	BBoF	high	mid-low[2]	low

[1] The complexity and the efficiency both depend on the sample rate of the sigma-delta modulators; It is a design trade-off between the two.
[2] The bitrate efficiency of CPRI is very low; eCPRI is better.

Table 3.5: Radio-over-fiber technology comparison.

Depending on the applications, different design trade-offs will result in different choices. The simple RRUs and relaxed linearity requirements on devices definitely make sigma-delta based architectures appealing for distributed / cell-free (massive) MIMO systems.

References

[1] C. Ranaweera *et al.*, "5G C-RAN with Optical Fronthaul: an Analysis from a Deployment Perspective," *Journal of Lightwave Technology*, vol. 36, no. 11, pp. 2059–2068, 2018.

[2] L. Breyne *et al.*, "Comparison Between Analog Radio-over-Fiber and Sigma Delta Modulated Radio-over-Fiber," *IEEE Photonics Technology Letters*, vol. 29, no. 21, pp. 1808–1811, 2017.

[3] P. M. Aziz *et al.*, "An Overview of Sigma-Delta Converters," *IEEE Signal Processing Magazine*, vol. 13, no. 1, pp. 61–84, 1996.

[4] M. M. Ebrahimi *et al.*, "Delta-Sigma-Based Transmitters: Advantages and Disadvantages," *IEEE Microwave Magazine*, vol. 14, no. 1, pp. 68–78, 2013.

[5] H. Li *et al.*, "A 21-GS/s Single-Bit Second-Order Delta-Sigma Modulator for FPGAs," *IEEE Transactions on Circuits and Systems II: Express Briefs*, vol. 66, no. 3, pp. 482–486, 2019.

[6] R. Hossain *et al.*, "Parallel MASH $\Sigma\Delta$ Modulator," 2012, US Patent US8203475B2. Available on URL: https://patents.google.com/patent/US8203475

[7] H. Li *et al.*, "Real-Time 100-GS/s Sigma-Delta Modulator for All-Digital Radio-over-Fiber Transmission," *Journal of Lightwave Technology*, vol. 38, no. 2, pp. 386–393, 2020.

[8] *Analog Device*, "Sigma-Delta ADCs and DACs Application Note (AN283)," last accessed on Jul. 6, 2022. Available on URL: https://www.analog.com/media/en/technical-documentation/application-notes/29252429152571724505492368045817 1an283.pdf

[9] S. Jayaprakasam *et al.*, "Distributed and Collaborative Beamforming in Wireless Sensor Networks: Classifications, Trends, and Research Directions," *IEEE Communications Surveys & Tutorials*, vol. 19, no. 4, pp. 2092–2116, 2017.

[10] C.-Y. Wu *et al.*, "Distributed MU-MIMO Demonstration Using FPGA-Based Sigma-Delta-over-Fiber," in *Proc. 45th European Conference on Optical Communication (ECOC 2019)*, 2019, pp. 1–4.

[11] ——, "Distributed Multi-User MIMO Transmission Using Real-Time Sigma-Delta-over-Fiber for Next Generation Fronthaul Interface," *Journal of Lightwave Technology*, vol. 38, no. 4, pp. 705–713, 2020.

[12] M. Gagnaire, "Chapter 4: Analog and Digitized Radio-over-Fiber," in *Fiber-Wireless Convergence in Next-Generation Communication Networks Systems, Architectures, and Management*, M. Tornatore *et al.*, Eds. Switzerland: Springer International Publishing, 2017, pp. 99–126.

[13] A. Frappé *et al.*, "An All-Digital RF Signal Generator Using High-Speed $\Sigma\Delta$ Modulators," *IEEE Journal of Solid-State Circuits*, vol. 44, no. 10, pp. 2722–2732, 2009.

[14] C.-Y. Wu *et al.*, "Real-Time 4×3.5 Gbps Sigma Delta Radio-over-Fiber for a Low-Cost 5G C-RAN Downlink," in *Proc. 44th European Conference on Optical Communication (ECOC 2018)*, 2018, pp. 1–3.

[15] J. Wang *et al.*, "Delta-Sigma Modulation for Next Generation Fronthaul Interface," *Journal of Lightwave Technology*, vol. 37, no. 12, pp. 2838–2850, 2019.

[16] "Common Public Radio Interface (CPRI) Specification V7.0," 2015, last accessed on Jul. 6, 2022. Available on URL: http://www.cpri.info/spec.html

[17] U. Gliese *et al.*, "Chromatic Dispersion in Fiber-Optic Microwave and Millimeter-Wave Links," *IEEE Transactions on Microwave Theory and Techniques*, vol. 44, no. 10, pp. 1716–1724, 1996.

[18] P. T. Dat *et al.*, "Radio-on-Radio-over-Fiber: Efficient Fronthauling for Small Cells and Moving Cells," *IEEE Wireless Communications*, vol. 22, no. 5, pp. 67–75, 2015.

[19] M. Sung *et al.*, "5G Trial Services Demonstration: IFoF-Based Distributed Antenna System in 28 GHz Millimeter-Wave Supporting Gigabit Mobile Services," *Journal of Lightwave Technology*, vol. 37, no. 14, pp. 3592–3601, 2019.

[20] ——, "RoF-Based Radio Access Network for 5G Mobile Communication Systems in 28 GHz Millimeter-Wave," *Journal of Lightwave Technology*, vol. 38, no. 2, pp. 409–420, 2020.

[21] C.-Y. Wu *et al.*, "Distributed Antenna System Using Sigma-Delta Intermediate-Frequency-over-Fiber for Frequency Bands above 24 GHz," *Journal of Lightwave Technology*, vol. 38, no. 10, pp. 2765–2773, 2020.

[22] "Common Public Radio Interface: eCPRI Interface Specification V2.0," 2019, last accessed on Jul. 6, 2022. Available on URL: http://www.cpri.info/spec.html

[23] C.-Y. Wu *et al.*, "Demonstration of a Scalable Distributed Antenna System Using Real-Time Bit-Interleaved Sigma-Delta-over-Fiber Architectures," in *Proc. 46th European Conference on Optical Communication (ECOC 2020)*, 2020, pp. 1–4.

[24] ——, "A Bit-Interleaved Sigma-Delta-over-Fiber Fronthaul Network for Frequency-Synchronous Distributed Antenna Systems," *Applied Sciences*, no. 23, 2021.

[25] L. Zhong *et al.*, "Experimental Demonstration of Delta-sigma Modulation Supported 65536-QAM OFDM Transmission for Fronthaul/WiFi Applications," in *Proc. 47th European Conference on Optical Communication (ECOC 2021)*, 2021, pp. 1–3.

[26] J. Wang *et al.*, "Delta-Sigma Digitization and Optical Coherent Transmission of DOCSIS 3.1 Signals in Hybrid Fiber Coax Networks," *Journal of Lightwave Technology*, vol. 36, no. 2, pp. 568–579, 2018.

[27] I. C. Sezgin *et al.*, "Effect of VCSEL Characteristics on Ultra-High Speed Sigma-Delta-over-Fiber Communication Links," *Journal of Lightwave Technology*, vol. 37, no. 9, pp. 2109–2119, 2019.

[28] A. Aighobahi *et al.*, "Experimental Analysis of Single and Multiple Antenna Units in Uplink of Radio-over-Fiber Distributed Antenna System," in *Proc. 2015 International Topical Meeting on Microwave Photonics (MWP)*, 2015, pp. 1–4.

[29] ——, "Capacity and Error Performance Verification of Multi-Antenna Schemes in Radio-over-Fiber Distributed Antenna System," *Journal of Lightwave Technology*, vol. 34, no. 20, pp. 4779–4785, 2016.

[30] B. Schrenk *et al.*, "Fully Passive Remote Radio Head for Uplink Cell Densification in Wireless Access Networks," *IEEE Photonics Technology Letters*, vol. 27, no. 9, pp. 970–973, 2015.

[31] E. Moutaly *et al.*, "Phase Modulated Radio-over-Fiber for Efficient 5G Fronthaul Uplink," *Journal of Lightwave Technology*, vol. 37, no. 23, pp. 5821–5832, 2019.

[32] I. C. Sezgin *et al.*, "All-Digital, Radio-over-Fiber, Communication Link Architecture for Time-Division Duplex Distributed Antenna Systems," *Journal of Lightwave Technology*, vol. 39, no. 9, pp. 2769–2779, 2021.

[33] E. G. Larsson *et al.*, "Massive MIMO for Next Generation Wireless Systems," *IEEE Communications Magazine*, vol. 52, no. 2, pp. 186–195, 2014.

[34] A. Kaszubowska-Anandarajah and L.P. Barry, "Remote Downconversion Scheme for Uplink Configuration in Radio/Fiber Systems," in *Proc. 2005 7th International Conference Transparent Optical Networks*, vol. 2, 2005, pp. 161–164.

[35] C. Vagionas *et al.*, "Linearity Measurements on a 5G mmWave Fiber Wireless IFoF Fronthaul Link with Analog RF Beamforming and 120° Degrees Steering," *IEEE Communications Letters*, vol. 24, no. 12, pp. 2839–2843, 2020.

[36] N. Argyris *et al.*, "A 5G mmWave Fiber-Wireless IFoF Analog Mobile Fronthaul Link with up to 24-Gb/s Multiband Wireless Capacity," *Journal of Lightwave Technology*, vol. 37, no. 12, pp. 2883–2891, 2019.

[37] K. Kanta *et al.*, "Demonstration of a Hybrid Analog-Digital Transport System Architecture for 5G and Beyond Networks," *Applied Sciences*, vol. 12, no. 4, 2022.

[38] "3GPP TS 38.104. New Radio (NR): Base Station (BS) Radio Transmission and Reception (Release 17) (V17.6.0)," June 2022.

[39] "IEEE Standard for Information Technology–Telecommunications and Information Exchange between Systems Local and Metropolitan Area Networks–Specific Requirements Part 11: Wireless LAN Medium Access Control (MAC) and Physical Layer (PHY) Specifications Amendment 2: Enhanced Throughput for Operation in License-Exempt Bands above 45 GHz," 2021, last accessed on Jul. 6, 2022. Available on URL: https://ieeexplore.ieee.org/document/9502046

[40] "3GPP TR 38.807. Technical Specification Group Radio Access Network; Study on requirements for NR beyond 52.6 GHz (Release 16) (V16.1.0)," March 2021.

[41] I. C. Sezgin *et al.*, "A Low-Complexity Distributed-MIMO Testbed Based on High-Speed Sigma-Delta-over-Fiber," *IEEE Transactions on Microwave Theory and Techniques*, vol. 67, no. 7, pp. 2861–2872, 2019.

[42] K. Nishimura *et al.*, "Analog Radio-over-Fiber Based Mobile Fronthaul Toward Beyond-5G Era," in *Proc. 2020 International Topical Meeting on Microwave Photonics (MWP)*, 2020, pp. 21–24.

[43] I. C. Sezgin *et al.*, "A Flexible Multi-Gbps Transmitter Using Ultra-High Speed Sigma-Delta-over-Fiber," in *Proc. 2018 IEEE/MTT-S International Microwave Symposium (IMS)*, 2018, pp. 1195–1198.

[44] K. Van Gasse *et al.*, "Analog Radio-over-Fiber Transceivers Based on III-V-on-Silicon Photonics," *IEEE Photonics Technology Letters*, vol. 30, no. 21, pp. 1818–1821, 2018.

[45] L. Cheng *et al.*, "Coordinated Multipoint Transmissions in Millimeter-Wave Radio-over-Fiber Systems," *Journal of Lightwave Technology*, vol. 34, no. 2, pp. 653–660, 2016.

[46] A. Lorences-Riesgo *et al.*, "Real-Time FPGA-Based Delta-Sigma-Modulation Transmission for 60 GHz Radio-over-Fiber Fronthaul," in *Proc. 44th European Conference on Optical Communication (ECOC 2018)*, 2018, pp. 1–3.

[47] U. Habib *et al.*, "Analog Radio-over-Fiber Supported Increased RAU Spacing for 60 GHz Distributed MIMO Employing Spatial Diversity and Multiplexing," *Journal of Lightwave Technology*, vol. 36, no. 19, pp. 4354–4360, 2018.

[48] E. Ruggeri *et al.*, "A 5G Fiber Wireless 4 Gb/s WDM Fronthaul for Flexible 360° Coverage in V-Band Massive MIMO Small Cells," *Journal of Lightwave Technology*, vol. 39, no. 4, pp. 1081–1088, 2021.

[49] E. Sackinger, *Broadband Circuits for Optical Fiber Communication*. Hoboken, NJ, USA: John Wiley & Sons, 2005.

Part II

Distributed Antenna Systems Enabled by Sigma-Delta-over-Fiber Technologies

4

Sigma-Delta RFoF Based Distributed Antenna System for Sub-6 GHz Bands

This chapter introduces a distributed antenna system (DAS) for sub-6 GHz bands. The system has one central site that connects to two low-complexity remote radio units (RRUs) via fibers. Each RRU has one transmit antenna. From the central site to the RRUs, sigma-delta modulated radio-frequency signals are transmitted—sigma-delta modulated radio-frequency signal over fiber (SD-RFoF). With the two transmit antennas and the served users, we demonstrate the downlink performance of a 2×2 multi-user multiple-input multiple-output (MU-MIMO) system. This chapter is based on the following publication:

Chia-Yi Wu, Haolin Li, Olivier Caytan, *et al.*, "Distributed Multi-User MIMO Transmission Using Real-Time Sigma-Delta-over-Fiber for Next Generation Fronthaul Interface," *Journal of Lightwave Technology*, 2020.

4.1 Introduction

Multiple-input multiple-output (MIMO) is the most common way to increase wireless spectral efficiency by exploiting spatial diversity [1, 2]. Compared with co-located MIMO, distributed MIMO can further improve the channel capacity [3].

A form of distributed MIMO—the coordinated multi-point (CoMP) transmission—has already been proposed and deployed for 4G [4]. Multiple base stations, which are not co-located, serve cell-edge users cooperatively, so the transmitted signals do not interfere with each other and may combine constructively to increase the received signal power. Such coordination requires extra information being exchanged between multiple base stations. Originally, the extra information must go via the backhaul networks. Both the latency and the backhaul traffic congestion were potential problems. Combining the centralized radio access network (C-RAN) architecture with the CoMP concept allows the extra data to be exchanged via only the fronthaul network [5].

In addition to interference mitigation, the distributed scheme is especially suitable for high-capacity hot-spot scenarios. With the spatial multiplexing technique, the transmitted data rate can be easily multiplied.

For this prototype system, we prioritized the simplicity of RRUs. Hence, the SD-RFoF architecture (Fig. 4.1) is applied. The simple, inexpensive and power-efficient RRU architecture is appealing for applications with high RRU density [6, 7]. Furthermore, it will be shown in the measurement results that SD-RFoF has also high scalability for different signal bandwidths without modifying the underlying hardware.

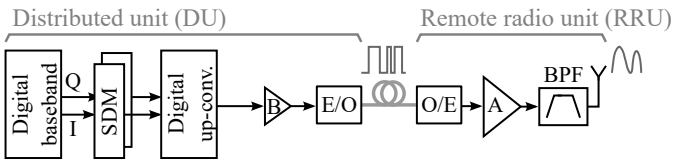

Figure 4.1: Sigma-delta modulated radio-frequency signal over fiber (SD-RFoF). (SDM: sigma-delta modulator; B: binary driver; E/O / O/E: electrical-to-optical / optical-to-electrical converter; A: amplifier; BPF: band-pass filter.)

Because the transmitted signals are up-converted at the distributed unit (DU)[1], the carrier synchronization between transmitters—one of the large challenges for distributed MIMO transmission [8]—is no longer a problem. The

[1]To align with the 5G NG-RAN terminology, the term "distributed unit (DU)" is used for the central site where all physical-layer blocks are located.

distributed MIMO SD-RFoF system suffers no performance degradation caused by the frequency asynchronism between transmitters, and thus needs no sophisticated synchronization algorithm.

Section 4.2 introduces a real-time FPGA-based 2×2 distributed MU-MIMO system implemented using off-the-shelf and in-house developed components. Then, it describes the measurement workflow and the applied algorithms. In Section 4.3, the SD-RFoF link performance of different OFDM signal bandwidths is provided, followed by the MIMO measurement results and the performance evaluation of the carrier frequency asynchronism between RRUs.

4.2 System Architecture and Experimental Methodology

4.2.1 SD-RFoF-Based Distributed Antenna System

Fig. 4.2 shows a 2×2 MU-MIMO downlink transmission using SD-RFoF links. The system consists of one DU, two RRUs, and two independent receivers / users.

The physical (PHY) layer signal processing, e.g. the OFDM signal generation and MIMO precoding, is done by MATLAB scripts on a personal computer (PC). The generated OFDM baseband signals[2], whose in-phase (I) and quadrature (Q) signal are both 16-bit, are loaded to the DU FPGA via Ethernet. The real-time modules of the DU, including the real-time low-pass SDMs [9] and digital up-conversion [10], are implemented on a *Xilinx Virtex Ultrascale* FPGA (VCU108). Each RRU has only a photodiode, a band-pass filter (BPF), two amplifiers, and an antenna.

Distributed Unit (DU)

The loaded OFDM signals are streamed from the on-FPGA DDR to 4 (2×2, one I-Q pair per RRU) SDMs using a *Xilinx* AXI direct memory access (DMA) IP. The SDMs modulate the signals at 7 Gbps (gigabits per second). Digital up-conversion [10] translates the modulated I and Q signal (both 1-bit) to one 14 Gbps binary signal with a center frequency of around 3.5 GHz for each RRU. Fig. 4.2a shows the spectrum and waveform of a MATLAB-generated OFDM signal. Fig. 4.2b shows the simulated spectrum and waveform after sigma-delta modulation and digital up-conversion with fixed-point representation; it can be seen that the quantization noise is pushed out of the band of interest.

[2]The related parameters are included in Appendix A.

Each non-return-to-zero (NRZ) signal is converted to the optical domain using a QSFP-100G-SR4 module and transmitted over an OM4 multi-mode fiber (MMF). The QSFP-100G-SR4 module has four 850 nm VCSELs (vertical-cavity surface-emitting lasers); we use only two of them for two MMFs. Each MMF connects the DU to one RRU. The QSFP module supports link lengths up to 100 m for OM4 MMFs. The maximum optical launch power per lane is approximately 2.4 dBm. Note that the optical link lengths can be largely extended if single-mode QSFP modules and fibers are exploited [11].

Remote Radio Unit (RRU)

At each RRU, the received optical signal is converted back to the electrical domain using a GaAs PIN photodiode with a responsivity around 0.4 A/W. The photodiode is impedance-matched to the low-noise amplifier (LNA), *Mini-Circuits* PMA3-83LN+, to maximize the power transfer at 3.5 GHz [12]. The LNA amplifies the electrical signal coming from the photodiode; it has a low noise figure of 1.3 dB and 20.8 dB gain when operating at a 5V supply. The measured spectrum at the output of an LNA is shown in Fig. 4.2c; a spectrum similar to Fig. 4.2b is observed.

Then, the out-of-band quantization noise is filtered by a BPF as shown in the measured spectrum (Fig. 4.2d). The filtered analog signals are amplified by power amplifiers (PAs), followed by in-house developed antennas[3] to transmit the radio-frequency (RF) signals.

Mini-Circuits amplifiers ZX60-83LN-S+ are used as the PAs. The power measured at the PA output is -2.51 dBm/40.96 MHz (-2.70 dBm/163.84 MHz). Note that the position of the PA and BPF are exchangeable if using a switching-mode power amplifier [14, 15].

Receiver / User

The two receivers, each with an architecture identical to a SISO receiver, operate independently. They have the same antennas as the RRUs. For each receiver, the antenna is first connected to an LNA. The amplified received signal is down-converted using a zero intermediate frequency (zero-IF) receiver and sampled by an analog front-end evaluation kit (*Analog Device FMCOMMS1-EBZ*) at 327.68 MHz ($2\times$ the largest signal bandwidth, 163.84 MHz). A *Xilinx Kintex 7* FPGA (KC705) collects the data for offline signal processing using MATLAB.

[3]The air-filled substrate-integrated-waveguide (AFSIW) cavity-backed slot antennas [13] are matched to a 50 Ω impedance between 2.95 GHz to 3.90 GHz.

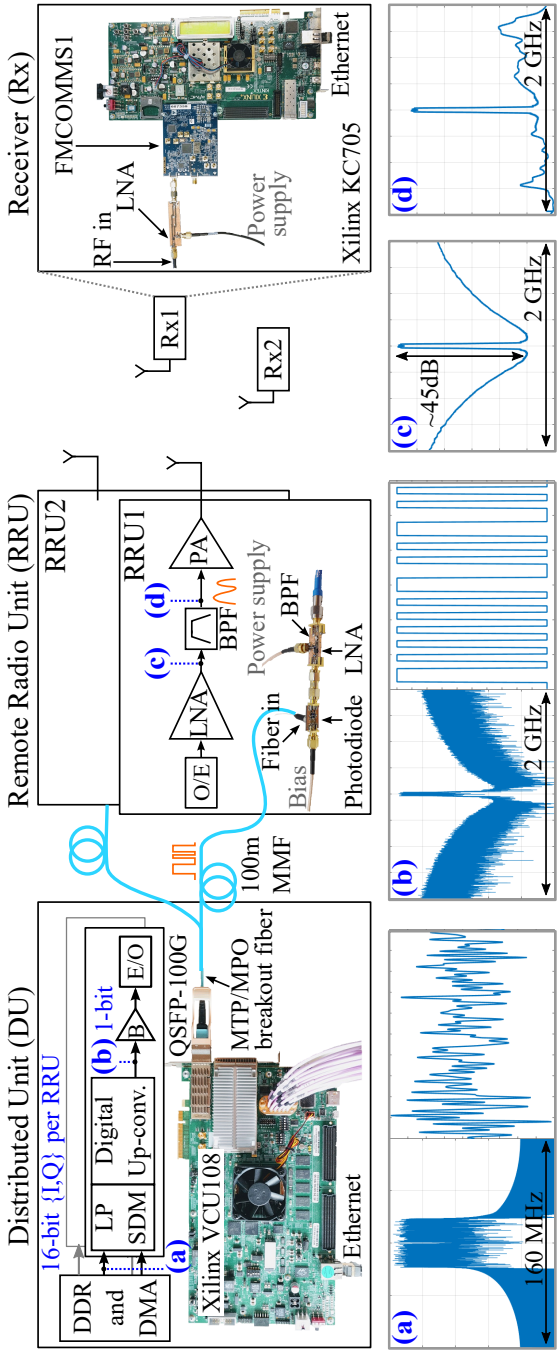

Figure 4.2: System architecture. (DDR: DDR4 SDRAM device; DMA: direct memory access; LP SDM: low-pass sigma-delta modulator; B: binary driver; E/O / O/E: electrical-to-optical/optical-to-electrical converter; MMF: multi-mode fiber; LNA: low-noise amplifier; BPF: band-pass filter; PA: power amplifier.)
(a) Spectrum and waveform of a 40.96 MHz OFDM baseband signal generated by MATLAB;
(b) simulated spectrum and waveform of the digital up-conversion output;
(c) measured spectrum of the non-return-to-zero (NRZ) output signal of the LNA;
(d) measured spectrum of the BPF output.

The signal processing includes OFDM frame boundary detection, carrier frequency offset (CFO) correction using the algorithm proposed in [16], fast Fourier transform (FFT), least-square channel estimation [17], and QAM demodulation.

4.2.2 MU-MIMO OFDM Signal

In a 2×2 MIMO system, the received OFDM baseband data on a subcarrier can be written as

$$\begin{bmatrix} \mathrm{R}_1 \\ \mathrm{R}_2 \end{bmatrix} = \underbrace{\begin{bmatrix} \mathrm{H}_{11} & \mathrm{H}_{21} \\ \mathrm{H}_{12} & \mathrm{H}_{22} \end{bmatrix}}_{\text{Channel matrix: } \mathbf{H}} \begin{bmatrix} \mathrm{X}_1 \\ \mathrm{X}_2 \end{bmatrix} + \begin{bmatrix} \mathrm{W}_1 \\ \mathrm{W}_2 \end{bmatrix} \tag{4.1}$$

where all elements in Eq. (4.1) are complex numbers; R_j is the signal received by receiver j; H_{ij} denotes the equivalent channel frequency response (CFR) in baseband between RRU i and receiver j; X_i is the baseband data transmitted by RRU i; W_j is the additive noise. The subcarrier index is omitted to keep the expression simple.

The workflow has two phases as illustrated in Fig. 4.3: the training and data transmission phases. The workflow is fully realized in MATLAB.

Training Phase

During the training phase, frequency-interleaved training sequences[4] for channel estimation are transmitted. The receivers receive the signals and estimate the CFRs with the least square channel estimation algorithm proposed in [17]. Ideal channel information feedback is assumed.

For the case with two transmitters, the training sequences should last at least two OFDM frames. In a noisy environment, using longer training sequences, i.e. averaging over multiple estimated H_{ij}, results in better channel estimation results.

Data Transmission Phase

During the data transmission phase, for each subcarrier, the precoded data is transmitted. The precoded data is generated based on the zero-forcing (ZF) technique with the estimated CFRs.

[4] See Appendix A.

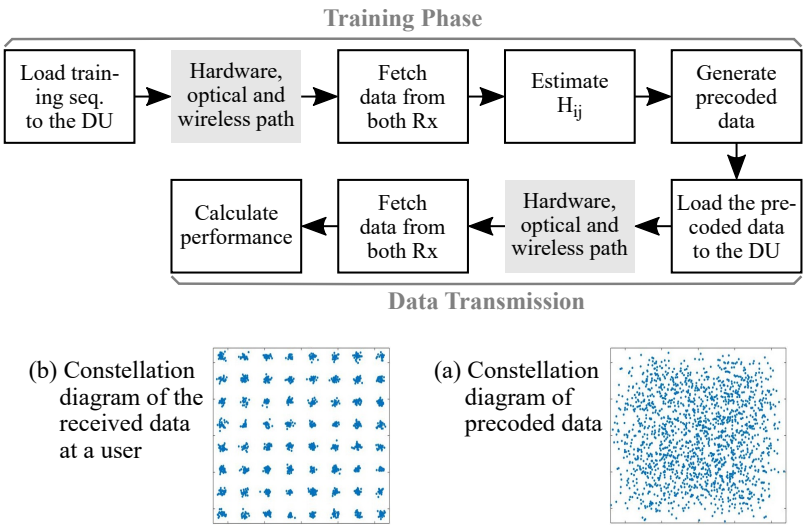

Figure 4.3: Measurement workflow.

$$\begin{bmatrix} X_1 \\ X_2 \end{bmatrix} = \underbrace{\begin{bmatrix} \alpha & -\beta\frac{\hat{H}_{21}\hat{H}^*_{11}}{\hat{H}^*_{11}\hat{H}_{11}} \\ -\alpha\frac{\hat{H}_{12}\hat{H}^*_{22}}{\hat{H}^*_{22}\hat{H}_{22}} & \beta \end{bmatrix}}_{\text{Precoding matrix: } \mathbf{G}} \begin{bmatrix} S_1 \\ S_2 \end{bmatrix} \tag{4.2}$$

where $\hat{H}_{ij}$ denotes the estimated CFR between RRU i and receiver j during the latest training phase and S_j is the baseband data—the constellation points—expected to be received by receiver j; α and β are two real constants that have the same values for all subcarriers in an OFDM frame.

The precoding matrix **G** in Eq. (4.2) is applied, instead of the inverse of the channel matrix **H** in Eq. (4.1), because it is easier to adjust the dynamic range of the precoded data to fit the input range of SDMs by tuning the two constants α and β.

Combining Eq. (4.1) and Eq. (4.2),

$$\begin{bmatrix} R_1 \\ R_2 \end{bmatrix} = \begin{bmatrix} c_1 & i_1 \\ i_2 & c2 \end{bmatrix} \begin{bmatrix} S_1 \\ S_2 \end{bmatrix} + \begin{bmatrix} W_1 \\ W_2 \end{bmatrix} \tag{4.3}$$

where

$$c_1 = \alpha(H_{11} - H_{21}\frac{\hat{H}_{12}\hat{H}^*_{22}}{\hat{H}^*_{22}\hat{H}_{22}}), \tag{4.4}$$

$$c_2 = \beta(\mathrm{H}_{22} - \mathrm{H}_{12}\frac{\hat{\mathrm{H}}_{21}\hat{\mathrm{H}}_{11}^*}{\hat{\mathrm{H}}_{11}^*\hat{\mathrm{H}}_{11}})\,, \tag{4.5}$$

$$i_1 = \beta(\mathrm{H}_{21} - \mathrm{H}_{11}\frac{\hat{\mathrm{H}}_{21}\hat{\mathrm{H}}_{11}^*}{\hat{\mathrm{H}}_{11}^*\hat{\mathrm{H}}_{11}})\,, \tag{4.6}$$

and

$$i_2 = \alpha(\mathrm{H}_{12} - \mathrm{H}_{22}\frac{\hat{\mathrm{H}}_{12}\hat{\mathrm{H}}_{22}^*}{\hat{\mathrm{H}}_{22}^*\hat{\mathrm{H}}_{22}})\,. \tag{4.7}$$

Assuming the channel estimation is sufficiently accurate, i.e. $\hat{\mathrm{H}}_{ij} \approx \mathrm{H}_{ij}$, both i_1 and i_2 will be close to zero. In this case, a receiver i shall receive its data S_i with almost no interference ($\mathrm{S}_{j,j\neq i}$) as shown in Fig. 4.3b. From the measurement results, it will become clear that the performance difference between the MU-MIMO setup and a single-input single-output (SISO) link is relatively small in terms of error vector magnitude (EVM).

4.3 Measurement Results

In this section, the transmitter performance is provided. OFDM signals with different bandwidths were transmitted over an SD-RFoF link. The distributed MIMO performance was measured in a typical office environment; the SISO performance is provided as a baseline. In the end, to highlight the advantage of using RFoF links for distributed MIMO deployment, we also evaluated the performance degradation by deliberately introducing frequency asynchronism between RRUs. When up-conversion is performed at the RRU, small frequency deviations can be expected [18, 19]. The performance is presented in error vector magnitude (EVM) normalized to the average constellation power.

4.3.1 Link Performance

To show the quality of the SDoF link, the performance was measured without the wireless path. The output of the power amplifier was directly connected to an *Analog Device* FMCOMMS1-EBZ; appropriate attenuation was applied in between to prevent the receiver chain from saturation. The same reference clock was used for the up-conversion and down-conversion, i.e. there was no CFO. Fig. 4.4a plots the EVM values against the signal bandwidths and Fig. 4.4b and c show the received constellation diagrams.

There is no significant performance difference in terms of EVM between the 64-QAM and 256-QAM cases. The performance degrades as the signal bandwidth increases because of two reasons: First, when the total transmitted signal power is kept the same, the power spectral density (PSD) of the signal

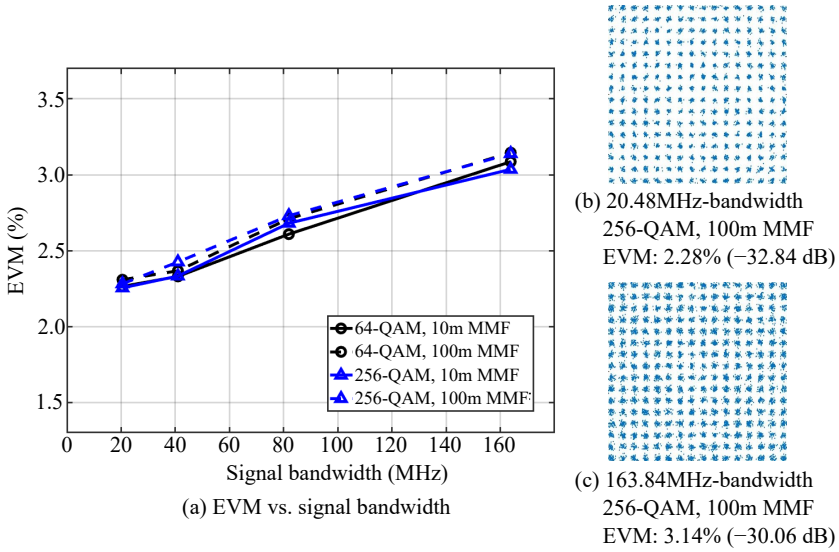

(a) EVM vs. signal bandwidth

(b) 20.48MHz-bandwidth
256-QAM, 100m MMF
EVM: 2.28% (−32.84 dB)

(c) 163.84MHz-bandwidth
256-QAM, 100m MMF
EVM: 3.14% (−30.06 dB)

Figure 4.4: Measured EVM values and constellation diagrams.

decreases as the signal bandwidth increases. Because the noise PSD stays the same, the SNR drops accordingly. Second, the oversampling ratio (OSR), defined as:

$$\mathrm{OSR} = \frac{f_{\Sigma\Delta}/2}{\mathrm{BW}}, \tag{4.8}$$

decreases as the signal bandwidth (BW) increases thus resulting in a lower signal-to-quantization-noise ratio (SQNR); $f_{\Sigma\Delta}$ is the sample rate of the SDM.

The 3.14% EVM of the 163.84 MHz-bandwidth OFDM signals transmitted over a 100 m MMF is lower than the 3GPP EVM requirement for 256-QAM: 3.5% (−29.12 dB) [20].

The identical hardware architecture was used for all measured bandwidths, implying the high scalability of the SD-RFoF link. The optical bitrate efficiency was not considered a severe issue in this work because each DU-RRU link used one fiber in this demonstration. For network architectures that require higher bitrate efficiency, performing up-conversion at RRUs can largely decrease the line rate. However, the RRU complexity will increase.

It is possible to reach longer link lengths by exploiting QSFP modules for single-mode fibers. As presented in [11], the SD-RFoF link performance is sufficient for up to 20 km of single-mode fibers.

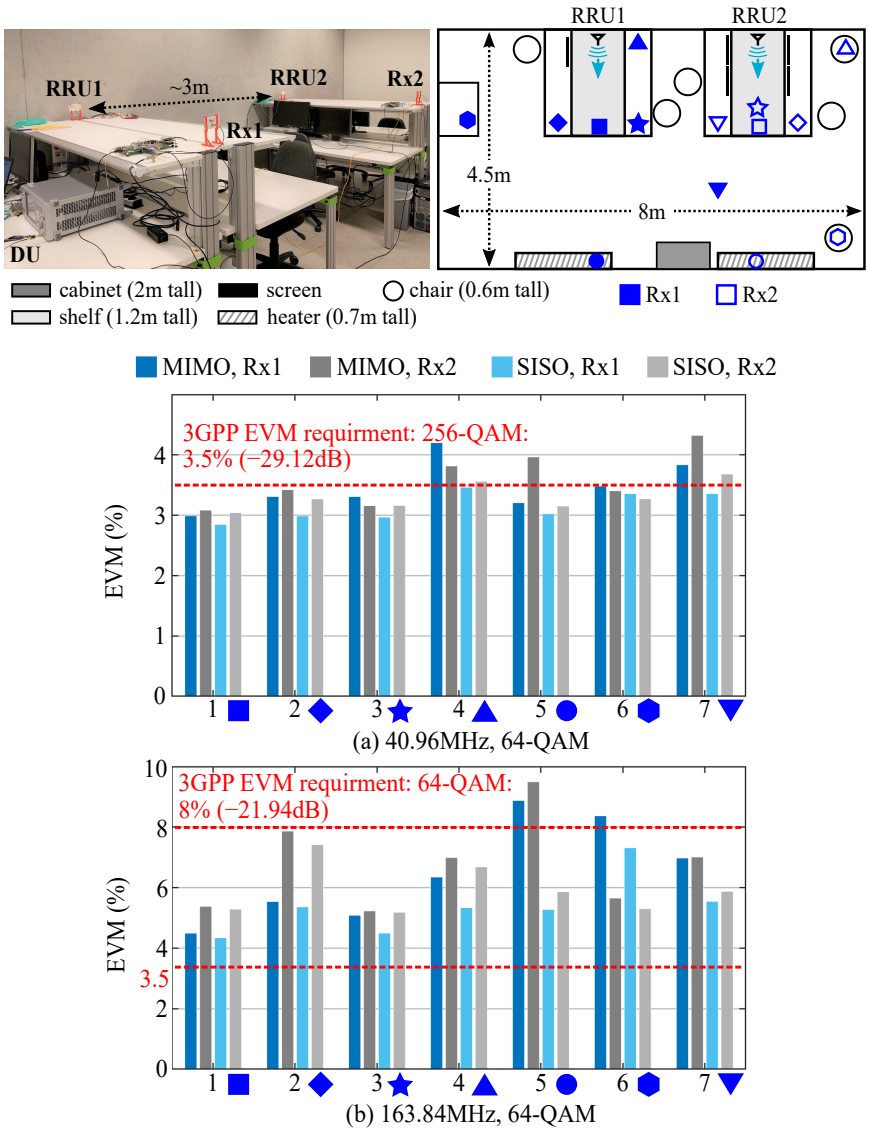

Figure 4.5: The measurement setup, the simplified layout of the room and the distributed MIMO performance of two bandwidths: (a) 40.96 MHz; (b) 163.84 MHz.

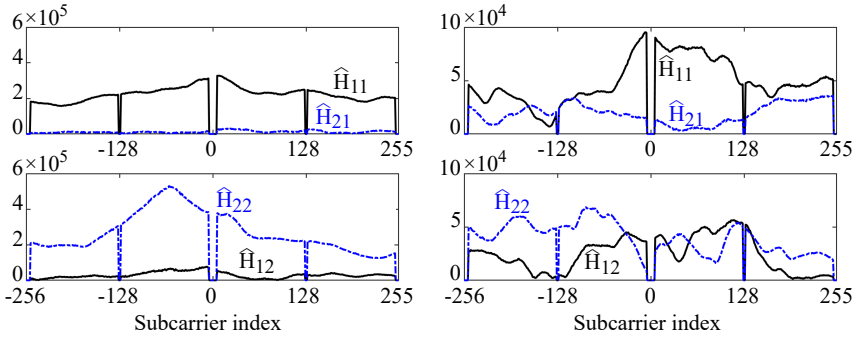

(a) Estimated CFRs of Case 1 ■ (b) Estimated CFRs of Case 5 ●

Figure 4.6: Magnitude of the estimated channel frequency responses (CFRs): $\hat{\mathrm{H}}_{ij}$. (a) Case 1, 163.84 MHz; (b) Case 5, 163.84 MHz.

4.3.2 Distributed MIMO Performance

The combined optical-wireless performance was measured in an office that was 8 m long, 4.5 m wide, and 3.5 m tall approximately. Each RRU was connected to the DU with a 100 m MMF.

Fig. 4.5 includes the photo and simplified layout of the room and the measured EVM values. The furniture in the room, especially the metallic surfaces of the heaters and shelves, formed a multipath-rich environment.

The directions of the RRU antennas are illustrated in Fig. 4.5. The receiver antennas always faced the nearest RRU antenna. Without loss of generality, the receiver (Rx) that was geometrically closer to RRU 1 was named Rx 1, denoted with the filled icons. The hollowed icons represent Rx 2. The transmit power per transmitter was kept the same for the SISO and MIMO cases. No common reference clock was provided to the DU and receivers. Since the up-conversion was performed at the DU, there was no carrier frequency asynchronism between the two RRUs. The CFO between the RRUs and receivers was estimated and compensated offline using MATLAB.

We measured 64-QAM OFDM signals with two different signal bandwidths: 40.96 MHz (Fig. 4.5a) and 163.84 MHz (Fig. 4.5b). For the 40.96 MHz MIMO cases, the average EVM of all cases and two receivers is 3.53% (-29.04 dB). For most cases, the performance satisified 3GPP EVM requirement for 256-QAM (3.5%) [20], so it was possible to transmit 256-QAM signals. However, to make a fair comparison with the 163.84 MHz cases, 64-QAM was chosen. The average EVM increase compared to the SISO transmission (3.22%, -29.83 dB) is 0.8 dB. The average EVM for the 163.84 MHz MIMO cases is 6.66% (-23.52 dB) and 5.66% (-24.94 dB) for SISO; the average EVM in-

crease is 1.42 dB.

Fig. 4.6a shows the magnitudes of $\hat{\mathrm{H}}_{ij}$ of the case with the best performance: Case 1 in Fig. 4.5. The magnitudes were calculated using the signed 16-bit I and Q values collected by *Analog Device* FMCOMMS1-EBZ without any normalization. During the MIMO transmission, the desired data signal for Rx 1 came from RRU 1 and the interference came from RRU 2. As shown in Fig. 4.6a, the magnitudes of the signal CFRs, $\hat{\mathrm{H}}_{11}$ and $\hat{\mathrm{H}}_{22}$, were both sufficiently larger than the magnitudes of the interference CFRs, $\hat{\mathrm{H}}_{12}$ and $\hat{\mathrm{H}}_{21}$. Therefore, there was little performance degradation between the MIMO and SISO transmission.

Case 5 had a similar setup geometry but with longer distances. However, almost 4 dB degradation in EVM was measured between the MIMO and SISO transmission. It can be seen from Fig. 4.5 that the EVM values of the SISO cases were both worse than those of Case 1. The estimated CFRs of the signals, $\hat{\mathrm{H}}_{11}$ and $\hat{\mathrm{H}}_{22}$, had much smaller magnitudes than those of Case 1. The estimated CFRs were expected to be less accurate based on these two observations. Besides, the interferences were strong compared to the signals as shown in Fig. 4.6b. Because the interferences were strong, the imperfect interference cancellation due to inaccurate estimation influenced the performance more. Stronger power amplifiers should be able to improve the received signal quality and, therefore, improve the estimation accuracy.

Singular Values of the Channel Matrices

To evaluate the richness of multipaths of the experimental environment, the correlation between CFRs were analyzed. We applied singular value decomposition (SVD) to the channel matrices. As described in Eq. (4.1), for each subcarrier, $\mathbf{H}$ is a 2×2 matrix:

$$\mathbf{H} = \begin{bmatrix} \mathrm{H}_{11} & \mathrm{H}_{21} \\ \mathrm{H}_{12} & \mathrm{H}_{22} \end{bmatrix} \tag{4.9}$$

where H_{ij} denotes the equivalent CFR between RRU i and receiver j. The SVD of $\mathbf{H}$ is

$$\mathbf{H} = \mathbf{U}\,\mathbf{S}\,\mathbf{V}^{\mathrm{H}} \tag{4.10}$$

where the columns of $\mathbf{U}$ and $\mathbf{V}$ are formed by the left and right singular vectors of $\mathbf{H}$ respectively, $\mathbf{V}^{\mathrm{H}}$ denotes the Hermitian transpose (conjugate transpose) of $\mathbf{V}$, and $\mathbf{S}$ is a diagonal matrix with non-negative real numbers on the diagonal. $\mathbf{S}$ contains the singular values, σ_1 and σ_2, of $\mathbf{H}$:

$$\mathbf{S} = \begin{bmatrix} \sigma_1 & 0 \\ 0 & \sigma_2 \end{bmatrix}. \tag{4.11}$$

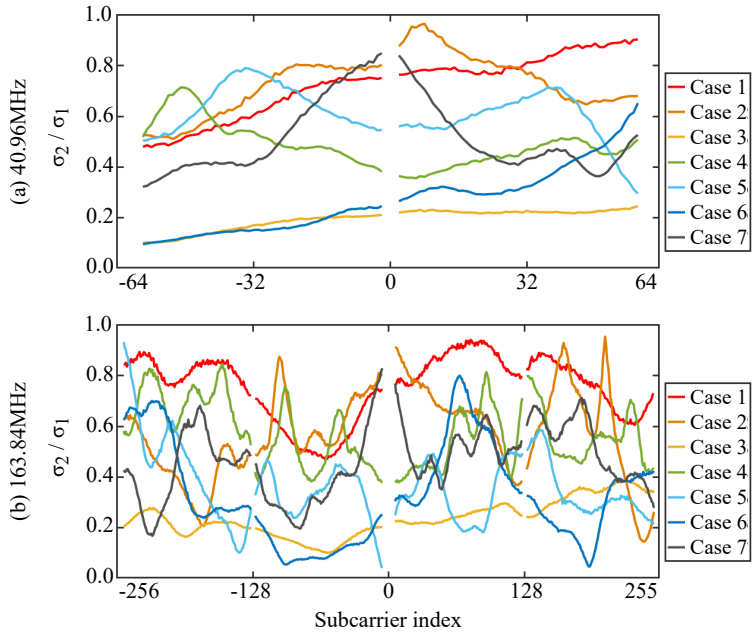

Figure 4.7: Ratios of singular values (σ_2/σ_1) of the channel matrices ($\hat{\mathbf{H}}$).

Bandwidth	Case						
(MHz)	1	2	3	4	5	6	7
40.96	0.72	0.73	0.19	0.49	0.61	0.27	0.52
163.84	0.76	0.57	0.24	0.57	0.36	0.33	0.46

Table 4.1: Average σ_2/σ_1 over non-zero subcarriers.

For MIMO channels that are highly correlated, the ratio of the two singular values, σ_2/σ_1, is close to zero, implying that both row vectors of $\mathbf{H}$, $[\mathrm{H}_{11}\ \mathrm{H}_{21}]$ and $[\mathrm{H}_{12}\ \mathrm{H}_{22}]$, are so similar that they can both be expressed as scalar products of one vector—the first column of $\mathbf{V}$. On the contrary, for MIMO channels that are totally independent, i.e. $\mathbf{H}$ is an identity matrix, σ_2/σ_1 is one.

Fig 4.7 plots the ratios σ_2/σ_1 (calculated from the estimated CFRs) of all non-zero subcarriers for 40.96 MHz-bandwidth (Fig 4.7a) and 163.84 MHz (Fig 4.7b). Table 4.1 lists the average σ_2/σ_1 over non-zero subcarriers for each case (Fig. 4.5).

The ratios σ_2/σ_1 indicate the richness of multipaths. However, a smaller σ_2/σ_1 does not always result in a larger MIMO-SISO performance difference,

e.g. Case 3. Case 3 has the smallest average σ_2/σ_1 for both the 40.96 MHz and 163.84 MHz case, but the MIMO-SISO performance difference is 0.47 dB for 40.96 MHz and 0.57 dB for 163.84 MHz.

The accuracy of the estimated CFRs and the power difference between the signal and interference paths are more dominant factors. In other words, the MIMO transmission had the best performance when the signals from both RRUs were strong enough to estimate H_{ij} accurately and when each receiver was close to one RRU.

In general, the MIMO performance was comparable to the SISO transmission, implying that the wireless spectral efficiency significantly increased by exploiting spatial diversity.

4.3.3 Impact of Frequency Asynchronism

This subsection highlights one of the benefits of the proposed architecture by measuring the EVM values versus the carrier frequency deviation between RRUs.

The proposed architecture up-converts the sigma-delta modulated signals to 3.5 GHz at one DU and transmits the RF signals to the RRUs over fiber. Up-converting both signals at one DU makes it possible to use the same local oscillator and thus guarantee the carrier synchronism between RRUs. Digitized radio-over-fiber (DRoF) based C-RAN, in contrast to the proposed architecture, generates the carrier signals at each RRU separately. As frequency

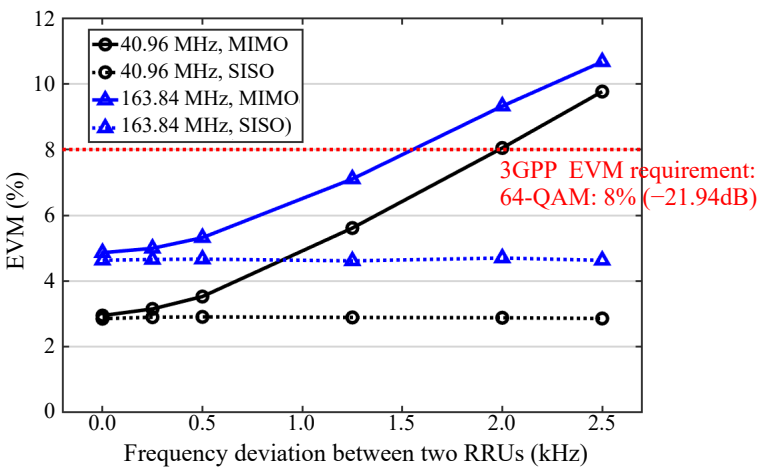

Figure 4.8: Measured EVM vs. carrier frequency deviation between two remote radio units (RRUs).

deviations may be introduced while generating each carrier signal [19], its performance can degrade consequently due to carrier frequency asynchronism between RRUs. Algorithms have been developed to estimate and compensate for the multiple carrier frequency offsets for CoMP transmission [21]. Both the estimation and compensation are challenging and require complex computation. The impact of frequency asynchronism for 4G C-RAN has also been evaluated in [18] with simulation results.

For different base station classes, a carrier frequency error ranging from ± 0.05 to ± 0.25 ppm, corresponding to ± 175 Hz to ± 875 Hz for 3.5 GHz, is allowed [20]. Since the carrier frequencies of the two RRUs of our proposed setup were always synchronous, extra CFOs were added to RRU 2 to evaluate the impact of frequency asynchronism.

The CFO effect can be modeled as a phase shift growing linearly with the time index [22]. Neglecting the effect of the multipath channel and noise, the received and sampled time-domain baseband signal can be written as

$$r[n] = x[n]e^{j2\pi\frac{\Delta f}{f_s}n} \tag{4.12}$$

where $x[n]$ and $r[n]$ are the transmitted and received baseband signals in the time domain, the integer n is the time index, Δf is the CFO in Hz and f_s is the OFDM sampling frequency. Extra CFOs were added by rotating each sample of the time-domain sequence $x[n]$ with the phase $2\pi(\Delta f/f_s)n$ while generating the 64-QAM OFDM signals using MATLAB.

The receivers were placed as the Case 1 in Fig. 4.5 that had strong line-of-sight (LoS) paths between both RRUs and receivers. The averaged EVM values (over Rx 1 and Rx 2) are shown in Fig. 4.8. When there was no frequency difference between the two RRUs, the MIMO performance was almost as good as SISO; the EVM difference is about 0.3 dB. However, even with a difference as small as 250 Hz, performance degradation is noticeable; the EVM difference between the MIMO and SISO transmission increases to 0.7 dB. The performance gap between the MIMO and SISO cases grows rapidly when the carrier frequency difference increases.

With the ambition to increase the number of RRUs, compensating for multiple CFOs between RRUs will become unfeasible. Hence, an architecture that can guarantee the frequency synchronization between RRUs—as we proposed—is highly beneficial.

4.4 Conclusion

This chapter demonstrated a fully implemented 2×2 distributed MU-MIMO OFDM downlink system using real-time SD-RFoF links. The OFDM base-

band signals were sigma-delta modulated and digitally up-converted to a carrier frequency around 3.5 GHz on an FPGA; the signals were transmitted over multi-mode fibers using a commercial QSFP module.

The link performance satisfied the 3GPP EVM requirement for 256-QAM (3.5%): the EVM average of 163.84 MHz-bandwidth OFDM signals over 100 m multi-mode fibers was 3.14% (-30.06 dB). It is worth mentioning that the same hardware implementation was used for different bandwidths. Combining SD-RFoF links and MIMO transmission guarantees the frequency synchronism between RRUs; as shown by the 2×2 MU-MIMO performance, the wireless spectral efficiency almost doubled. An average EVM of 3.5% was measured for 40.96 MHz-bandwidth signals (64-QAM, 330 Mbps) and 6.66% for 163.84 MHz-bandwidth (64-QAM, 1.4 Gbps).

This setup has two appealing attributes: low-complexity RRUs and synchronism between RRUs. For sub-6 GHz networks which do not require high bitrate efficiency, this architecture can be a cost-efficient candidate.

References

[1] J. Proakis and M. Salehi, *Digital Communications*, Chapter 15: Multiple-Antenna Systems, Fifth ed. McGraw-Hill Education, 2007.

[2] A. Lozano and N. Jindal, "Transmit Diversity vs. Spatial Multiplexing in Modern MIMO Systems," *IEEE Transactions on Wireless Communications*, vol. 9, no. 1, pp. 186–197, 2010.

[3] J. Wang and L. Dai, "Asymptotic Rate Analysis of Downlink Multi-User Systems with Co-Located and Distributed Antennas," *IEEE Transactions on Wireless Communications*, vol. 14, no. 6, pp. 3046–3058, 2015.

[4] R. Irmer *et al.*, "Coordinated Multipoint: Concepts, Performance, and Field Trial Results," *IEEE Communications Magazine*, vol. 49, no. 2, pp. 102–111, 2011.

[5] T. Pfeiffer, "Next Generation Mobile Fronthaul and Midhaul Architectures [Invited]," *Journal of Optical Communications and Networking*, vol. 7, no. 11, pp. B38–B45, 2015.

[6] G. Torfs *et al.*, "ATTO: Wireless Networking at Fiber Speed," *Journal of Lightwave Technology*, vol. 36, no. 8, pp. 1468–1477, 2018.

[7] M. F. Keskin *et al.*, "Localization with Distributed MIMO Using a High-Speed Sigma-Delta-over-Fiber Testbed," *IEEE Microwave and Wireless Components Letters*, pp. 1–4, 2022.

[8] S. Jayaprakasam *et al.*, "Distributed and Collaborative Beamforming in Wireless Sensor Networks: Classifications, Trends, and Research Directions," *IEEE Communications Surveys & Tutorials*, vol. 19, no. 4, pp. 2092–2116, 2017.

[9] H. Li *et al.*, "A 21-GS/s Single-Bit Second-Order Delta-Sigma Modulator for FPGAs," *IEEE Transactions on Circuits and Systems II: Express Briefs*, vol. 66, no. 3, pp. 482–486, 2019.

[10] A. Frappé *et al.*, "An All-Digital RF Signal Generator Using High-Speed $\Sigma\Delta$ Modulators," *IEEE Journal of Solid-State Circuits*, vol. 44, no. 10, pp. 2722–2732, 2009.

[11] C.-Y. Wu *et al.*, "Real-Time 4×3.5 Gbps Sigma Delta Radio-over-Fiber for a Low-Cost 5G C-RAN Downlink," in *Proc. 44th European Conference on Optical Communication (ECOC 2018)*, 2018, pp. 1–3.

[12] J. Van Kerrebrouck *et al.*, "Real-Time All-Digital Radio-over-Fiber LTE Transmission," in *Proc. 2017 Advances in Wireless and Optical Communications (RTUWO)*, 2017, pp. 83–86.

[13] O. Caytan *et al.*, "Passive Opto-Antenna as Downlink Remote Antenna Unit for Radio Frequency over Fiber," *Journal of Lightwave Technology*, vol. 36, no. 19, pp. 4445–4459, 2018.

[14] J. Wang *et al.*, "Delta-Sigma Modulation for Next Generation Fronthaul Interface," *Journal of Lightwave Technology*, vol. 37, no. 12, pp. 2838–2850, 2019.

[15] I. C. Sezgin *et al.*, "A Low-Complexity Distributed-MIMO Testbed Based on High-Speed Sigma-Delta-over-Fiber," *IEEE Transactions on Microwave Theory and Techniques*, vol. 67, no. 7, pp. 2861–2872, 2019.

[16] A. N. Mody and G. L. Stuber, "Synchronization for MIMO OFDM Systems," in *Proc. 2001 IEEE Global Communications Conference (GLOBECOM '01)*, vol. 1, 2001, pp. 509–513.

[17] J.-J. van de Beek *et al.*, "On Channel Estimation in OFDM Systems," in *Proc. 1995 IEEE 45th Vehicular Technology Conference. Countdown to the Wireless Twenty-First Century*, vol. 2, 1995, pp. 815–819.

[18] J. Li *et al.*, "Performance Evaluation of Cloud-RAN System with Carrier Frequency Offset," in *Proc. 2012 IEEE Global Communications Conference (GLOBECOM) Workshops*, 2012, pp. 222–226.

[19] A. Pizzinat *et al.*, "Things You Should Know About Fronthaul," *Journal of Lightwave Technology*, vol. 33, no. 5, pp. 1077–1083, 2015.

[20] "3GPP TS 38.104. New Radio (NR): Base Station (BS) Radio Transmission and Reception (Release 17) (V17.6.0)," June 2022.

[21] Y.-S. Yang *et al.*, "A Low-Complexity Transceiver Structure with Multiple CFOs Compensation for OFDM-Based Coordinated Multi-Point Systems," *IEEE Transactions on Communications*, vol. 63, no. 7, pp. 2658–2670, 2015.

[22] J. J. van de Beek *et al.*, "ML Estimation of Time and Frequency Offset in OFDM Systems," *IEEE Transactions on Signal Processing*, vol. 45, no. 7, pp. 1800–1805, 1997.

5

Sigma-Delta IFoF Based Distributed Antenna System for the 28 GHz Bands

This chapter introduces a distributed antenna system (DAS) for the frequency bands above 24 GHz, the so-called 26 GHz bands (in Europe) or 28 GHz bands (worldwide). The DAS is enabled by the sigma-delta modulated intermediate-frequency signal over fiber (SD-IFoF) architecture. The signals to be transmitted are up-converted to an intermediate frequency around 2.5 GHz and transmitted to the two remote radio units (RRUs) via fibers. Compared to the architecture proposed in Chapter 4, although the RRU complexity increases, this architecture has an improved optical bitrate efficiency. With two transmit antennas, each belonging to one RRU, and one served user, we demonstrate the digital beamforming performance of a 2×1 distributed antenna / multiple-input single-output (MISO) system. This chapter is based on the following publication:

Chia-Yi Wu, Haolin Li, Joris Van Kerrebrouck, *et al.*, "Distributed Antenna System Using Sigma-Delta Intermediate-Frequency-over-Fiber for Frequency Bands Above 24GHz," *Journal of Lightwave Technology*, 2020.

5.1 Introduction

The demand for wide signal bandwidths and the scarcity of available bands below 6 GHz stimulated millimeter-wave (mmWave) (30–300 GHz) research [1]. The 28 GHz bands have been allocated for 5G [2, 3]. The wider and cheaper bands come with large challenges.

Compared to sub-6 GHz bands, mmWave bands suffer from larger attenuation over the air [4, 5]. Multiple-antenna systems can form beams to combat path loss [6]. The higher path loss also makes it even more necessary to have line-of-sight (LoS) paths by avoiding obstructions [7, 8]. Combining DASs and mmWave bands seems promising to increase LoS paths and therefore increase coverage [9].

For mmWave applications, intermediate-frequency signal over fiber (IFoF) architectures are more favorable as described in Chapter 3. The optical device requirements are less stringent compared to radio-frequency signal over fiber (RFoF) links. Many publications demonstrated the performance of analog IFoF (A-IFoF) links [9–13]. IFoF technologies also avoid the low optical spectral / bitrate efficiency due to the high radio-frequency (RF) carriers [14–16]. However, A-IFoF-based DASs often require additional low-frequency reference clocks to generate the RF carriers [9, 10].

In this proposed DAS, the SD-IFoF links (Fig. 5.1) provide signals to RRUs. At each RRU, a clock-and-data recovery module (CDR) reconstructs a clock signal from the non-return-to-zero (NRZ) downlink bitstream. The retrieved clock can be used as a reference by the frequency synthesizer to generate the RF carrier frequency. The proposed architecture achieves a higher bitrate efficiency than the setup introduced in Chapter 4 and offers more flexibility to switch between different carrier frequencies. However, the two frequency synthesizers at the two RRUs bring uncorrelated phase noise into the system.

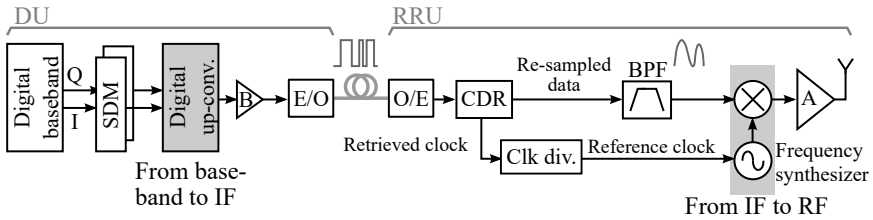

Figure 5.1: Sigma-delta modulated intermediate-frequency signal over fiber (SD-IFoF). (SDM: sigma-delta modulator; B: binary driver; E/O / O/E: electrical-to-optical / optical-to-electrical converter; CDR: clock-and-data recovery module; BPF: band-pass filter; A: amplifier; Clk div.: clock divider.)

Section 5.2 introduces the DAS with two RRUs for the 28 GHz bands. In Section 5.3, we provide the performance of the SD-IFoF link. Then, the 2-by-1 beamforming performance is evaluated with different distances between the two RRUs. In the end, the performance degradation due to asynchronous phase noise between RRUs is evaluated with experimental results.

5.2 System Architecture and Experimental Methodology

5.2.1 SD-IFoF-Based Distributed Antenna System

Fig. 5.2 shows our distributed antenna downlink system. The system consists of one distributed unit (DU), two RRUs, and one receiver / user. Table 5.1 lists all commercial components used in this experimental setup.

Distributed Unit (DU)

The physical (PHY) layer signal processing, e.g. the OFDM signal generation and precoding, is done by MATLAB scripts on a personal computer (PC). The real-time sigma-delta modulators (SDMs) [17] and digital up-conversion [18] are implemented on a *Xilinx Virtex Ultrascale* FPGA (VCU108).

The generated OFDM baseband signals[1] are loaded to the DU FPGA via Ethernet. The loaded signals are streamed to 2×2 (one I-Q pair per RRU) SDMs using a *Xilinx* AXI direct memory access (DMA) IP and modulated at 4.9152 Gbps (gigabits per second). Digital up-conversion [18] translates the modulated I and Q signals (both 1-bit) to one 9.8304 Gbps NRZ signal with a 2.4576 GHz center frequency for each RRU. The bitrate is chosen based on the supported data-rate range of the CDRs *Analog Devices* ADN2917 (8.5–11.3 Gbps) and the passband frequency range of the available band-pass filters in our lab (2.3–2.6 GHz).

The NRZ signals are converted to the optical domain using a QSFP-100G-SR4 module and transmitted over OM4 multi-mode fibers (MMFs). The QSFP-100G-SR4 module has four 850 nm VCSELs (vertical-cavity surface-emitting lasers); we use only two of them to transmit signals over two MMFs. Each MMF connects the DU to one RRU. The QSFP module supports link lengths up to 100 m for OM4 MMFs. The maximum optical launch power per lane is approximately 2.4 dBm. Note that the optical link lengths can be largely extended if single-mode QSFP modules and fibers are exploited [19].

[1] The related parameters are included in Appendix A.

Distributed unit (DU):	
electrical-to-optical converter	QSFP-100G-SR4 (850 nm)
Remote radio unit (RRU):	
optical-to-electrical converter	QSFP-40G-SR4 (850 nm)
clock and data recovery module (CDR)	*Analog Devices* ADN2917 (The CDR supports data rates between 8.5 Gbps and 11.3 Gbps.)
clock divider	*Analog Devices* HMC983LP5E
frequency synthesizer	*Analog Devices* EVAL-ADF5356
up-converter (including an up-mixer and a quadrupler)	*Analog Devices* EVAL-ADMV1013 (The clock input path operates from 5.4 GHz to 10.25 GHz.)
low-noise amplifier (LNA)	*Analog Devices* HMC1040LP3CE (The LNA operates between 24 GHz and 43.5 GHz and delivers 23 dB of small signal gain.)
power amplifier (PA)	*Analog Devices* HMC943LP5E (The PA operates between 24 GHz and 31.5 GHz and delivers 21 dB of gain.)
Receiver (Rx) / user:	
low-noise amplifier (LNA)	*Analog Devices* HMC1040LP3CE
band-pass filter (BPF)	*Marki Microwave* FB-2770 (Passband: 23.55 GHz to 31.85 GHz.)
down-converter (including a down-mixer and a quadrupler)	*Analog Devices* EVAL-ADMV1014 (The clock input path operates from 5.4 GHz to 10.25 GHz.)
analog front-end evaluation kit	*Analog Devices* FMCOMMS1-EBZ

Table 5.1: Hardware components.

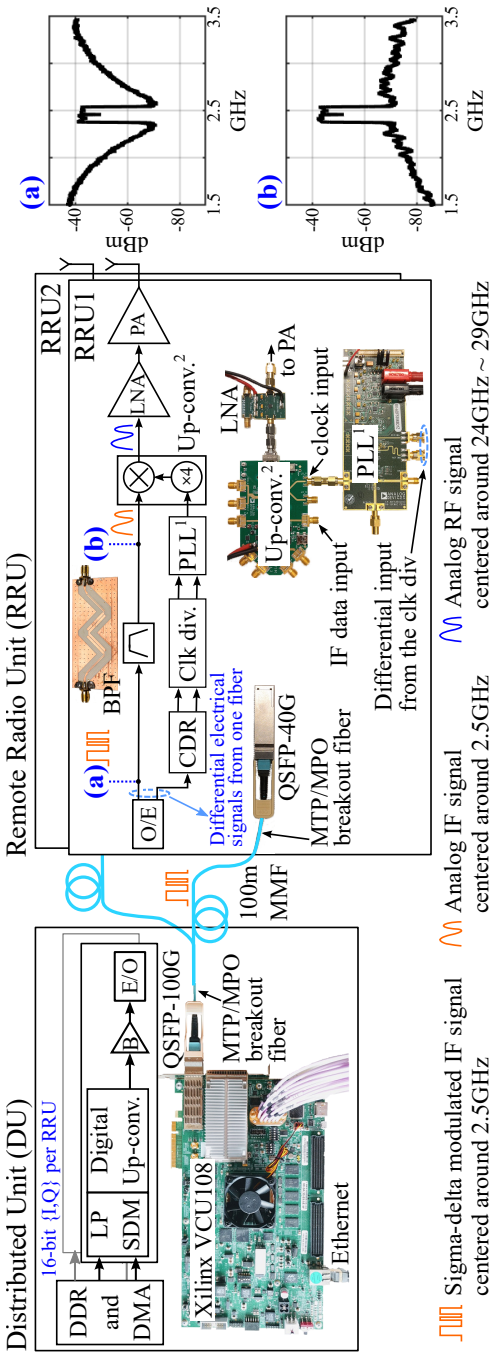

Figure 5.2: System architecture. (DDR: DDR4 SDRAM device; DMA: direct memory access; LP SDM: low-pass sigma-delta modulator; B: binary driver; E/O / O/E: electrical-to-optical / optical-to-electrical converter; MMF: multi-mode fiber; BPF: band-pass filter; LNA: low-noise amplifier; PA: power amplifier; CDR: clock and data recovery module; Clk div.: clock divider; PLL: phase lock loop.)
(a) Measured spectrum of the QSFP-40G output signal; (b) measured spectrum of the band-pass filter output.
[1]PLL-based frequency synthesizer to generate the reference input for the up-converter.
[2]Up-converter to convert the IF signal to RF. It has an up-mixer and a quadrupler which generates a clock signal with a frequency that is four times the frequency of the reference clock input.

Remote Radio Unit (RRU)

The received optical signal is converted back to the electrical domain using a QSFP-40G-SR4 module. The module can convert four optical signals, received from four separate fibers, to four pairs of differential electrical signals. For this setup, each RRU requires only one photo receiver out of the four.

In the setup, we use one lane of the differential output for the data path and the other lane for the reference clock generation. Theoretically, CDRs can provide both reconstructed data and a reconstructed clock signal, as shown in Fig. 5.1. However, the CDRs in our setup introduce too much jitter. The signal-to-noise ratio (SNR) of the CDR-reconstructed data signal is worse than its original input.

Fig. 5.2a is the spectrum measured by an *Anritsu* signal analyzer (MS2692A) after the QSFP-40G-SR4 converts the received optical NRZ signal to an electrical signal. It can be seen that the quantization noise is pushed out of the band of interest. The out-of-band quantization noise is filtered by a band-pass filter (BPF), as shown in the measured spectrum (Fig. 5.2b). The filtered IF signal is connected to the IF data input port of the up-converter *Analog Devices* EVAL-ADMV1013.

At each RRU, the CDR retrieves a clock signal from the sigma-delta modulated downlink bitstream. The frequency of the reconstructed clock is half the bit rate over fiber: 4.9152 GHz. The proposed architecture uses a clock divider to generate a low-frequency clock (24.576 MHz) as the reference clock signal for the phase lock loop (PLL) in the frequency synthesizer. The output of the frequency synthesizer can be configured to have frequencies which are simple fractions of the frequency of the input reference clock. The frequency synthesizer then generates the input clock signal (f_{PLL}) for the up-converter.

The quadrupler in the up-converter generates a clock signal with a frequency that is four times the input clock frequency. The up-mixer modulates the IF input signal with the output clock signal of the quadrupler. The RF carrier frequencies are calculated using Eq. (5.1) and listed in Table 5.2.

$$f_{\mathrm{RF}} = 4f_{\mathrm{PLL}} + f_{\mathrm{IF}} = 4f_{\mathrm{PLL}} + 2.4576 \quad \text{(GHz)} \tag{5.1}$$

where f_{PLL} is the frequency of the PLL output clock signal and f_{IF} is the IF carrier frequency.

A low-noise amplifier (LNA) and a power amplifier (PA) amplify the RF signal before feeding it to the antenna. The power measured at the PA output is about 4 dBm/160.32 MHz for single-input single-output (SISO) cases.

Each RRU uses one in-house developed stacked air-filled substrate-integrated-waveguide (AFSIW) aperture-coupled cavity-backed patch antenna to transmit the RF signal. The compact antennas are implemented using the technology

Optical signal bit rate (Gbps)		9.8304		
CDR output freq. (MHz)		4915.2 (9830.4/2)		
Clock divider output freq. (MHz)		24.576 (4915.2/200)		
PLL output freq. (MHz)	5406.72	5652.48	6144.00	6635.52
Carrier freq. (RF) (GHz)	24.08	25.07	27.03	29.00

Table 5.2: Frequency at the output of each stage of the clock path.

described in [20, 21]. They exhibit a radiation efficiency (η_{rad}) higher than 90% and are matched to a 50 Ω impedance between 23.25 GHz to 30.25 GHz.

Receiver and Signal Processing

The receiver uses the same antenna as the RRUs. The antenna is first connected to an LNA. The amplified received signal is filtered by a BPF with a passband from 23.55 GHz to 31.85 GHz and down-converted to 2.4576 GHz using the down-converter evaluation board *Analog Devices* EVAL-ADMV1014. Then, the IF signal is filtered by a BPF with a passband from 2.3 GHz to 2.6 GHz. An analog front-end evaluation kit (*Analog Device FMCOMMS1-EBZ*) down-converts the IF signal to baseband and samples the baseband signal at 327.68 MHz. A *Xilinx Kintex 7* FPGA (KC705) collects the data for offline signal processing using MATLAB.

The signal processing includes OFDM frame boundary detection, carrier frequency offset (CFO) correction [22], fast Fourier transform (FFT), least-squares channel estimation [23], and QAM demodulation. The demonstration workflow illustrated in Fig. 5.4 is fully realized in MATLAB. Ideal channel information feedback is assumed. The CFRs estimated during the training

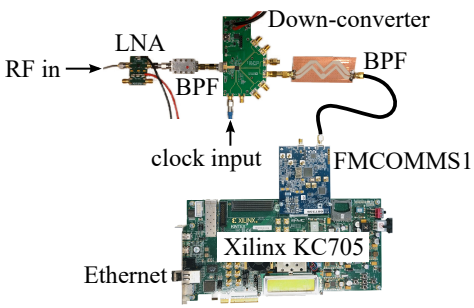

Figure 5.3: Receiver. (LNA: low-noise amplifier; BPF: band-pass filter.)

phase are used to generate precoded data. At the receivers, after canceling the effect of the channel and the CFO, the received data is demodulated.

5.2.2 MISO OFDM Signals

The OFDM signal parameters used in the demonstration are summarized in Appendix A. In our demonstration, two RRUs are employed. As such, the received baseband data (in the frequency domain) on a subcarrier k can be written as

$$\mathrm{R}_k = \mathrm{H}_{1,k}\,\mathrm{X}_{1,k} + \mathrm{H}_{2,k}\,\mathrm{X}_{2,k} + \mathrm{W}_k \tag{5.2}$$

where all elements in (5.2) are complex numbers; $\mathrm{H}_{i,k}$ denotes the equivalent channel frequency response (CFR) in baseband between RRU i and the receiver; $\mathrm{X}_{i,k}$ is the precoded baseband data transmitted by RRU i; W_k is the additive noise.

The workflow has two phases as shown in Fig. 5.4: the training and data transmission phases.

Training Phase

During this phase, frequency-interleaved training sequences[2] for channel estimation are transmitted; for each subcarrier, within one given OFDM frame, either RRU 1 or RRU 2 transmits QPSK data while the other one transmits zeros. First, the algorithm described in [22] is applied to estimate the CFO. The CFRs are estimated using the least-squares channel estimation algorithm [23]. The training sequences should last at least two OFDM frames for the case with two RRUs. The path with the lower path loss is selected as the main path. Without loss of generality, the RRU transmitting the signal via the main path is named RRU 1.

Data Transmission Phase

During this phase, RRU 1 transmits the original OFDM signal while RRU 2 transmits the precoded signal. The precoding guarantees that the signals from two RRUs combine constructively at the receiver.

5.3 Measurement Results

In this section, first, the performance of the proposed SD-IFoF link is provided. Wide-bandwidth OFDM signals were transmitted through the complete signal

[2] See Appendix A.

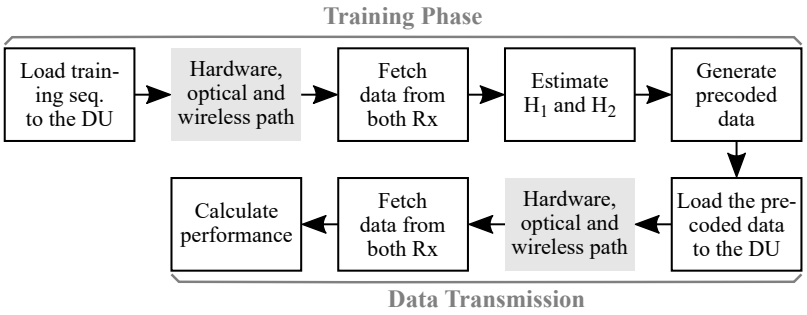

Figure 5.4: Measurement workflow.

chain but without wireless paths. We also present measurement results to show that the carrier frequency synchronism was maintained in our setup. Second, the 2×1 MISO performance was measured by transmitting signals modulated at 25.07 GHz in a typical office environment; the SISO performance is provided as a baseline. In the end, we evaluate the performance degradation due to asynchronous phase noise. The performance is presented in error vector magnitude (EVM) normalized to the average constellation power.

5.3.1 Link Performance

To show the quality of the SD-IFoF link, we measured the performance without wireless paths. The output of the up-converter EVAL-ADMV1013 was connected directly to the input of the down-converter EVAL-ADMV1014. The output amplitude of the up-converter was properly adjusted to prevent the receiver chain from saturating. The same reference clock was provided for the up- and down-converters using one PLL, i.e. there was no CFO.

Fig. 5.5 plots the EVM values against the RF carrier frequencies. The carrier frequency could be easily adjusted by configuring the PLL output frequency while the rest of the hardware remained the same. Hence, there was no significant performance difference in terms of EVM when applying different carrier frequencies.

For optical back-to-back cases (with only the breakout fibers), the average EVM values are 4.74% (-26.48 dB), 5.73% (-24.84 dB), and 6.31% (-24.00 dB) for the 160.32 MHz-, 249.92 MHz-, and 299.20 MHz-bandwidth OFDM signal (64-QAM), respectively. As the signal bandwidth increases, the performance degradation is expected because of two reasons. First, when the total transmitted signal power is kept the same, the power spectral density (PSD) of the signal decreases as the signal bandwidth increases. Because the noise PSD stays the same, the SNR drops accordingly. Second, the oversam-

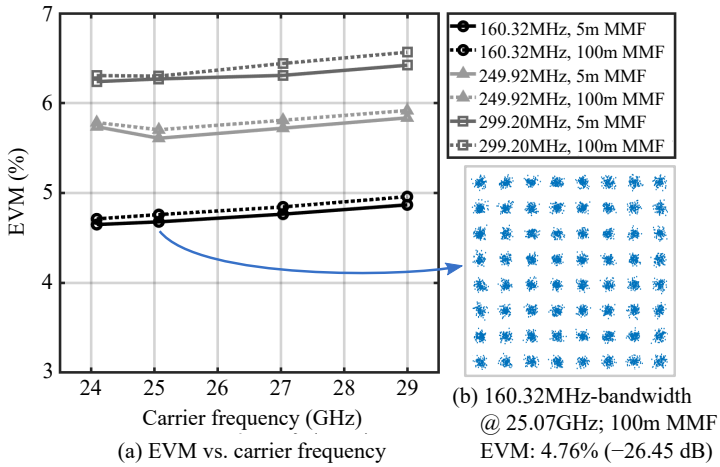

(a) EVM vs. carrier frequency

(b) 160.32MHz-bandwidth @ 25.07GHz; 100m MMF EVM: 4.76% (−26.45 dB)

Figure 5.5: SD-IFoF link quality: measured EVM vs. carrier frequency (GHz). It is measured with 5 m (optical back-to-back) and 100 m multi-mode fibers (MMF) without wireless paths.

pling ratio (OSR), defined as:

$$\mathrm{OSR} = \frac{f_{\Sigma\Delta}/2}{\mathrm{BW}}, \tag{5.3}$$

decreases as the signal bandwidth (BW) increases thus resulting in a lower signal-to-quantization-noise ratio (SQNR); $f_{\Sigma\Delta}$ is the sample rate of the SDM.

The EVM values were higher when transmitting over a 100 m MMF. Nonetheless, the 6.40% EVM of the 299.20 MHz-bandwidth OFDM signals transmitted over a 100 m MMF is lower than the 3GPP EVM requirement for 64-QAM: 8% (−21.94 dB) [3].

The optical bitrate efficiency, calculated by dividing the transmitted data bandwidth by the bit rate over fiber, is 30.44 MHz / Gbps (299.20 MHz / 9.8304 Gbps). Using the example in [24], the bitrate efficiency of CPRI is 27.12 MHz / Gbps. The proposed SD-IFoF architecture decreases the RRU complexity while maintaining the same optical bitrate efficiency as CPRI.

5.3.2 RRU Synchronism

To validate the frequency synchronism between RRUs, the output clock signals of the PLLs were measured by a *Keysight* real-time oscilloscope (DSAZ634A). Fig. 5.6a shows the captured waveforms; the output of PLL 1 was used as the trigger signal. Fig. 5.6b and Fig. 5.6c are the real-time eye diagrams for about

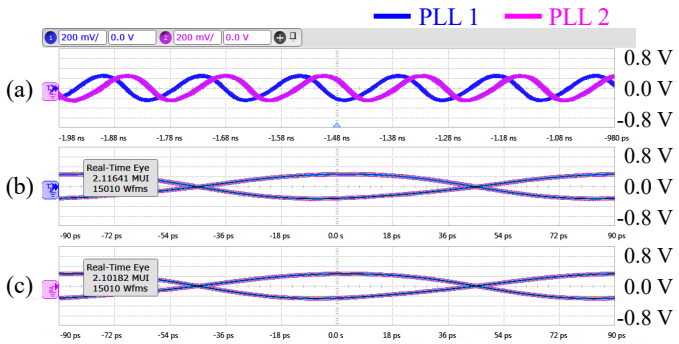

Figure 5.6: PLL output signals measured by a real-time oscilloscope. (a) Captured waveforms using the output of PLL 1 as the trigger signal; (b) and (c): real-time eye diagrams of PLL 1 and PLL 2 for about 15000 frames.

15000 frames. It can be seen from the captured waveforms and the real-time eye diagrams that the RRUs were frequency-synchronized.

5.3.3 Distributed MISO Performance

The combined optical-wireless performance was measured with a 100 m MMF between the DU and each RRU. Fig. 5.7 shows the simplified layout of the measurement environment and the measured EVM values. The two RRUs were 1 m away from each other. No common reference clocks were provided to the DU, RRUs, and receiver. The CFO between the RRUs and the receiver was estimated and compensated offline using MATLAB [22].

The receiver locations and the directions of the antennas are illustrated in the figure. For the MISO cases, the transmission power per antenna was decreased to half of the power of a single antenna for the SISO cases by adding 3 dB attenuators between the power amplifiers and the RRU antennas. The SISO links between the receiver and both RRU 1 and RRU 2 were measured, but only the lower EVM value of the two is presented for comparison.

We measured 64-QAM OFDM signals with a 160.32 MHz signal bandwidth. The average EVM of all SISO cases was 7.19% (-22.86 dB) and 6.31% (-24.00 dB) for MISO. The gain was about 1.12 dB. For some antenna locations, it was possible to transmit higher-bandwidth signals. 160.32 MHz was chosen for ease of comparison so that all cases could receive 64-QAM signals.

The two RRUs were placed 2 m away from each other in the second measurement scenario (Fig. 5.8). The first three receiver locations were selected for comparison and the performance is summarized in Table 5.3.

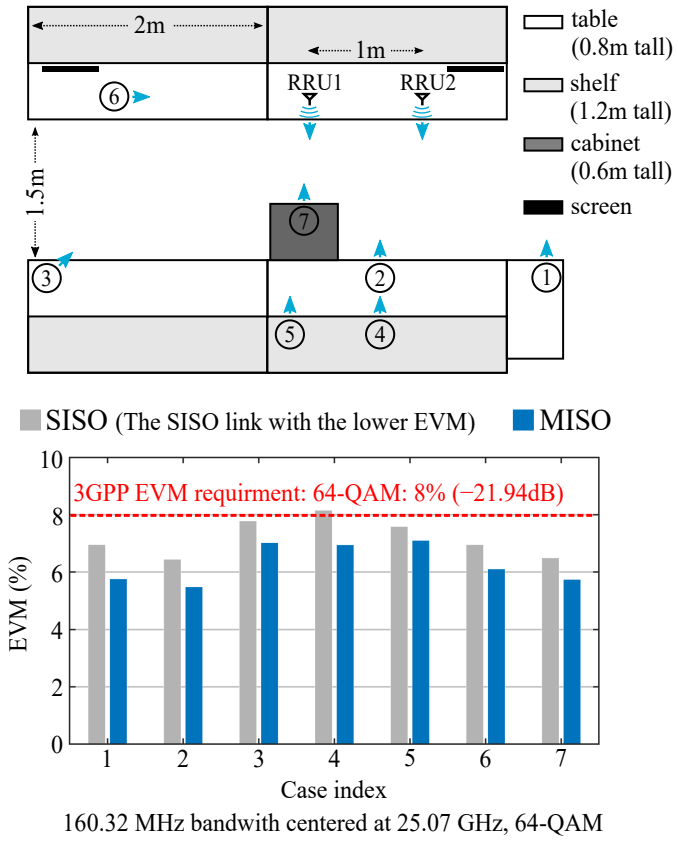

Figure 5.7: Simplified layout of the measurement environment and the distributed antenna system performance. The circled numbers denote different receiver locations. Each case in the bar chart corresponds to one receiver location.

Case 1: When the RRU distance was 1 m, a good gain of 1.63 dB was observed. However, when RRU 1 was moved away from the receiver, the receiver was mainly served by RRU 2. The MISO performance was worse than the SISO because the transmission power of RRU 2 in the SISO cases was doubled with respect to the MISO transmission.

Case 2: The receiver could receive good quality signals from RRU 1 and RRU 2 for both RRU distances, thus the MISO performance was similar.

Case 3: When the RRU distance was 1 m, both antennas were quite far from the receiver. A gain was observed but the EVM value was among the higher ones. When RRU 1 was moved closer to the receiver, the performance im-

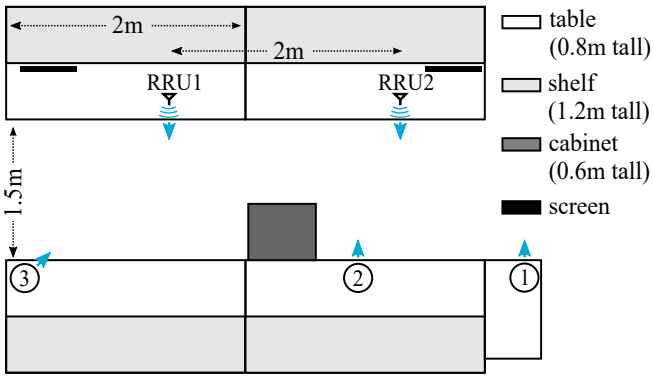

Figure 5.8: Simplified layout of the measurement environment. The circled numbers denote different receiver locations.

RRU distance	Case index	1	2	3
1 m	SISO	6.95%	6.44%	7.78%
	MISO	5.76%	5.48%	7.02%
	Gain (dB)	1.63	1.40	0.89
2 m	SISO	6.50%	6.15%	6.44%
	MISO	7.11%	5.18%	6.02%
	Gain (dB)	−0.77	1.35	0.59

Table 5.3: EVM comparison between two different RRU distances.

proved significantly. The gain was less obvious for the same reason as Case 1: the receiver was mainly served by RRU 1 and the transmission power per RRU was stronger while measuring SISO cases.

When the RRUs are further apart, the channel condition between an RRU to a receiver will be more diverse. The received signal quality would be better if the receiver is mainly served by the RRUs whose signals can arrive at the receiver via good-conditioned channels. Thus, the applied precoding scheme—keeping the transmission power per antenna for the MISO cases equal to half of the SISO transmission power—was not optimized. E.g., for Case 1, when the two RRUs were 2 m apart, it would be more beneficial if the receiver was served by mainly RRU 2. Instead of keeping the same transmission power per antenna, distributing the transmission power based on the channel qualities can offer more flexibility.

5.3.4 Impact of Asynchronous Phase Noise

This subsection evaluates the performance degradation due to the asynchronous phase noise introduced by the two PLLs. Note that the two RRUs were frequency-synchronous, as shown in Fig. 5.6. The "asynchronous" and "synchronous" in this subsection refer to the phase noise.

In Table 5.4, the "Asynchronous RRUs" rows list the MISO performance presented in Fig. 5.7. The reference clock signals for the up-converters at the two RRUs were independently generated by PLLs, so asynchronous phase noise was introduced. The results listed in the "Synchronous RRUs" rows are measured by using the output of the PLL at RRU 1 for the up-converters of both RRUs.

Performance loss ranging from 0.35 to 0.83 dB was observed except for Case 6. For Case 6, the receiver was mainly served by one RRU and the signal from the other RRU was not dominating. This resulted in the close performance for both the synchronous and asynchronous cases. Chapter 7 will provide the simplified derivation and simulation result of the performance degradation due to inaccurate digital beamforming phases.

Case index	1	2	3	4
Asynchronous RRUs:				
EVM (%)	5.76	5.48	7.02	6.95
EVM (dB)	(−24.79)	(−25.22)	(−23.07)	(−23.16)
Synchronous RRUs:				
EVM (%)	5.53	4.98	6.71	6.34
EVM (dB)	(−25.14)	(−26.05)	(−23.47)	(−23.95)
Performance loss (dB)	0.35	0.83	0.4	0.79
Case index	5	6	7	
Asynchronous RRUs:				
EVM (%)	7.10	6.11	5.74	
EVM (dB)	(−22.97)	(−24.28)	(−24.82)	
Synchronous RRUs:				
EVM (%)	6.70	6.14	5.47	
EVM (dB)	(−23.47)	(−24.23)	(−25.25)	
Performance loss (dB)	0.5	−0.05	0.43	

Table 5.4: MISO performance comparison between asynchronous and synchronous RRUs

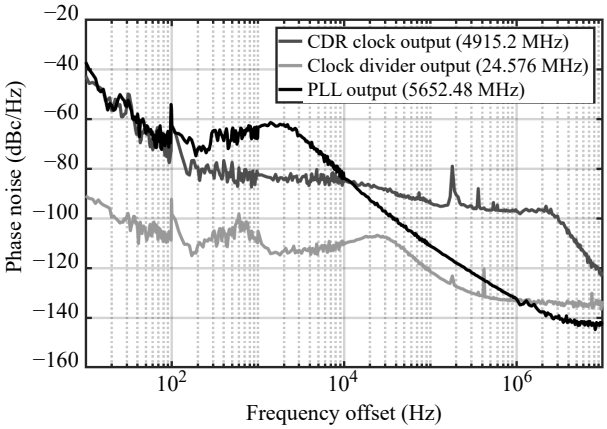

Figure 5.9: Measured phase noise.

The measured phase noise was plotted in Fig. 5.9. The PLLs introduced considerably large phase noise. We expect a performance improvement if better PLLs are used.

5.4 Conclusion

This chapter demonstrated a fully implemented 2×1 distributed MISO OFDM downlink system using real-time SD-IFoF links. The OFDM baseband signals were sigma-delta modulated and digitally up-converted to an intermediate frequency around 2.5 GHz on an FPGA. The signals were transmitted over multi-mode fibers using a commercial QSFP module. At each remote radio unit, the clock information contained in the sigma-delta modulated signal was retrieved using a clock and data recovery module. This architecture guarantees the frequency synchronism between remote radio units and requires no extra reference clock signal for synchronization.

The performance of the SDoF link satisfied the 3GPP error vector magnitude (EVM) requirement for 64-QAM (8%): the average EVM of 299.20 MHz-bandwidth OFDM signals over a 100 m multi-mode fiber was 6.40% (-23.88 dB) for different carrier frequencies ranging from 24 GHz to 29 GHz. The same hardware implementation was used for different signal bandwidths and the carrier frequency could be easily adjusted by configuring the phase lock loops (PLLs), proving that the SD-IFoF link is highly flexible. For the MISO measurements, an average gain of 1.12 dB was observed despite the performance degradation due to asynchronous phase noise introduced by the independent PLLs.

References

[1] T. Wang *et al.*, "Spectrum Analysis and Regulations for 5G," in *5G Mobile Communications*, W. Xiang *et al.*, Eds. Switzerland: Springer International Publishing, 2017, pp. 27–50.

[2] Qualcomm, "Global Update on Spectrum for 4G & 5G," 2020, last accessed on Jul. 6, 2022. Available on URL: https://www.qualcomm.com/media/documents/files/spectrum-for-4g-and-5g.pdf

[3] "3GPP TS 38.104. New Radio (NR): Base Station (BS) Radio Transmission and Reception (Release 17) (V17.6.0)," June 2022.

[4] T. S. Rappaport *et al.*, "State of the Art in 60-GHz Integrated Circuits and Systems for Wireless Communications," *Proceedings of the IEEE*, vol. 99, no. 8, pp. 1390–1436, 2011.

[5] F. Huang *et al.*, "Propagation Characteristics of Indoor Radio Channel from 3.5 GHz to 28 GHz," in *Proc. 2016 IEEE 84th Vehicular Technology Conference (VTC)*, 2016, pp. 1–5.

[6] S. Sun *et al.*, "MIMO for Millimeter-Wave Wireless Communications: Beamforming, Spatial Multiplexing, or Both?" *IEEE Communications Magazine*, vol. 52, no. 12, pp. 110–121, 2014.

[7] E. J. Violette *et al.*, "Millimeter-Wave Propagation at Street Level in an Urban Environment," *IEEE Transactions on Geoscience and Remote Sensing*, vol. 26, no. 3, pp. 368–380, 1988.

[8] A. F. Elrefaie and M. Shakouri, "Propagation Measurements at 28 GHz for Coverage Evaluation of Local Multipoint Distribution Service," in *Proc. 1997 Wireless Communications Conference*, 1997, pp. 12–17.

[9] M. Sung *et al.*, "5G Trial Services Demonstration: IFoF-Based Distributed Antenna System in 28 GHz Millimeter-Wave Supporting Gigabit Mobile Services," *Journal of Lightwave Technology*, vol. 37, no. 14, pp. 3592–3601, 2019.

[10] U. Habib *et al.*, "Analog Radio-over-Fiber Supported Increased RAU Spacing for 60 GHz Distributed MIMO Employing Spatial Diversity and Multiplexing," *Journal of Lightwave Technology*, vol. 36, no. 19, pp. 4354–4360, 2018.

[11] N. Argyris *et al.*, "A 5G mmWave Fiber-Wireless IFoF Analog Mobile Fronthaul Link with up to 24-Gb/s Multiband Wireless Capacity," *Journal of Lightwave Technology*, vol. 37, no. 12, pp. 2883–2891, 2019.

[12] E. Ruggeri *et al.*, "A 5G Fiber Wireless 4 Gb/s WDM Fronthaul for Flexible 360° Coverage in V-Band Massive MIMO Small Cells," *Journal of Lightwave Technology*, vol. 39, no. 4, pp. 1081–1088, 2021.

[13] K. Kanta *et al.*, "Demonstration of a Hybrid Analog-Digital Transport System Architecture for 5G and Beyond Networks," *Applied Sciences*, vol. 12, no. 4, 2022.

[14] P. T. Dat *et al.*, "Radio-on-Radio-over-Fiber: Efficient Fronthauling for Small Cells and Moving Cells," *IEEE Wireless Communications*, vol. 22, no. 5, pp. 67–75, 2015.

[15] L. Cheng *et al.*, "Coordinated Multipoint Transmissions in Millimeter-Wave Radio-over-Fiber Systems," *Journal of Lightwave Technology*, vol. 34, no. 2, pp. 653–660, 2016.

[16] H. Li *et al.*, "Real-Time 100-GS/s Sigma-Delta Modulator for All-Digital Radio-over-Fiber Transmission," *Journal of Lightwave Technology*, vol. 38, no. 2, pp. 386–393, 2020.

[17] ——, "A 21-GS/s Single-Bit Second-Order Delta-Sigma Modulator for FPGAs," *IEEE Transactions on Circuits and Systems II: Express Briefs*, vol. 66, no. 3, pp. 482–486, 2019.

[18] A. Frappé *et al.*, "An All-Digital RF Signal Generator Using High-Speed $\Sigma\Delta$ Modulators," *IEEE Journal of Solid-State Circuits*, vol. 44, no. 10, pp. 2722–2732, 2009.

[19] C.-Y. Wu *et al.*, "Real-Time 4×3.5 Gbps Sigma Delta Radio-over-Fiber for a Low-Cost 5G C-RAN Downlink," in *Proc. 44th European Conference on Optical Communication (ECOC 2018)*, 2018, pp. 1–3.

[20] Q. Van den Brande *et al.*, "Highly Efficient Impulse-Radio Ultra-Wideband Cavity-Backed Slot Antenna in Stacked Air-Filled Substrate Integrated Waveguide Technology," *IEEE Transactions on Antennas and Propagation*, vol. 66, no. 5, pp. 2199–2209, 2018.

[21] I. Lima de Paula *et al.*, "Cost-Effective High-Performance Air-Filled SIW Antenna Array for the Global 5G 26 GHz and 28 GHz Bands," *IEEE Antennas and Wireless Propagation Letters*, vol. 20, no. 2, pp. 194–198, 2021.

[22] A. N. Mody and G. L. Stuber, "Synchronization for MIMO OFDM Systems," in *Proc. 2001 IEEE Global Communications Conference (GLOBECOM '01)*, vol. 1, 2001, pp. 509–513.

[23] J.-J. van de Beek *et al.*, "On Channel Estimation in OFDM Systems," in *Proc. 1995 IEEE 45th Vehicular Technology Conference. Countdown to the Wireless Twenty-First Century*, vol. 2, 1995, pp. 815–819.

[24] "Common Public Radio Interface: eCPRI Interface Specification V2.0," 2019, last accessed on Jul. 6, 2022. Available on URL: http://www.cpri.info/spec.html

6

Bit-Interleaved SDoF Based Distributed Antenna System for Sub-6 GHz Bands

This chapter introduces another distributed antenna system (DAS) architecture for sub-6 GHz bands. This DAS is more scalable in terms of the number of the supported antennas. In the proposed system, two remote radio units (RRUs) are connected to the central site by a network enabled by the bit-interleaved sigma-delta-over-fiber (BI-SDoF) concept: multiple sigma-delta modulated baseband signals are time-interleaved into one non-return-to-zero (NRZ) signal. The NRZ signal is then converted to the optical domain and transmitted over fiber. Both the downlink and uplink data paths have been implemented.

This chapter is based on two publications: A preliminary setup was demonstrated online for the 46th European Conference on Optical Communication (ECOC 2020). The measurement results have later been published in *Applied Sciences*.

1. **Chia-Yi Wu**, Caro Meysmans, Haolin Li, *et al.*, "Demonstration of a Scalable Distributed Antenna System Using Real-Time Bit-Interleaved Sigma-Delta-over-Fiber Architectures," in *Proceedings of the 46th European Conference on Optical Communication (ECOC 2020)*, Brussels (online), Belgium, 2020.

2. **Chia-Yi Wu**, Haolin Li, Joris Van Kerrebrouck, *et al.*, "A Bit-Interleaved Sigma-Delta-over-Fiber Fronthaul Network for Frequency-Synchronous Distributed Antenna Systems," *Applied Sciences*, 2021.

6.1 Introduction

Massive multiple-input multiple-output (MIMO) is a key technology to increase wireless spectral efficiency and radiated energy efficiency for 5G [1–3]. 6G considers spectral efficiency as one of the key performance indicators (KPIs). It expects the peak spectral efficiency to double and the experienced spectral efficiency to increase tenfold [4]. Cell-free massive MIMO, also traditionally known as distributed massive MIMO, has attracted wide attention [3–5] because the distributed scheme can further improve the spectral efficiency and user fairness [6].

To enable cell-free massive MIMO, we expect the fronthaul networks to have a high capacity, high scalability (in terms of the supported signal bandwidth and the number of supported antennas), low latency, and low deployment costs. Most importantly, the network should provide precise synchronization between different remote units in both time and frequency [7].

The fronthaul network of the proposed DAS is enabled by the BI-SDoF concept, introduced in Subsection 3.2.3. While increasing the scalability in terms of the number of supported antennas, the network keeps one of the most desirable characteristics of digitized radio-over-fiber (DRoF)—NRZ signals over fiber. Therefore, it has high linearity tolerances on both electrical and optical components. Compared to the architecture introduced in Chapter 4, it can support more remote antennas via one fiber. Furthermore, the RRU complexity remains relatively low in contrast to those of DRoF-based networks.

Similar to the IFoF-based architecture introduced in Chapter 5, this DAS also extracts the clock information contained in the downlink bitstreams for synchronization. With the help of synchronization circuits, this implementation successfully deals with an essential challenge: precise frequency synchronization of different remote units. Owing to the straightforward data paths, all transceivers inherently transmit or receive with fixed timing offsets which can be easily calibrated.

This chapter is organized as follows: Section 6.2 introduces the DAS architecture. Section 6.3 provides the measurement results with discussions, which show the achievable signal quality and validate the synchronization performance.

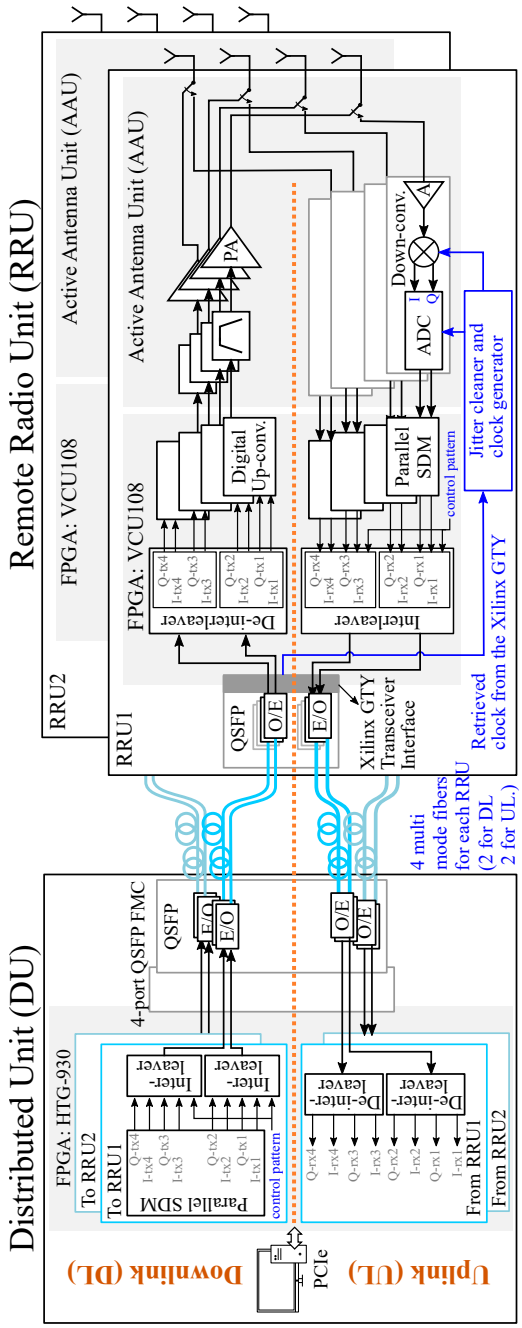

Figure 6.1: System architecture. (PCIe: peripheral component interconnect express; SDM: sigma-delta modulator; FMC: FPGA mezzanine card; E/O / O/E: electrical-to-optical/optical-to-electrical converter; Up-/Down-conv.: up-/down-conversion; PA: power amplifier; A: low-noise amplifier; ADC: analog-to-digital converter.

6.2 System Architecture

The setup has one central site—the distributed unit (DU)—and two RRUs. Fig. 6.1 illustrates the block diagram and Table 6.1 lists all the hardware components.

The DU (Fig. 6.2a) comprises a personal computer (PC) and a *Hitech Global* HTG-930 board, which connects to the PC via the peripheral component interconnect express (PCIe) interface and has a *Xilinx Virtex UltraScale+* FPGA (VU13P). The board is connected to a four-port QSFP FMC module. (FMC: FPGA mezzanine card.) This PC is also used for performance monitoring. Each RRU (Fig. 6.2b) consists of a *Xilinx Virtex Ultrascale* FPGA (VCU108) and an active antenna unit (AAU), which is in-house developed and has four

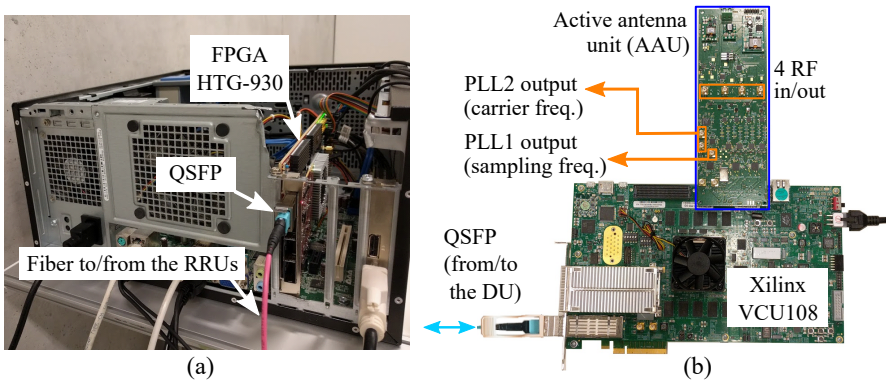

Figure 6.2: Photos of (a) the distributed unit (DU) and (b) a remote radio unit (RRU). The phase lock loop (PLL) outputs are used for debugging and performance monitoring.

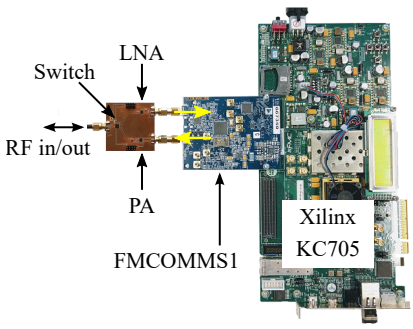

Figure 6.3: Photo of the mobile user.

Remote radio unit (active antenna unit)	
switch	*Analog Devices* HMC8038
band-pass filter (BPF)	*Mini-Circuits* BFCV–3641+
power amplifier (PA)	*Analog Devices* HMC327
low-noise amplifier (LNA)	*Mini-Circuits* PMA3-83LNW+
down-converter	*Analog Devices* ADL5380
analog-to-digital converter (ADC)	*Analog Devices* AD9633
crystal oscillator	*Crystek* CVHD–950–122.880
phase lock loop (PLL)	
PLL1 (Fig. 6.2)	*Analog Devices* AD9524
PLL2 (Fig. 6.2)	*Analog Devices* ADF4356
User	
analog front-end evaluation kit	*Analog Devices* FMCOMMS1-EBZ
switch	*Analog Devices* HMC8038
power amplifier (PA)	*Analog Devices* HMC327
low-noise amplifier (LNA)	*Mini-Circuits* PMA3-83LN+

Table 6.1: Hardware components.

wireless transceivers.

The DU is connected to the RRUs with BI-SDoF links, in which baseband signals are sigma-delta modulated and time-interleaved before being transmitted over fiber. Considering the targeted use cases and the implementation cost, this setup uses multi-mode fibers (MMFs) and commercial QSFP-100G-SR4 modules. Each QSFP has four 850 nm vertical-cavity surface-emitting lasers (VCSELs) and built-in clock-and-data recovery modules (CDRs) for transmitting and receiving. To serve all four transceivers on one RRU, two MMFs are used for the downlink transmission and two others for the uplink between the DU and each RRU.

If a longer transmission distance is required, single-mode fibers (SMFs) can be used instead. As NRZ signals are transmitted over fiber, the impact of fiber nonlinearities can be viewed as optical bit errors. Section 6.3 will further show the high bit error tolerance of sigma-delta modulated signals. Consequently, we expect similar performance when using SMFs.

Although the block diagram (Fig. 6.1) seems complicated due to the provided details, the hardware is actually straightforward and can easily be incorporated in an application-specific integrated circuit (ASIC).

A user (Fig. 6.3) has a *Xilinx Kintex 7* FPGA (KC705), an analog front end evaluation kit (*Analog Device* FMCOMMS1-EBZ), and a printed circuit board (PCB), which contains a low-noise amplifier (LNA) for reception, a power amplifier (PA) for transmission, and a switch.

6.2.1 Downlink Data Path

The downlink (DL) data goes first from the DU to an RRU via an optical link and then from an RRU antenna [8] to a user as shown in the upper half of Fig. 6.1. The signals for transmission are provided to the DU FPGA by the PC via the PCIe interface; to collect the received signals for performance monitoring, the user is connected to the PC via Ethernet.

On the DU FPGA, sixteen parallel low-pass sigma-delta modulators (SDMs) are implemented to serve two RRUs as four I-Q pairs are required by each RRU; the SDMs modulate the baseband signals at 3.6864 Gbps. (I: in-phase; Q: quadrature; Gbps: gigabit per second.) As illustrated in Fig. 6.4, every four bi-level sigma-delta modulated signals, i.e., two pairs of sigma-delta modulated I and Q signals, are time-interleaved together with one bi-level control sequence into one NRZ signal, which is converted to the optical domain and transmitted over one fiber by a QSFP.

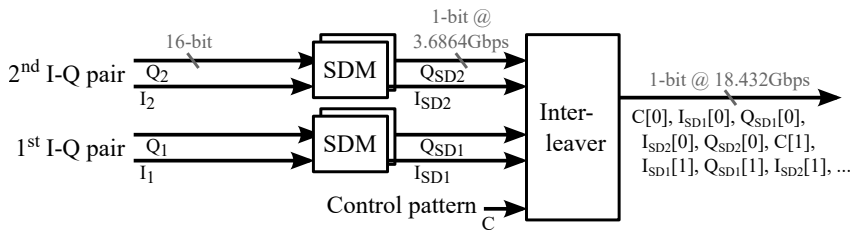

Figure 6.4: Illustration of the bit-interleaving process. (SDM: sigma-delta modulators.)

At each RRU, a QSFP converts the received 18.432 Gbps bitstreams from the optical domain to the electrical domain. On the FPGA, each bitstream is first de-interleaved back to two pairs of 3.6864 Gbps sigma-delta modulated I and Q signals; the signals are then up-sampled and digitally up-converted to the carrier frequency as depicted in Fig. 3.9a. Afterwards, band-pass filters on the AAU filter out the quantization noise. The radio-frequency (RF) signals are amplified and sent to antennas.

The DL data passes only simple and non-blocking modules; the signals are in fact streamed directly from the DU to all antennas. As a result, the transmission timing offsets between them, which may come from hardware mismatches

or the locked phases of the phase lock loops (PLLs), are inherently fixed, although there is no absolute time shared between all transmitters. Such offsets can either be calibrated or contained in the estimated channel information. The transmission timings can then be considered synchronous.

At the user, the received signals are amplified by the LNA, down-converted using a zero intermediate frequency (zero-IF) receiver, and sampled. The FPGA collects the sampled data whose quality is later checked by the PC.

6.2.2 Uplink Data Path

The uplink (UL) data goes from a user to RRUs wirelessly and then from RRUs to the DU via the optical links as depicted in the lower half of Fig. 6.1. The digital baseband signal to be transmitted is loaded to the user via Ethernet. The FPGA streams the digital signal to the FMCOMMS1-EBZ which converts the signal to an RF analog signal for transmission.

At an RRU, the AAU amplifies, down-converts, and samples the RF signals received by its antennas. The baseband signals, sampled at 92.16 MSps (megasamples per second) by the analog-to-digital converters (ADCs), are subsequently up-sampled and sigma-delta modulated at 3.6864 Gbps by the FPGA. Every two sigma-delta modulated I-Q pairs and one control sequence are time-interleaved and transmitted to the DU over one fiber. The DU QSFP converts the NRZ signals back to the electrical domain. The DU FPGA de-interleaves the electrical signals, filters out the quantization noise, and down-samples the signals to 81.92 MSps. The PC collects the data via the PCIe interface. Similar to the DL, the transparency of the data path guarantees that the UL data is received simultaneously by all antennas at RRUs and streamed directly to the DU. This attribute is especially important for the uplink channel estimation [9].

6.2.3 Synchronization Circuit

To guarantee frequency synchronism between RRUs, a synchronization circuit is implemented on every AAU. For each RRU, the CDR of the *Xilinx GTY* transceiver retrieves the clock information from the DL bitstream and generates a 30.72 MHz clock. The retrieved 30.72 MHz clock goes to the AAU. However, the jitter of this clock is high due to the mediocre performance of the on-FPGA PLLs.

The synchronization circuit comprises two PLLs (Fig. 6.5). The first PLL (PLL1) functions as a jitter cleaner and generates a low-jitter 92.16 MHz clock, which provides the sample clock of ADCs and the reference clock for the second PLL (PLL2). PLL2 generates the carrier clock for down-conversion.

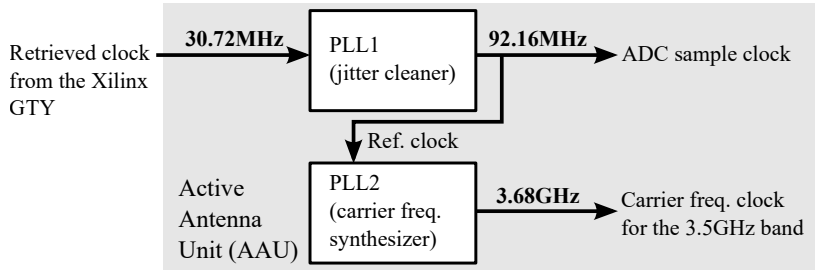

Figure 6.5: Block diagram of the synchronization circuit. (ADC: analog-to-digital converter; PLL: phase lock loop.)

6.3 Experimental Methodology and Measurement Results

Python-generated orthogonal frequency-division multiplexing (OFDM) baseband signals are used for both the DL and UL transmission for ease of implementation. The related parameters are included in Appendix A.

Through extensive measurements, this section demonstrates two main advantages of the proposed architecture: (1) BI-SDoF links can deliver good quality data, which meets the 3GPP error vector magnitude (EVM) requirement for 256-QAM (3.5%) [10]; (2) the BI-SDoF-based network guarantees the frequency synchronism between RRUs without an extra reference clock signal provided.

6.3.1 Link Performance

The link performance was measured by transmitting 40.96 MHz-OFDM signals (256-QAM) centered at 3.6864 GHz. The EVM values are normalized to the average constellation power.

1. DL: from the DU to an RRU via an optical link with different fiber lengths, then from an RRU RF in / out port to a user (electrical back-to-back);

2. UL: from a user to an RRU RF in / out port (electrical back-to-back), then from the RRU to the DU via an optical link with different fiber lengths.

The combined length of the break-out fibers, and therefore the fiber length of the optical back-to-back cases, was about 8 m. The RF in / out port of the

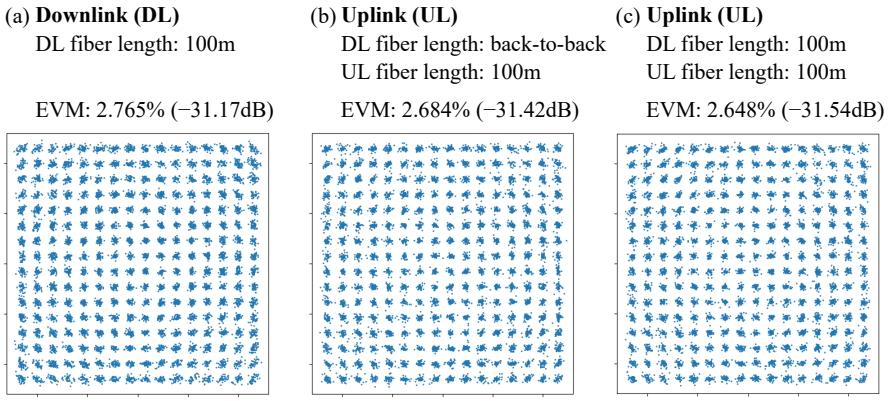

Figure 6.6: Constellation diagrams of the demodulated OFDM signals of the worst cases of the downlink (Table 6.2) and uplink performance measurements (Table 6.3).

RRU and the user were connected directly with a cable. Appropriate attenuation was applied to prevent the receivers from saturation. No reference clock was provided; the carrier frequency offset was estimated and canceled using the algorithm proposed in [11].

Downlink Performance

Table 6.2 lists the measured EVM values corresponding to different DL fiber lengths. Due to the high bit-error rate (BER) tolerance of sigma-delta modulated signals [12, 13], there is little performance degradation when the optical transmission distance increases. A BER up to 2×10^{-4} can be tolerated in sigma-delta-over-fiber (SDoF) applications; the corresponding signal quality is about −45 dB EVM [13]. The constellation diagram of the worst case—with a 100 m MMF added between the break-out fibers—can be found in Fig. 6.6a.

	DL (DU to RRU) fiber length		
	Back-to-Back	**30 m MMF**	**100 m MMF**
EVM	2.725% (−31.29 dB)	2.752% (−31.21 dB)	2.765%[1] (−31.17 dB)

[1] Constellation: Fig. 6.6a.

Table 6.2: Downlink performance in EVM.

Uplink Performance

Pseudorandom binary sequences (PRBSs) were transmitted over the DL fiber to keep the CDR at the RRU locked. Therefore, the DL fiber length was expected to have an impact on the phase noise of the retrieved clock. Two scenarios with different DL fiber lengths were considered when measuring the UL performance: (1) back-to-back; (2) with a 100 m MMF. Table 6.3 lists the measured EVM values corresponding to different UL fiber lengths under these two scenarios. Fig. 6.6b and c show the corresponding constellation diagrams.

As in Table 6.2, there is little performance degradation when the UL optical transmission distance increases. The performance difference between the two scenarios is also negligible.

	UL (DU to RRU) fiber length		
	Back-to-Back	**30 m MMF**	**100 m MMF**
DL Back-to-Back	2.615% (−31.65 dB)	2.672% (−31.46 dB)	2.684%[1] (−31.42 dB)
DL 100 m MMF	2.621% (−31.63 dB)	2.641% (−31.56 dB)	2.648%[2] (−31.54 dB)

[1] Constellation: Fig. 6.6b.
[2] Constellation: Fig. 6.6c.

Table 6.3: Uplink performance in EVM.

6.3.2 RRU Synchronism

Three experiments were performed to demonstrate the RRU synchronism. The jitter measurement showed the carrier frequency stability over time and provided the asynchronous jitter information in the time domain. The spectrum measurement illustrated the asynchronous phase noise spectrum in the frequency domain. The last one calculated the average phase difference between two RRUs using the estimated channel frequency responses (CFRs).

After we published the measurement results on *Applied Sciences* [14], the old AAUs were worn-out due to long use and the performance became unstable. Therefore, we fabricated new ones. Since the measurements of Part III were performed with the new AAUs, we also redid the measurements for this subsection.

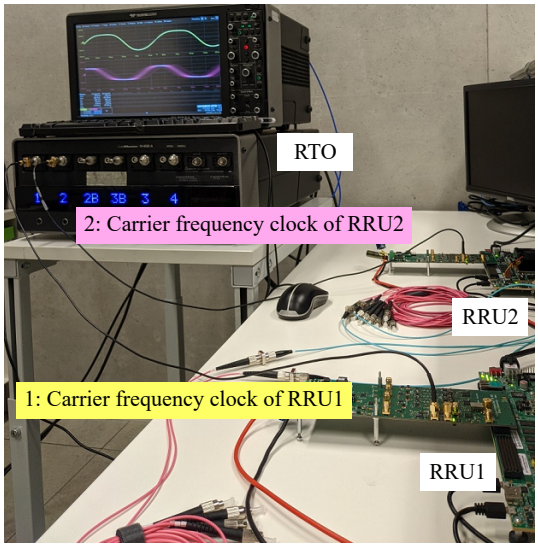

Figure 6.7: Jitter measurement setup. (RTO: real-time oscilloscope.)

6.3.2.1 Jitter Measurement

The DL bitstream contained PRBSs to keep the CDRs on both RRUs locked. The carrier frequency clocks of both RRUs were connected to the real-time oscilloscope (RTO) (*Lecroy LabMaster* 10-65Zi-a). RRU1's clock (labeled in yellow) was the trigger signal. Fig. 6.7 and Fig. 6.8 show the experiment setup and the measured results averaged over 20 seconds (the longest limited average duration of the RTO). Four scenarios were considered.

The stable waveforms imply that the CDRs were frequency-synchronized owing to the synchronization circuits (Fig. 6.5).

The RTO measured the delay between a falling edge of the trigger signal (RRU1's carrier frequency clock) and the first subsequent falling edge of the observed signal (RRU2's carrier frequency clock, labeled in pink) as marked in Fig. 6.8. The mean values of the delay indicated the average phase differences between the two clock sources. The values were different for the four test scenarios because the PLLs had to re-lock each time we changed the fibers. Once the PLLs were locked, these mean values were stable and would be captured as channel information. Hence, while the mean values remain stable, the transceiver coherency is guaranteed.

The standard deviation of the delay can be considered as an indicator of the asynchronous jitter. Fig. 6.8a shows the result when the reference clocks of the first PLLs of both AAUs were connected to the same 30.72 MHz reference

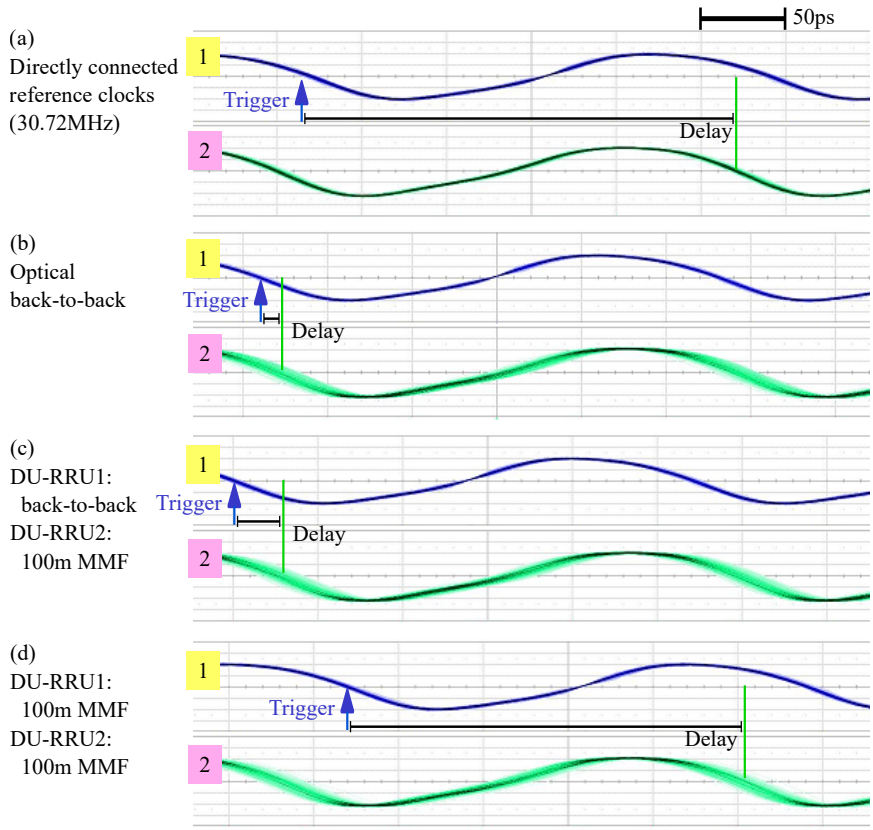

Figure 6.8: Jitter measurement results. The results are shifted horizontally to align the edges of RRU2's clock (labeled in pink) for easy comparison.)

clock instead of the retrieved clocks from the FPGAs. The standard deviation of the delay was 4.02 ps. For the optical back-to-back case (Fig. 6.8b), the standard deviation was 6.95 ps. After a 100 m MMF was added to only the RRU2 DL optical link (Fig. 6.8c), the standard deviation increased slightly to 7.07 ps. When the DL optical links of both RRUs had 100 m MMFs, the standard deviation increased again slightly to 7.16 ps.

6.3.2.2 Spectrum Measurement

To measure the spectrum of the asynchronous phase noise, a 5 MHz sine wave modulated at the carrier frequency (3.6864 GHz), i.e., a 3.6914 GHz sine wave, was connected to one of the RF-in connectors of both RRUs with cables as illustrated in Fig. 6.9.

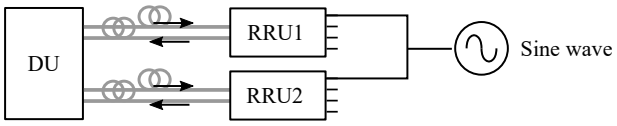

Figure 6.9: Spectrum measurement setup.

The DU provided PRBSs to keep the CDRs at the RRUs locked and received one sine wave from each RRU. The received sine signals were sampled at 81.92 MSps; the received sequences were 25 ms long. A phase shift was applied to one received sine wave and this phase-shifted sine wave was used to cancel the other sine wave. The spectrum of the cancellation result can be viewed as the asynchronous phase noise spectrum.

Fig. 6.10 includes the results of three test scenarios: (a) with directly connected reference clocks for the RRUs, (b) optical back-to-back, and (c) with 100 m DL fibers.

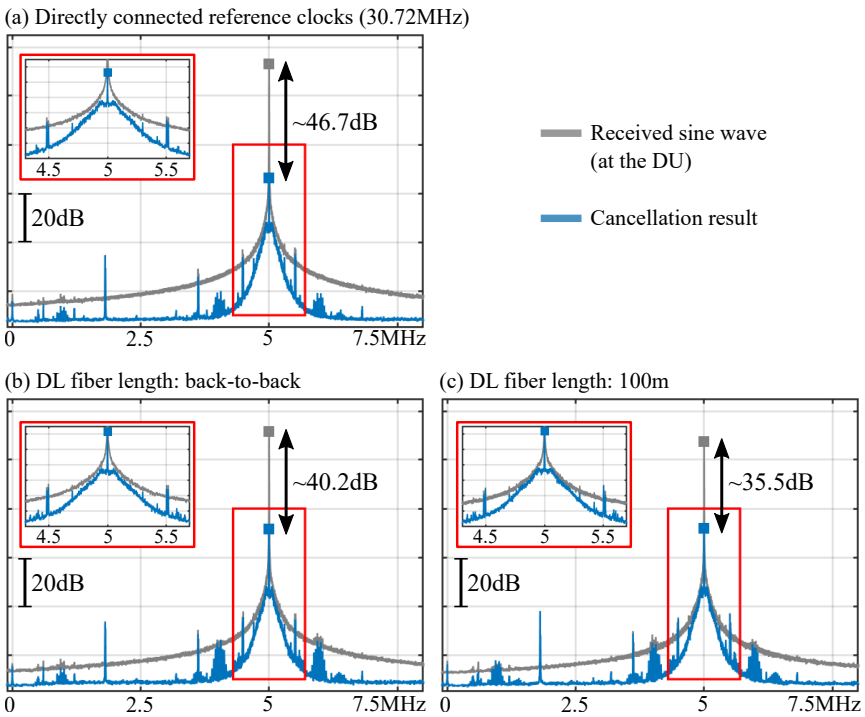

Figure 6.10: Spectra of the received sine wave and the asynchronous phase noise. Measurement time duration: 25ms.

For each scenario, if we compare the two spectra, we can see that the phase noise contained in the two sine waves was mainly correlated. The correlated phase noise originated from the sine wave generator and the retrieved 30.72 MHz clocks, which were extracted from the DL bitstreams generated with one common reference clock at the DU. The spikes at 5 MHz $\pm$ 500 kHz were caused by the power supplies of the AAUs. We also noticed more noise around 5 MHz $\pm$ 1 MHz compared with the old AAUs. However, the source is not clear.

About 46.7 dB suppression was reached if reference clocks were applied. Note that the signal tone was almost 1.5 dB stronger than those of the two other scenarios although the noise floor was almost the same. Scenario (b) and (c) both had better suppression, 40.2 dB and 35.5 dB, respectively, compared to the previously published results [14] (34 dB for both scenarios). One possible explanation is that the suppression performance of the old AAUs was not dominated by the quality of the retrieved clocks.

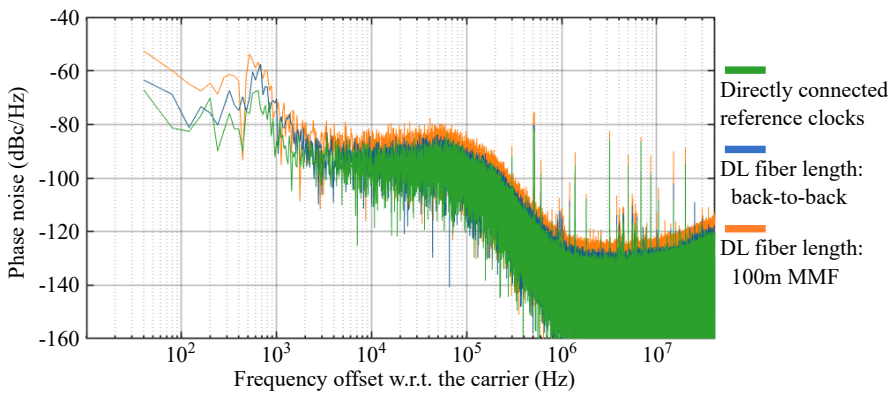

Figure 6.11: Asynchronous phase noise; range: 40 Hz–40.96 MHz.

Fig. 6.11 plots the asynchronous phase noise of the three scenarios. The asynchronous jitter values can be calculated by integrating the phase noise over frequency [15]. The calculated jitter values are 2.50 ps (with directly connected reference clocks), 2.99 ps (with optical back-to-back), and 3.45 ps (with 100 m MMFs). The sine wave data was received by the RRUs and the anti-aliasing filters removed part of the broadband noise. Therefore, the calculated values are smaller than the RTO-measured values (4.02 ps, 6.95 ps, and 7.16 ps), as expected.

6.3.2.3 Phase Difference Measurement

Since distributed antenna systems are one of the targeted use cases for BI-SDoF-based networks, plotting the average phase difference between two RRUs versus time gives an intuitive view of the achievable phase coherence.

As illustrated in Fig. 6.12, one RRU1 transceiver functioned as a transmitter, while another RRU1 transceiver and one RRU2 transceiver received the transmitted signal wirelessly. The two receivers were perfectly synchronized in the carrier and sample clock frequencies. The relation between the sampling timing of the two RRUs was also fixed due to the architecture. Instead of PRBSs, an OFDM signal was sent to RRU1 via the DL fiber.

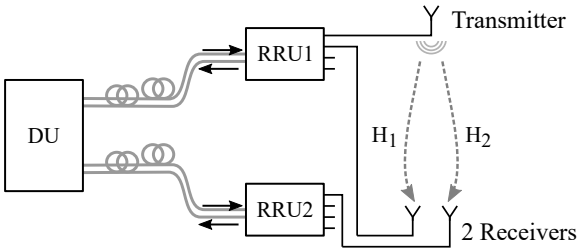

Figure 6.12: Phase difference measurement setup.

The overall CFRs, $\mathbf{H}_1$ and $\mathbf{H}_2$, were estimated using the least square channel estimation [16]. Both estimation results, $\hat{\mathbf{H}}_1$ and $\hat{\mathbf{H}}_2$, contain 114 complex values corresponding to 114 non-zero subcarriers. (See Appendix A.)

During the measurement period, the wireless channels were assumed to remain static. The phase difference between the two RRUs can be calculated by

$$\phi = \frac{1}{N_{\mathbf{D}}} \sum_{k \in \mathbf{D}} \text{angle}\left(\frac{\hat{\mathrm{H}}_{1,k}}{\hat{\mathrm{H}}_{2,k}}\right) \tag{6.1}$$

where k denotes the subcarrier index, $\mathbf{D}$ is the index set of all non-zero subcarriers and $N_{\mathbf{D}}$ is the number of indices in $\mathbf{D}$. $\hat{\mathrm{H}}_{1,k}$ and $\hat{\mathrm{H}}_{2,k}$ denote the k-th elements of $\hat{\mathbf{H}}_1$ and $\hat{\mathbf{H}}_2$, respectively.

Fig. 6.13 plots ϕ versus time for three test scenarios. As in the jitter measurement, the PLLs had to re-lock each time we introduced different fiber lengths, hence the change in the average phase difference. The average was observed to be stable once the PLLs were locked and would be contained in the overall CFRs.

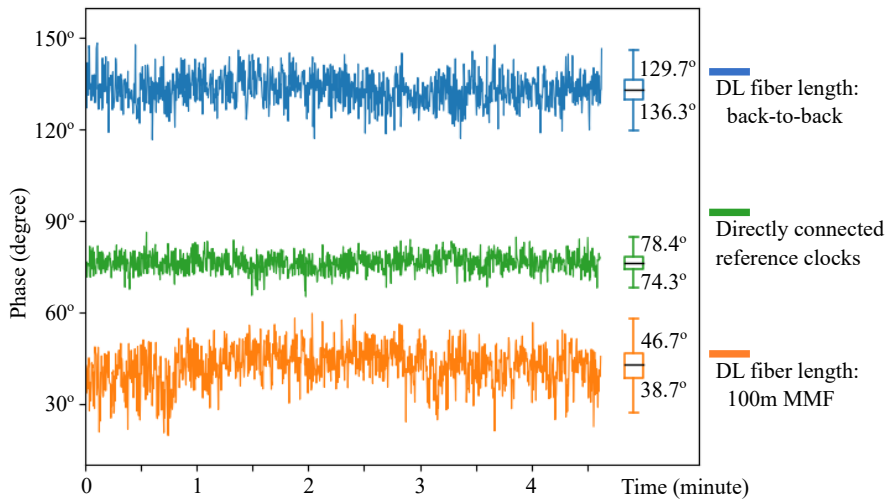

Figure 6.13: RRU phase difference versus time and its distribution.

The box plots[1] of ϕ are included to better visualize the distribution. Table 6.4 summarizes the dispersion measures of the old results, which were measured with the previous-generation AAUs and had been published in [14], together with two sets of results with 1-second, and 5-minute measurement duration, respectively.

Comparing the 0.4-second and 1-second cases, we can see the phase difference between the new AAUs is considerably more stable. It is also noticed that, with the new AAUs, the performance difference between the back-to-back and 100 m DL fiber scenarios becomes more obvious; the standard deviation difference increases from 0.16° [14] to 0.61°. Such results align with the spectrum measurement results. It is possible that, when using the old AAUs, the fluctuation in phase difference was not dominated by the phase noise introduced by extra fibers.

When the measurement duration increased to 5 minutes, all dispersion measures increased accordingly. While the values of the scenario with directly connected reference clocks remained relatively stable, the values of the two other scenarios increased more noticeably.

[1] A box plot shows the spread of numerical data graphically and usually includes a box and a set of whiskers [17]. The box is drawn from the first quartile (Q1)—the median of the lower half of the dataset—to the third quartile (Q3)—the median of the upper half of the dataset—with a horizontal line drawn in the middle to denote the median. The interquartile range (IQR) is defined as Q3−Q1. The upper and lower whiskers denote the largest and smallest observed data point from the dataset that fall within Q3+1.5IQR and Q1−1.5IQR; 1.5 is the default value set by *Matplotlib* of Python [18].

	Standard deviation			**Interquartile range (IQR)**[1]			**Data range excluding outliers**[2]		
Measurement duration	0.4 s[3]	1 s	5 min.	0.4 s[3]	1 s	5 min.	0.4 s[3]	1 s	5 min.
Directly connected ref. clocks	-	2.71	2.94	-	3.70	4.10	-	14.09	16.36
DL fiber length: back-to-back	6.28	4.03	5.09	8.46	5.22	6.67	31.54	20.55	26.29
DL fiber length: 100 m	6.44	4.64	6.34	9.33	6.21	8.05	31.18	23.94	31.09

[1] The interquartile range (IQR) is defined as the range between the first and the third quartile (Q3−Q1), i.e., the range between the medians of the lower and upper halves of the dataset.

[2] The data range excluding outliers is the range between the two whiskers. The upper and lower whiskers denote the largest and smallest observed data point from the dataset that fall within Q3+1.5IQR and Q1−1.5IQR.

[3] These columns contain the results measured with the previous-generation AAUs that have compromised performance due to aging. The results have been published in [14].

Table 6.4: Summary of dispersion measures: measurement duration: 0.4 second [14], 1 second, and 5 minutes. (Unit: degree.)

The fiber length does cause more fluctuation in phase difference. However, within 1 second, the performance difference between the back-to-back and 100 m DL fiber scenarios is less significant.

Distributed schemes can bring rich spatial diversity [19]. However, compared to co-located antenna systems in which little asynchronous phase noise is expected between base station transceivers, the fluctuation in phase difference introduced by separately located frequency synthesizers is unavoidable. Such fluctuation can definitely degrade the digital beamforming accuracy. The impact will be further discussed in Chapter 7.

6.3.3 Single-Input Multiple-Output Uplink Performance

Fig. 6.14 shows a screenshot of the single-input multiple-output (SIMO) uplink demonstration for ECOC 2020 [20]. The setup had a one-antenna user (single-input). At the base station side, there were two RRUs with two active antennas each (multiple-output).

The user transmitted 8 QPSK training frames with known data (for channel estimation) followed by 20 64-QAM data frames. The four antennas at the RRUs received signals at the same time. For the single-input single-output (SISO) case, uplink signals were only received by one antenna (marked with the yellow star). The Python platform estimated the CFRs with the training frames and used the CFRs to compensate for the channel effect when demodulating the data frames. For the SIMO case, the estimated CFRs were used for combining the four received uplink signals from the four antennas with the maximum ratio combining (MRC) method.

Note that it is definitely possible to decrease the number of training frames for channel estimation. Since we did not want the inaccurate channel estimation results to limit the performance, we kept the training sequence long.

In the demonstration, the mobile user moved along the black arrow from the right of the right-most antenna to the left of the left-most antenna. We showed both the SISO and SIMO performance. The upper-right corner plotted the constellation diagram and showed the EVM of the SISO case. The lower-right figure showed the SIMO performance.

When the uplink signal was received by only one base station receiver, the performance degraded as the distance between the user and the receiver increased. The EVM ranged from 3.57% to 13.78%. When the user was served by four base station receivers, the performance remained stably good: 2.28%–4.01%.

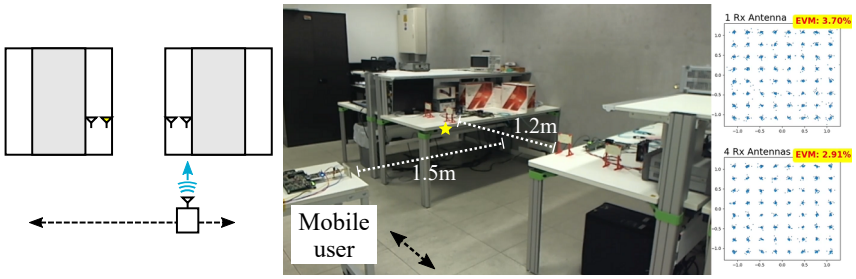

Figure 6.14: Online demonstration at the 46th ECOC.

6.3.4 Multiple-Input Single-Output Downlink Performance

The performance of a four-by-one multiple-input single-output (MISO) downlink setup has also been demonstrated for ECOC 2020 [20]. Due to the progress delay caused by the Covid-19 outbreak, the time-division duplex (TDD) reciprocity calibration process was not implemented in time. The demonstration therefore followed the same workflow as described in Chapter 5.

To guarantee that the estimated downlink channel information could be used by the precoder in time, we eventually used an RRU as the user and connected this "user" to the DU via fiber. As a result, the "user" was frequency-synchronized to the base station. Since the demonstrated performance was less realistic and the digital beamforming performance with the complete calibration process will be introduced in Chapter 7, these results are left out of this dissertation.

6.4 Conclusion

This chapter proposed another feasible distributed antenna system. The system has good signal qualities for both the downlink and uplink data paths. Time-interleaving multiple sigma-delta modulated baseband signals into one bitstream allows for the transmission of NRZ signals over fiber. It also keeps the RRU complexity low while improving the optical bitrate efficiency as explained in Chapter 3.

Additionally, without an extra reference clock signal provided for synchronization, the network guarantees fixed transmission and sampling timing offsets between all transceivers and synchronizes the carrier and sample frequencies between RRUs. The synchronism has been thoroughly validated with measurements in different domains. The real-time oscilloscope observation shows that the two RRUs have the same carrier frequency.

Compared to co-located antenna systems in which little asynchronous phase noise is expected between transceivers, the fluctuation in phase difference can definitely degrade the digital beamforming accuracy. On the other hand, distributed schemes also bring rich spatial diversity.

As cell-free massive MIMO gains more attention, the proposed network architecture has a high potential for its good signal quality, guaranteed synchronism, and scalability.

References

[1] E. G. Larsson *et al.*, "Massive MIMO for Next Generation Wireless Systems," *IEEE Communications Magazine*, vol. 52, no. 2, pp. 186–195, 2014.

[2] S. Ahmadi, *5G NR*, Chapter 4: New Radio Access Physical Layer Aspects (Part 2), First ed. London, United Kingdom: Academic Press, Elsevier, 2019.

[3] I. F. Akyildiz *et al.*, "6G and Beyond: The Future of Wireless Communications Systems," *IEEE Access*, vol. 8, pp. 133 995–134 030, 2020.

[4] N. Rajatheva *et al.*, "White Paper on Broadband Connectivity in 6G," 2020, last accessed on Jul. 6, 2022. Available on URL: https://arxiv.org/pdf/2004.14247.pdf

[5] The 5G Infrastructure Public Private Partnership (5G PPP), "European Vision for the 6G Network Ecosystem," 2021, last accessed on Jul. 6, 2022. Available on URL: https://5g-ppp.eu/wp-content/uploads/2021/06/WhitePaper-6G-Europe.pdf

[6] C.-M. Chen *et al.*, "Scaling Up Distributed Massive MIMO: Why and How," in *Proc. 2017 51st Asilomar Conference on Signals, Systems, and Computers*, 2017, pp. 271–276.

[7] J. Zhang *et al.*, "Cell-Free Massive MIMO: A New Next-Generation Paradigm," *IEEE Access*, vol. 7, pp. 99 878–99 888, 2019.

[8] O. Caytan *et al.*, "Passive Opto-Antenna as Downlink Remote Antenna Unit for Radio Frequency over Fiber," *Journal of Lightwave Technology*, vol. 36, no. 19, pp. 4445–4459, 2018.

[9] J. Li *et al.*, "Impacts of Asynchronous Reception on Cell-Free Distributed Massive MIMO Systems," *IEEE Transactions on Vehicular Technology*, vol. 70, no. 10, pp. 11 106–11 110, 2021.

[10] "3GPP TS 38.104. New Radio (NR): Base Station (BS) Radio Transmission and Reception (Release 17) (V17.6.0)," June 2022.

[11] A. N. Mody and G. L. Stuber, "Synchronization for MIMO OFDM Systems," in *Proc. 2001 IEEE Global Communications Conference (GLOBECOM '01)*, vol. 1, 2001, pp. 509–513.

[12] J. Wang *et al.*, "Delta-Sigma Digitization and Optical Coherent Transmission of DOCSIS 3.1 Signals in Hybrid Fiber Coax Networks," *Journal of Lightwave Technology*, vol. 36, no. 2, pp. 568–579, 2018.

[13] I. C. Sezgin *et al.*, "Effect of VCSEL Characteristics on Ultra-High Speed Sigma-Delta-over-Fiber Communication Links," *Journal of Lightwave Technology*, vol. 37, no. 9, pp. 2109–2119, 2019.

[14] C.-Y. Wu *et al.*, "A Bit-Interleaved Sigma-Delta-over-Fiber Fronthaul Network for Frequency-Synchronous Distributed Antenna Systems," *Applied Sciences*, no. 23, 2021.

[15] W. Kester, "Converting Oscillator Phase Noise to Time Jitter (MT-008 Tutorial)," last accessed on Jul. 6, 2022. Available on URL: https://www.analog.com/media/en/training-seminars/tutorials/mt-008.pdf

[16] J.-J. van de Beek *et al.*, "On Channel Estimation in OFDM Systems," in *Proc. 1995 IEEE 45th Vehicular Technology Conference. Countdown to the Wireless Twenty-First Century*, vol. 2, 1995, pp. 815–819.

[17] "Box plot (Wikipedia)," last accessed on Jul. 6, 2022. Available on URL: https://en.wikipedia.org/wiki/Box_plot

[18] "Matplotlib 3.5.1 documentation: matplotlib.pyplot.boxplot," last accessed on Jul. 6, 2022. Available on URL: https://matplotlib.org/stable/api/_as_gen/matplotlib.pyplot.boxplot.html

[19] I. C. Sezgin *et al.*, "A Low-Complexity Distributed-MIMO Testbed Based on High-Speed Sigma-Delta-over-Fiber," *IEEE Transactions on Microwave Theory and Techniques*, vol. 67, no. 7, pp. 2861–2872, 2019.

[20] C.-Y. Wu *et al.*, "Demonstration of a Scalable Distributed Antenna System Using Real-Time Bit-Interleaved Sigma-Delta-over-Fiber Architectures," in *Proc. 46th European Conference on Optical Communication (ECOC 2020)*, 2020, pp. 1–4.

Part III

Impacts of Asynchronous Phase Noise on Distributed Antenna Systems

7

Impacts of Asynchronous Phase Noise on Distributed Antenna Systems

7.1 Introduction

Except for the distributed antenna systems (DASs) enabled by radio-frequency signal over fiber (RFoF) technologies, other DASs cannot avoid all asynchronism between remote radio units (RRUs), namely frequency-, time-, and phase-asynchronism.

The radio-frequency (RF) carriers and the sample clocks of analog-to-digital / digital-to-analog converters (ADCs / DACs) can be synchronized by providing the frequency synthesizers at RRUs with additional low-frequency clocks [1, 2] or CDR-retrieved clocks [3, 4]. (CDR: clock-and-data recovery module.)

Commonly used protocols have well-defined requirements for time-synchronization [5, 6]. For analog radio-over-fiber (ARoF) or sigma-delta-over-fiber (SDoF), the straightforward architectures guarantee the coherency of transmission and reception timings. Due to hardware mismatches, the signals may not be transmitted or received by all RRUs at the exact same moment; however, the timing offsets should be time-invariant and can be calibrated.

Most distributed schemes have frequency synthesizers located at RRUs. The frequency synthesizers generate clocks with the same frequency and dif-

ferent (initial) phases. Inevitably, jitter / phase noise[1] is introduced into the system by the generated clocks. If the frequency synthesizers are configured properly and provide stable clocks, the initial phases can either be calibrated or compensated by equalizers. However, little can be done about the phase noise. Besides, the phase noise introduced by the independent frequency synthesizers is independent, thus asynchronous.

For multiple-antenna transmission, estimated channel state information (CSI) is often used to generate precoding matrices. Because the impact of phase noise would also be contained in the estimated CSI [7], the phase noise will result in phase inaccuracy of the CSI. Therefore, it would influence the precoding accuracy. The impact of asynchronous phase noise on DASs has been mentioned briefly in Chapters 5 and 6. In Chapter 5, noticeable beamforming performance degradation due to asynchronous phase noise was observed. Chapter 6 showed the fluctuation in the phase difference between two RRUs, which was expected to degrade the digital beamforming accuracy.

In Section 7.2, the expected performance degradation of a 2-by-1 digital beamforming case, caused by beamforming phase inaccuracy, is derived. Then, Section 7.3 focuses on the impact of asynchronous phase noise on the time-division duplex (TDD) reciprocity calibration. The calibration is an essential process for massive MIMO systems to calculate the downlink channel information based on the uplink channel information. This section also analyzes the characteristics of the calibration coefficients. To demonstrate the impact, Section 7.4 provides simulation and measurement results using the setup introduced in Chapter 6.

7.2 Impact of Inaccurate Digital Beamforming Phases

The derivation is based on a two-antenna system transmitting orthogonal frequency-division multiplexing (OFDM) signals. The system has two transmitters and one receiver.

For subcarrier k, the frequency-domain expression of the single-antenna transmission from transmitter i (Txi) to the receiver can be written:

$$\mathrm{R}_{i,k} = \mathrm{H}_{i,k} \cdot e^{j\theta_i} \cdot \mathrm{X}_{i,k} + \mathrm{W}_{i,k} \tag{7.1}$$

where $\mathrm{R}, \mathrm{H}, \mathrm{X}$, and W denote the received constellation, the channel frequency response (CFR), the transmitted data, and the additive white Gaussian noise

[1] Jitter and phase noise are two terms to describe the same imperfection. The term "phase noise" is used in this chapter.

(AWGN). To simplify the derivation, the phase deviation (θ) caused by phase noise, is assumed to remain stable within an OFDM frame; hence, the value is the same for all subcarriers.

To perform beamforming, the workflow described in Chapter 5 is applied. During the training phase, the overall CFRs are estimated. Ideally, if the signal-to-noise ratio (SNR) is sufficiently high, the estimated CFR $\hat{\mathrm{H}}_{i,k}$ for subcarrier k is:

$$\hat{\mathrm{H}}_{i,k} \approx \mathrm{H}_{i,k} \cdot e^{j\theta_i} \,. \tag{7.2}$$

To guarantee that the signals from both transmitters add up constructively at the receiver, the data to be transmitted (S_k) is precoded by multiplying the precoding matrices[2]:

$$\mathbf{M}_k = \begin{bmatrix} \hat{\mathrm{H}}^*_{1,k} \\ \hat{\mathrm{H}}^*_{2,k} \end{bmatrix} \,; \tag{7.3}$$

$\hat{\mathrm{H}}^*_{i,k}$ is the complex conjugate of $\hat{\mathrm{H}}_{i,k}$.

The matrix form of the transmission can be written as:

$$\mathrm{R}_k = \begin{bmatrix} \mathrm{H}_{1,k} \cdot e^{j\theta'_1} & \mathrm{H}_{2,k} \cdot e^{j\theta'_2} \end{bmatrix} \underbrace{\begin{bmatrix} \hat{\mathrm{H}}^*_{1,k} \\ \hat{\mathrm{H}}^*_{2,k} \end{bmatrix} \mathrm{S}_k}_{\text{Precoded data}} + \begin{bmatrix} \mathrm{W}_{1,k} \\ \mathrm{W}_{2,k} \end{bmatrix} \,. \tag{7.4}$$

To focus on the impact of phase noise, the following assumptions are made:

1. The SNR is sufficiently high, so W is negligible.
2. The CFRs remain stable between the training phase and the data transmission.
3. The absolute values of all $\mathrm{H}_{i,k}$ equal to 1.

With these assumptions, Eq. (7.4) can be rewritten as:

$$\mathrm{R}_k = \left(e^{j(\theta'_1 - \theta_1)} + e^{j(\theta'_2 - \theta_2)} \right) \mathrm{S}_k \,. \tag{7.5}$$

When the two transmitters share the same clock source, the phase deviation will be the same for both transmitters, i.e. $\theta'_1 - \theta_1 = \theta'_2 - \theta_2$.

$$\mathrm{R}_k = 2 \cdot e^{j\Delta\theta} \cdot \mathrm{S}_k \tag{7.6}$$

where $\Delta\theta = \theta'_1 - \theta_1 = \theta'_2 - \theta_2$. This phase deviation can be easily compensated by the receiver equalizer.

[2]This precoding method is called maximum ratio transmission (MRT).

Unfortunately, if the two transmitters are located at two RRUs, they will not share the same clock source. The phase drifts will not be the same for both transmitters. The two parts of Eq. (7.5) will have different values, instead of aligning perfectly in phase at the receiver.

$$\mathrm{R}_k = \left(e^{j\Delta\theta_1} + e^{j\Delta\theta_2}\right)\mathrm{S}_k = \left(1 + e^{j(\Delta\theta_2 - \Delta\theta_1)}\right) \cdot e^{j\Delta\theta_1}\mathrm{S}_k\,. \tag{7.7}$$

The term $e^{j\Delta\theta_1}$ can be compensated by the receiver equalizer.

By comparing Eq. (7.6) and Eq. (7.7), the degradation in the received signal power is:

$$P_{\text{degradation}}(\text{dB}) = 10\text{log}\left|\frac{2}{1+e^{j\phi}}\right|^2 = 10\text{log}\left(\frac{2}{1+cos(\phi)}\right) \tag{7.8}$$

with ϕ denotes the asynchronous phase noise corresponding to $\Delta\theta_2 - \Delta\theta_1$. The signal power degradation would also be the SNR degradation if the noise power is the same.

If the asynchronous phase noise is modeled as a Gaussian random variable with zero mean and σ_ϕ^2 variance: $\mathcal{N}(0, \sigma_\phi^2)$, the expected power degradation (in dB) with respect to σ_ϕ^2 is:

$$\mathrm{E}\left[P_{\text{degradation}}\right] = 10\text{log}\left(\frac{2}{1+e^{-\frac{1}{2}\sigma_\phi^2}}\right)\,. \tag{7.9}$$

The derivation is included in Appendix C.

Fig. 7.1 plots the signal degradation due to the inaccurate phase versus σ_ϕ in degree. The larger the phase noise variance, the less likely that the signals from multiple transmitters will be aligned. Thus, the SNR degradation increases.

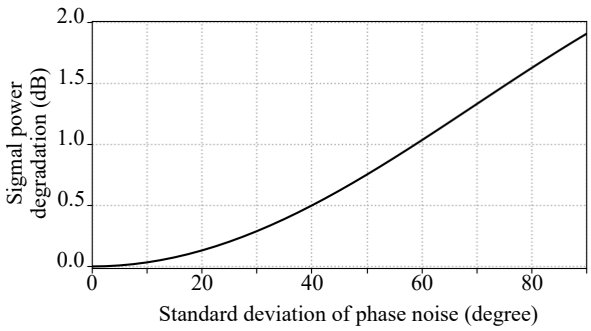

Figure 7.1: The signal power degradation (dB) versus the stadard deviation of ϕ (degree).

7.3 DAS Exploiting Time-Division Duplex (TDD) Reciprocity

For single-user beamforming, inaccurate CSI results in gain loss. For multi-user MIMO (MU-MIMO), to properly serve the spatially multiplexed users, CSI at the transmitter side is essential to most multi-user precoding techniques [8, 9]. On the transmitter side, the CSI can be used to mitigate the interference between users; this is common for downlink (DL) transmission.

In most systems, especially those with wide bandwidths, the CSI feedback is a heavy burden on the uplink (UL) capacity [8]. For massive MIMO, the required time-frequency resources to estimate CSI at the user side and the feedback overhead become impractical [10].

Operating in TDD mode is therefore preferred for the possibility to exploit the reciprocity of the wireless DL and UL channels [10, 11]. In the TDD scenario, while operating in the same frequency band, wireless channels can be assumed to remain constant in the time slot divided between the reverse link (uplink) and the forward link (downlink). When estimating CSI, all base station antennas can receive the signal from a user simultaneously. Hence, the required time-frequency resources for CSI estimation grow proportionally to the number of users N_{U} instead of the number of base station transceivers N_{B}; N_{B} is usually larger than N_{U} for massive MIMO systems. Furthermore, users are no longer required to send CSI to the base station.

However, communication channels do not consist of only wireless channels. The DL and UL hardware chains are seldom reciprocal and the differences must be calibrated [10, 12].

7.3.1 Exact versus Relative TDD Reciprocity Calibration

A communication channel consists of the wireless propagation channel, which is typically reciprocal for both the DL and UL, and the hardware at both sides of the link, including antennas, amplifiers, filters, etc. Since the DL and UL signals pass through different devices, the non-reciprocity of the hardware paths is self-explanatory. The TDD reciprocity calibration process, abbreviated as calibration process in this chapter, estimates calibration coefficients, which indicate the relation between the DL and UL channels.

When transmitting an OFDM signal, the overall DL and UL CFRs for subcarrier k can be written as:

$$\mathrm{H}_{\mathrm{B}\to\mathrm{U},k} = \mathrm{T}_{\mathrm{B},k} \cdot \mathrm{H}_k \cdot \mathrm{R}_{\mathrm{U},k} \cdot e^{-j2\pi\Delta f t_{\mathrm{D}}} \cdot e^{-j\Delta\theta(t_{\mathrm{D}})} \tag{7.10}$$

and

$$\mathrm{H}_{\mathrm{U}\to\mathrm{B},k} = \mathrm{T}_{\mathrm{U},k} \cdot \mathrm{H}_k \cdot \mathrm{R}_{\mathrm{B},k} \cdot e^{j2\pi\Delta f t_{\mathrm{U}}} \cdot e^{j\Delta\theta(t_{\mathrm{U}})} \tag{7.11}$$

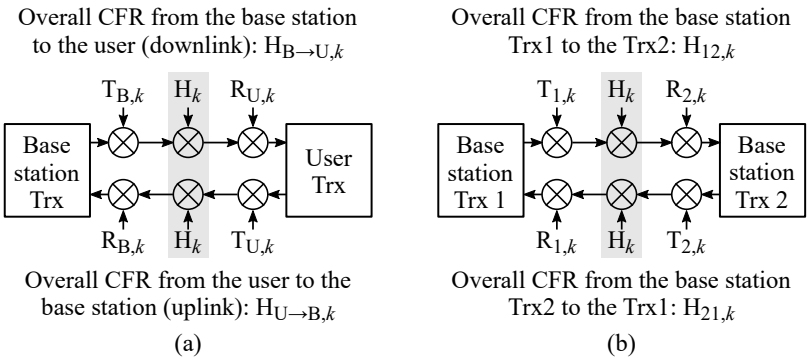

Figure 7.2: The overall channels between (a) a base station transceiver and a user; (b) two base station transceivers. The impacts of carrier frequency offsets and phase deviation are not marked in the figure. (CFR: channel frequency response; Trx: transceiver; k is the subcarrier index.)

where T, H, and, R denote the CFRs of the transmission (hardware), wireless, and reception (hardware) paths as illustrated in Fig. 7.2a; the subscripts B and U represent "base station transceiver" and "user transceiver", respectively; t_{D} and t_{U} are the timestamps when the DL and UL CFRs are measured; Δf denotes the carrier frequency offset (CFO) between the base station carrier f_{B} and the user carrier f_{U}; $\Delta\theta(t)$ comprises the constant phase difference between the base station and the user oscillators and the phase noise. If both carrier clocks are stable, only the phase noise changes over time.

The original (exact) calibration process involves both the base station and the served users [12]. The exact calibration coefficients are:

$$c_k = \frac{\mathrm{H}_{\mathrm{B}\to\mathrm{U},k}}{\mathrm{H}_{\mathrm{U}\to\mathrm{B},k}} = \frac{\mathrm{T}_{\mathrm{B},k}\cdot\mathrm{R}_{\mathrm{U},k}}{\mathrm{T}_{\mathrm{U},k}\cdot\mathrm{R}_{\mathrm{B},k}}\cdot e^{-j2\pi\Delta f(t_{\mathrm{D}}+t_{\mathrm{U}})}\cdot e^{-j(\Delta\theta(t_{\mathrm{D}})+\Delta\theta(t_{\mathrm{U}}))}\,. \quad (7.12)$$

The DL CFRs can be calculated using the estimated calibration coefficients $\hat{c}_k$ and the estimated UL CFRs $\hat{\mathrm{H}}_{\mathrm{U}\to\mathrm{B},k}$:

$$\mathrm{H}_{\mathrm{B}\to\mathrm{U},k} = \hat{c}_k\cdot\hat{\mathrm{H}}_{\mathrm{U}\to\mathrm{B},k}\,. \quad (7.13)$$

The calculated CFRs can be used for precoding.

The t_{D}-related terms in Eq. (7.12) can be troublesome. The DL-UL relation is likely to be different when the coefficients are applied. However, if all base station transceivers are synchronized in frequency and phase, the impact of the t_{D}-related terms will be the same for all transceivers. Therefore, the impact can be ignored when applying linear precoding.

Many later publications show that the relative calibration coefficients with respect to a reference transceiver are sufficient for linear MU-MIMO precoding techniques [13–15][3]. For co-located antenna systems, the transceivers are usually synchronized in time, frequency, and even phase. The relative calibration coefficient for subcarrier k between base station transceiver i and j is

$$c_{ij,k} = \frac{\mathrm{H}_{i\to j,k}}{\mathrm{H}_{j\to i,k}} = \frac{\mathrm{T}_{i,k} \cdot \mathrm{R}_{j,k}}{\mathrm{T}_{j,k} \cdot \mathrm{R}_{i,k}}. \tag{7.14}$$

The calibration coefficients can be estimated involving only base stations. Furthermore, the calibration coefficients are time-invariant.

7.3.2 Challenges for Distributed Antenna Systems (DASs)

For DASs, each RRU has its own oscillator or frequency synthesizer. It is again important to consider the impact of: (1) the CFOs between the RRUs, and (2) the phase differences between multiple oscillators.

Transceivers i and j are located at different RRUs. Both transceivers lock to a stable carrier frequency (f_i and f_j). Similar to Eq. (7.10) and Eq. (7.11), the overall CFR from transceiver i to j can be written as

$$\mathrm{H}_{i\to j,k} = \mathrm{T}_{i,k} \cdot \mathrm{H}_k \cdot \mathrm{R}_{j,k} \cdot e^{-j2\pi\Delta f t} \cdot e^{-j\Delta\theta(t)} \tag{7.15}$$

and the overall CFR from j to i can be written as

$$\mathrm{H}_{j\to i,k} = \mathrm{T}_{j,k} \cdot \mathrm{H}_k \cdot \mathrm{R}_{i,k} \cdot e^{j2\pi\Delta f t} \cdot e^{j\Delta\theta(t)} \tag{7.16}$$

where t is the time when the H is measured; $\Delta f = f_i - f_j$; $\Delta\theta(t)$ comprises the constant phase difference between two oscillators and asynchronous phase noise, which changes over time. Eq. (7.14) becomes

$$c_{ij,k} = \underbrace{\frac{\mathrm{T}_{i,k} \cdot \mathrm{R}_{j,k}}{\mathrm{T}_{j,k} \cdot \mathrm{R}_{i,k}}}_{\text{Time-invariant}} \cdot \underbrace{e^{-j2\pi\Delta f(t_{ij}+t_{ji})} \cdot e^{-j(\Delta\theta(t_{ij})+\Delta\theta(t_{ji}))}}_{\text{Time-variant}} \tag{7.17}$$

where t_{ij} and t_{ji} are the timestamps when $\mathrm{H}_{i\to j,k}$ and $\mathrm{H}_{j\to i,k}$ are measured, respectively. The calibration coefficients indicate the DL-UL relation of the

[3] [15] concludes from mathematical derivations that it is only necessary to calibrate the phase non-reciprocity at the base station side, i.e. the argument of $\mathrm{T}_{\mathrm{B},k}/\mathrm{R}_{\mathrm{B},k}$ (in the polar form). The rest has no impact on the inter-user interference (IUI) when applying linear precoding techniques. [16] claims differently: it is necessary to calibrate also the amplitude non-reciprocity, i.e. the absolute value of c_k (in the polar form). The main reason is that [16] aims to maximize the channel capacity and the power distribution for each user is important.

moment when they are calculated. The DL-UL relation is time-variant, so it is likely to be different when the coefficients are applied. Unlike the co-located scheme, Δf and $\Delta\theta(t)$ can be different between all transceivers. The impact of the time-variant part cannot be ignored for linear precoding and makes the use of channel reciprocity in DASs challenging. Such inaccuracy can accordingly degrade the performance [17].

As demonstrated in the previous chapter, the RRUs of our system are frequency-synchronized. The transmission and reception timing relations between RRUs are constant. However, phase fluctuation has been observed.

7.3.3 Workflow

Fig. 7.3 illustrates the workflow of a 2-by-1 DAS. The general workflow consists of three phases:

1. Calibration phase: to estimate the calibration coefficients.
   To estimate $\mathbf{H}_{\mathrm{R1}}$ and $\mathbf{H}_{\mathrm{R2}}$, the two transceivers transmit frequency-interleaved OFDM sequences[4] to a reference antenna. Then, to estimate $\mathbf{H}_{\mathrm{1R}}$ and $\mathbf{H}_{\mathrm{2R}}$, the reference antenna transmits when both transceivers receive simultaneously.

2. Training phase: to estimate the CFRs using the known data sent by users.
   The calculated DL CFRs relative to the reference antenna are:

$$\hat{\mathrm{H}}_{\mathrm{DL1},k} = \hat{c}_{\mathrm{1R},k} \cdot \hat{\mathrm{H}}_{\mathrm{UL1},k} \tag{7.18}$$

   and

$$\hat{\mathrm{H}}_{\mathrm{DL2},k} = \hat{c}_{\mathrm{2R},k} \cdot \hat{\mathrm{H}}_{\mathrm{UL2},k}\,, \tag{7.19}$$

   respectively.

3. Data transmission phase: to transmit the DL data to users.
   The DL data is precoded using Eq. (7.3).

The bold $\mathbf{H}$ denotes the vector formed by the CFRs of all subcarriers; the CFR corresponding to subcarrier k (H_k) is the k-th element of $\mathbf{H}$.

The calibration coefficients, estimated during one calibration phase, will be used to calculate the DL CFRs from the UL CFRs for precoding for several subsequent data transmission phases. The estimated UL CFRs, estimated during one training phase, will be used only by the data transmission phase following it. Frequent calibration and channel estimation are heavy overheads. Ideally, (1) the time-variant part of the calibration coefficients should not change

[4] See Appendix A

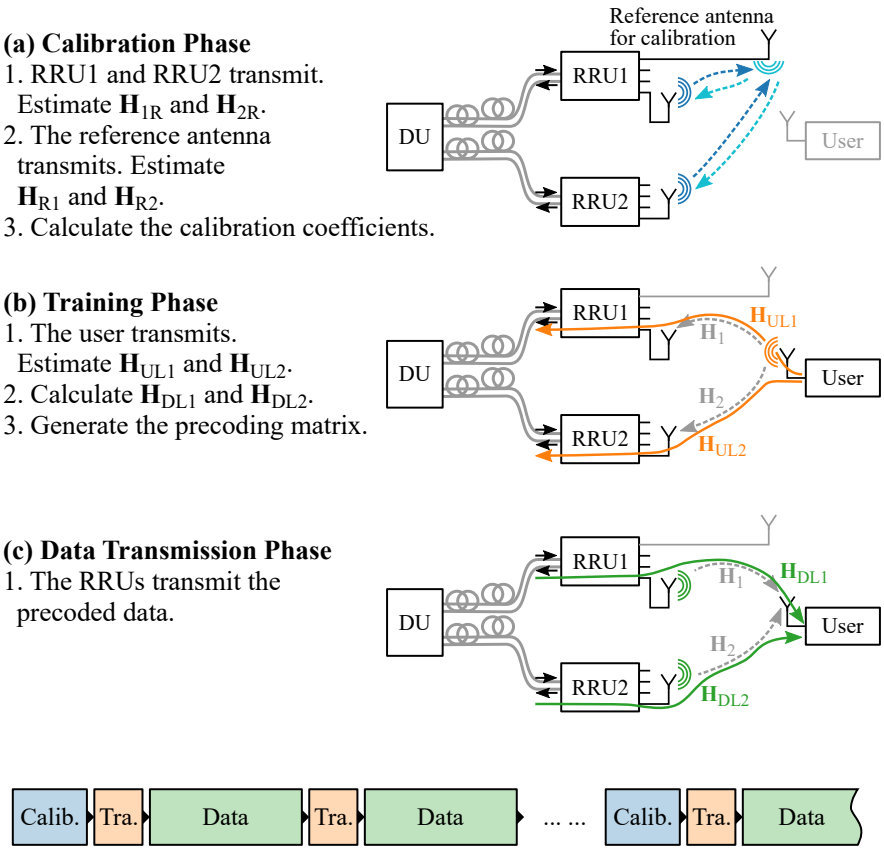

Figure 7.3: Workflow with time-division duplex (TDD) reciprocity calibration.

too much between two calibration phases and (2) the wireless channel should be static between two training phases.

The stability of the calibration coefficients corresponds to the asynchronous phase noise between RRU 1 and RRU 2 as explained below. It can be derived from Eq. (7.17) that

$$\hat{c}_{21,k} = \frac{\hat{c}_{2\mathrm{R},k}}{\hat{c}_{1\mathrm{R},k}} \,. \tag{7.20}$$

The precoding matrix, defined by Eq. (7.3), can be written as:

$$\mathbf{M}_k = \begin{bmatrix} \hat{c}_{1\mathrm{R},k} \cdot \hat{\mathrm{H}}_{\mathrm{UL1},k} \\ \hat{c}_{2\mathrm{R},k} \cdot \hat{\mathrm{H}}_{\mathrm{UL2},k} \end{bmatrix} = \hat{c}_{1\mathrm{R},k} \begin{bmatrix} \hat{\mathrm{H}}_{\mathrm{UL1},k} \\ \hat{c}_{21,k} \cdot \hat{\mathrm{H}}_{\mathrm{UL2},k} \end{bmatrix} \,. \tag{7.21}$$

The only relevent part for the beamforming accuracy is the time-variant part of $\hat{c}_{21,k}$. If the RRUs are frequency-synchronized, the time-variant part of $\hat{c}_{21,k}$ corresponds to the phase deviation between two RRUs—the asynchronous phase noise.

The time interval between two training phases, i.e. the length of the data transmission phase, depends on the coherence time of the wireless channel.

7.4 Experimental Methodology and Results

In this section, the experimental results were measured with the setup introduced in Chapter 6 [4]. First of all, the calibration coefficient stability is evaluated by measuring $\hat{c}_{21,k}$. Then, a few examples are provided to show the impact of inaccurate precoding. In Subsection 7.4.3, the error vector magnitude (EVM) values were measured for 10 minutes after one calibration phase to evaluate the necessity of frequent calibration for this setup.

7.4.1 Calibration Coefficient Stability

The measurement results for two schemes and three scenarios are provided. In the co-located scheme, all transceivers were located at one RRU; in the distributed scheme, the reference antenna and transceiver 1 were located at RRU 1 and transceiver 2 was located at RRU 2. For both schemes, the antenna locations were fixed. Hence, the performance differences between the two schemes were not related to the wireless channels. The reference antenna was placed across the two transceivers to guarantee line-of-sight (LoS) paths.

The three scenarios differed in the quality of the reference clocks for the frequency synthesizers. In the first scenario, a 30.72 MHz reference clock was connected to the frequency synthesizers. In the second and third scenarios, the reference clocks were retrieved from the DL bitstreams by CDRs; the optical links were 8 m (back-to-back) and 100 m multi-mode fibers.

Each set of sub-figures in Fig. 7.4 corresponds to one scenario of one scheme. The two sub-figures in each set show the amplitudes and phases of 1000 sets of $\hat{c}_{21,k}$ measured over five minutes; the x-axis is the subcarrier index (k). The black lines show the medians of all measurements. All measurement results are combined into the blue shadows.

For the co-located scheme, the blue shadows are barely visible. The quality of the reference clocks had little impact on the stability of $\hat{c}_{21,k}$. For the distributed scheme, the amplitudes are rather stable. The slopes of the phases are also stable; the blue shadows consist of sets of parallel lines. As the reference clock quality drops, the shadow width, corresponding to the phase deviation, increases.

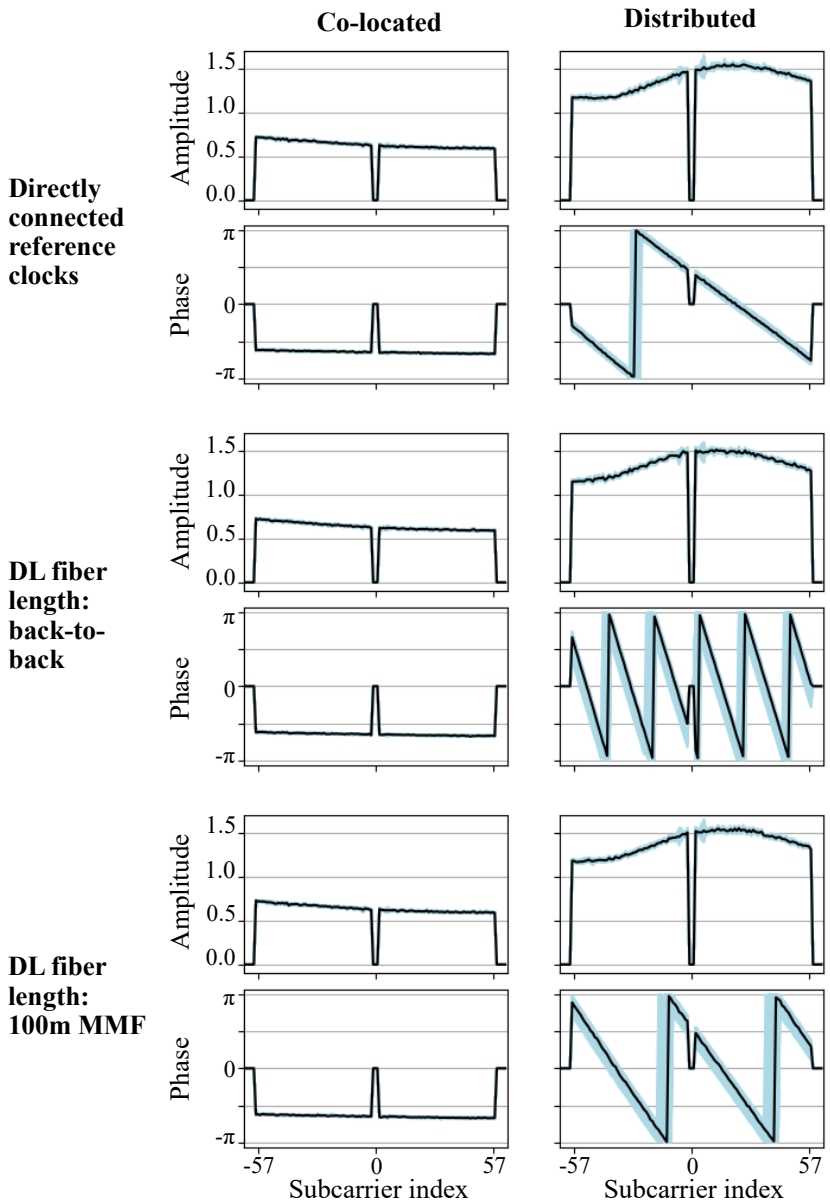

Figure 7.4: Calibration coefficients.

Three parts of $\hat{c}_{21,k}$ can be analyzed separately: the amplitudes $A_k(t)$, the slope of the phase $t_d(t)$, and the phase offset $\phi(t)$[5].

$$\hat{c}_{21,k} = A_k(t) \cdot e^{j\,2\pi\,t_d(t)\,f_{\text{sub}}\,k} \cdot e^{j\phi(t)} \tag{7.22}$$

where f_{sub} is the subcarrier spacing; for our setup, the subcarrier spacing is 320 kHz.

The amplitudes correspond to the gain differences between two transceivers. The values relate only to the hardware paths. As long as the same set of transceivers is used, A_k is time-invariant.

The slopes correspond to the combined delay differences in both the wireless and hardware paths between two transceivers. In an indoor environment, the path delay difference should be very small. Every meter of (physical) distance difference between the two transceivers and the reference transceiver results in around 3.3 ns (1 m / (3 $\times$ 10^8 m/s)) of difference in the arrival time.

For the co-located scheme, all three scenarios have slopes close to zero, as observed from the left column of Fig. 7.4. If the t_d values are plotted versus time, the figure will show three lines overlapping each other.

However, due to the distributed scheme, the buffer registers and the first-in first-out (FIFO) memory queues on the RRU FPGAs can introduce larger timing offsets. These hardware modules are used often in the design to convert data from one clock domain to another, e.g. from the ADC sample clock at 92.16 MHz to the FPGA clock around 200 MHz. These offsets are related to the initialization relation between multiple clocks on the FPGAs. The stability of the slopes is more obvious in Fig. 7.5, in which the t_d values of the distributed cases are plotted versus time. For the three plotted scenarios, the FPGAs were re-started. Therefore, the t_d values are different.

The phase offset can be further separated into two parts:

$$\phi(t) = \overline{\phi} + \phi_{\text{PN}}(t) \tag{7.23}$$

where $\overline{\phi}$ is the average phase difference between two transceivers and $\phi_{\text{PN}}(t)$ denotes the time-variant asynchronous phase noise. The average phase difference, same as discussed in Subsection 6.3.2 (6.3.2.1 and 6.3.2.3), will be compensated later by the receiver channel estimation.

For the co-located scheme (Fig. 7.6a), the three scenarios had the same $\overline{\phi}$ around 116°. The two transceivers shared the same clock sources for the radio-frequency carrier and the ADC sample clock. $\overline{\phi}$ came from the hardware, e.g. different paths for the clock signals. Thus, there was barely any phase fluctuation between transceivers. The standard deviations of ϕ_{PN} are 0.43°,

[5] If digital infinite impulse response (IIR) filters are applied in the system, it is more accurate to describe the phase offset as a function of both the timestamp (t) and the subcarrier index (k).

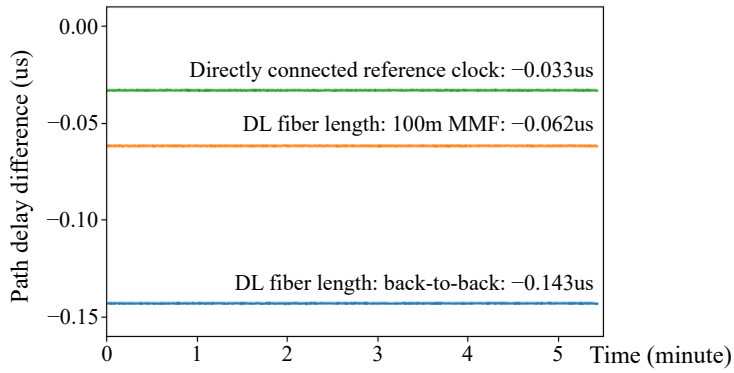

Figure 7.5: Path delay differences (t_d) versus time for the distributed cases.

0.50°, and 0.55° for the cases with directly connected reference clocks, with optical back-to-back, and with 100 MMFs.

For the distributed scheme (Fig. 7.6b), the three scenarios had different $\overline{\phi}$. $\overline{\phi}$ came from both the hardware and the average phase difference between separately located oscillators. Same as explained in Subsection 6.2.3, the mean values are different because the PLLs had to re-lock for each scenario. Once the PLLs were locked, $\overline{\phi}$ remained stable. The dispersion measures[6] are listed in Table 7.1.

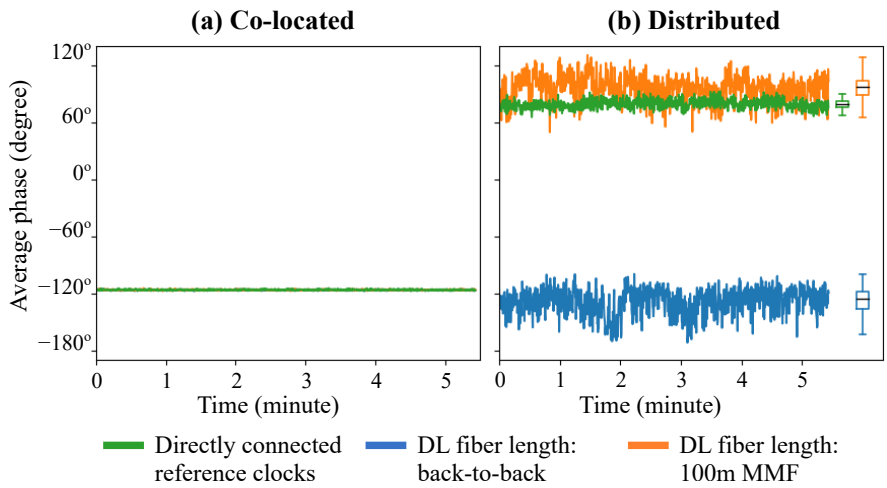

Figure 7.6: Phase offsets (ϕ) versus time for the (a) co-located and (b) distributed cases.

	Standard deviation	Interquartile range (IQR)	Data range excl. outliers
Direct ref. clocks	4.53	6.03	22.50
Optical B2B	13.97	18.74	63.80
100 MMFs	13.28	15.98	63.16

Table 7.1: Dispersion measures[6] of Fig. 7.6b. (Unit: degree.)

To conclude, the hardware-introduced factors are stable once the system is stable after starting up. Asynchronous phase noise between RRUs is the main cause of fluctuation.

7.4.2 Precoding Accuracy

To calculate the precoding matrices with Eq. (7.21), the calibration coefficients and the estimated UL CFRs are combined. Both accuracies are important to guarantee that the signals from the two transmitters add up constructively at the user. In this subsection, the necessity of TDD reciprocity calibration is demonstrated by both simulation and measurement results. Following the conclusion of [15], only the impact of phase inaccuracy is considered, i.e. the influences of t_d and $\phi(t)$.

If the calibration process is skipped, the signals from the two transceivers would arrive at the user with a phase difference. The phase difference, calculated from Eq. (7.22) and Eq. (7.23), can be written as:

$$\varphi(t) = \underbrace{\overline{\phi} + \phi_{\text{PN}}(t)}_{\phi(t)} + \underbrace{2\pi\, t_d\, f_{\text{sub}}\, k}_{k\text{-related}} \,. \tag{7.24}$$

The first part is not related to the subcarrier index k. The impact of $\phi_{\text{PN}}(t)$ has been discussed in Subsection 7.2. $\overline{\phi}$ makes the two signals arrive with a phase difference. Fig. 7.7 shows a simple simulation result: Two signals are generated by adding one 40.96 MHz-bandwidth OFDM signal with two different sets of AWGN. The signals are combined with a phase difference (x-axis) and the EVM of the combined signal is plotted.

[6] A box plot shows the spread of numerical data graphically and usually includes a box and a set of whiskers [18]. The box is drawn from the first quartile (Q1)—the median of the lower half of the dataset—to the third quartile (Q3)—the median of the upper half of the dataset—with a horizontal line drawn in the middle to denote the median. The interquartile range (IQR) is defined as Q3−Q1. The upper and lower whiskers denote the largest and smallest observed data point from the dataset that fall within Q3+1.5IQR and Q1−1.5IQR; 1.5 is the default value set by *Matplotlib* of Python [19].

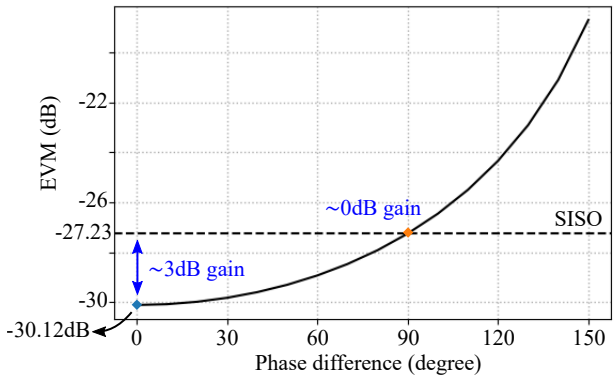

Figure 7.7: Inaccurate precoding: the impact of $\overline{\phi}$.

Each signal (before the combination) has an EVM of around 4.3% (-27 dB). If the phase difference ($\overline{\phi}$) is zero, the two signals will combine constructively and provide about 3 dB gain. However, as $\overline{\phi}$ becomes larger, the gain decreases. When $\overline{\phi}$ is larger than 90°, the gain even becomes negative.

Fig. 7.8 plots the spectra of the combined signals and the EVM values of each subcarrier for $\overline{\phi}$ equals 0° and 90°. The gain difference is obvious from both the spectra and the EVM values. When the two signals combine at the user with a 90° phase difference, the signal power is lower. There is no gain in the signal power, so the EVM values remain similar to those of only one transmitter, i.e. the single-input single-output (SISO) case.

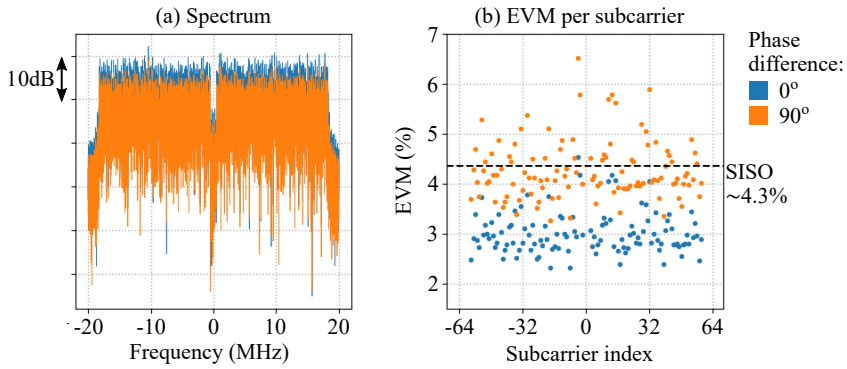

Figure 7.8: Inaccurate precoding: the impact of $\overline{\phi}$.

The second part of $\varphi(t)$ in Eq. (7.24) is caused by the path delay difference and, therefore, related to the subcarrier index. As stated in the previous subsec-

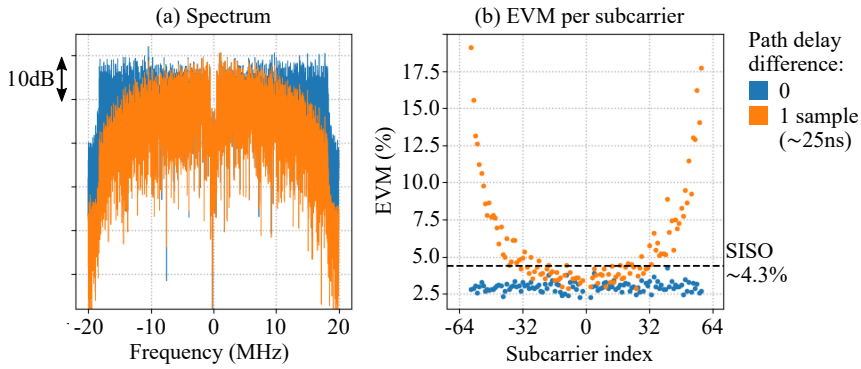

Figure 7.9: Inaccurate precoding: the impact of t_d.

tion, the path delay difference should be very small in an indoor environment. However, when calculating the DL CFRs from the UL ones, the receive chain hardware can introduce larger delay differences. The path delay results in different arrival phases for different subcarriers. The signals on some subcarriers combine constructively, while others combine destructively.

Fig. 7.9 plots the spectra of the combined signals and the EVM values of each subcarrier for t_d equals 0 ns and 25 ns (1 OFDM sample at 40.96MSps). If only $2\pi\, t_d\, f_{\text{sub}}\, k$ is considered, the phase difference grows proportionally with $|k|$. The subcarriers further away from the center combine destructively and result in poor signal qualities.

In a real system, the impacts of all parts in Eq. (7.24) are usually combined. Fig. 7.10 and Fig. 7.11 shows the measurement results using the DAS introduced in Chapter 6. The 2-by-1 beamforming was performed without the calibration process. The estimated UL CFRs were used directly as DL CFRs.

In Fig. 7.10, signals on all subcarriers combined destructively. In Fig. 7.11, the k-related phase deviation is obvious. Some subcarriers have low EVMs less than 4%; some are totally ruined.

To accurately estimate t_d, the DAS must be able to transmit and receive the signal coherently. Our proposed system is therefore a viable solution. The straightforward transmission and reception paths guarantee the coherency. The negative impact of asynchronous reception has also been evaluated in [20].

When the complete process, illustrated in Fig. 7.3, was followed and the precoding matrices were generated using Eq. (7.21), an average EVM of 2.66% was achieved as plotted in Fig. 7.12. The importance of the calibration process is incontrovertible.

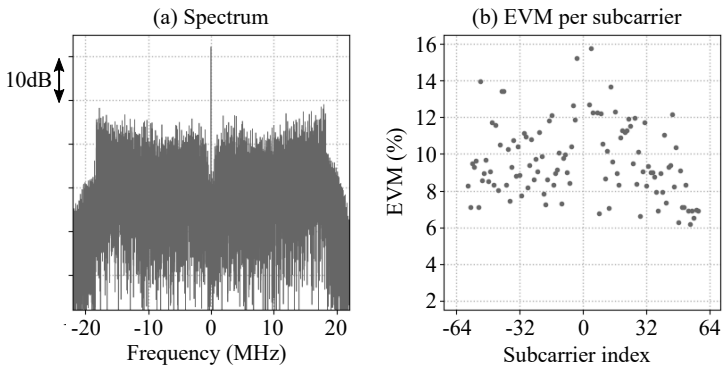

Figure 7.10: Digital beamforming **without** the calibration process.

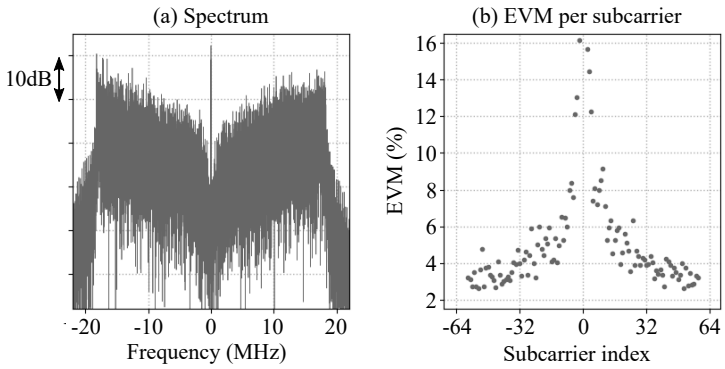

Figure 7.11: Digital beamforming **without** the calibration process.

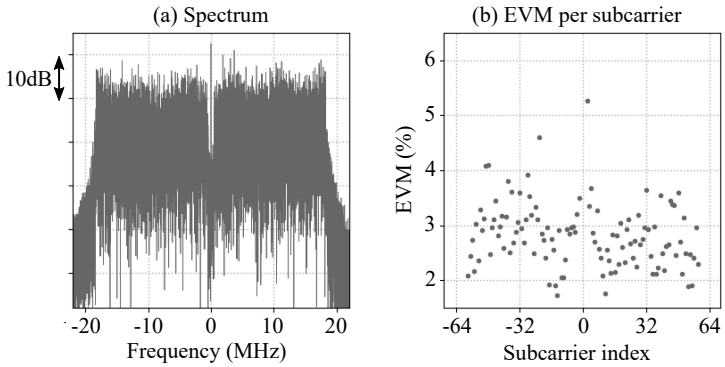

Figure 7.12: Digital beamforming with the calibration process.

7.4.3 DAS Performance Stability

The importance of calibration has been demonstrated. The next question is: how often should the calibration process be performed? Since the calibration coefficients from all transceivers are required, frequent calibration is a heavy overhead.

According to the results shown in Subsection 7.4.1, the only time-variant part is the asynchronous phase noise—$\phi_{\mathrm{PN}}(t)$ in Eq. (7.24). It can be observed from Fig. 7.6 that the averages were stable although the phases fluctuated. Similar fluctuation is also expected in the beamforming accuracy. However, the beamforming performance should not become worse over time.

The experiment started with one calibration phase. Then, the training and data transmission phases were repeated for ten minutes. Fig. 7.13 shows the experimental results.

The EVM of the SISO link (downlink) between either transmitter and the user was around 3.23% (-29.81 dB). There was no shared clock between the transceivers and the user; the CFO was canceled by the algorithm proposed in [21]. When performing the 2-by-1 beamforming, 3 dB attenuators were added to both transceivers; the total transmit power remained the same as the SISO case. Therefore, the ideal gain brought by the spatial diversity should be 3 dB if the EVM is noise-limited.

For the case with directly connected reference clocks, the average EVM was 2.70% (-31.38 dB), corresponding to a gain of 1.57 dB compared to the SISO case. The best EVM was 2.32% (-32.69 dB), corresponding to a gain of 2.88 dB. The first quartile (Q1) was 2.59% (-31.73 dB), meaning that 25% of the measured EVM values correspond to more than 1.92 dB gain. The EVM variation may come mainly from the UL CFR quality.

For the optical back-to-back case, the average EVM was 2.97% (-30.55 dB), corresponding to only 0.74 dB gain. The best EVM was 2.58% (-31.77 dB), corresponding to a gain of 1.96 dB. The first quartile (Q1) was 2.84% (-30.93 dB); 25% of the measured EVM values correspond to more than 1.12 dB gain.

For both scenarios, the EVM values remained stable. This meets the observation of the phase fluctuation (Fig. 7.6). However, this conclusion differs from the experimental results published in [1]. The performance of the distributed massive MIMO system in [1] degraded over time. One possible reason is that the settings of the frequency synthesizers might cause small frequency drifts; the frequency drifts make the phases drift further over time. Besides, the performance with more transceivers and users needs more investigation.

The gain loss between the two scenarios was about 0.7 dB.

Using Eq. (7.9) and the measured variances in Table 7.1, the expected loss in signal power can be calculated. Since the calibration process happened

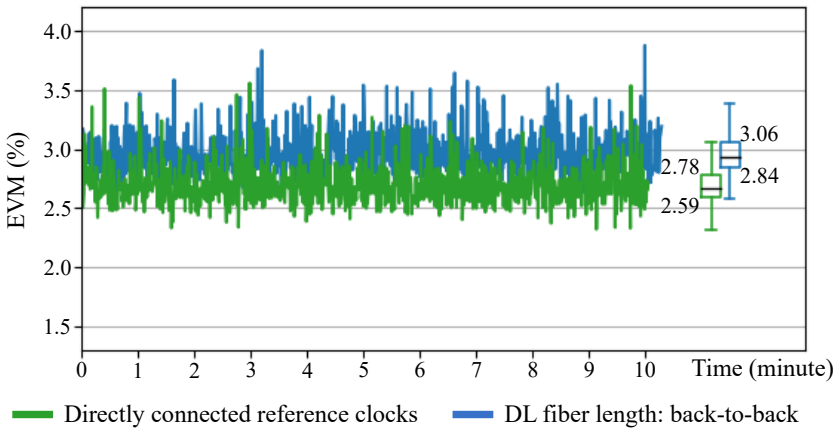

Figure 7.13: EVM values versus time after a calibration phase.

only once at the beginning of each experiment, the phase of the calibration coefficients and the actual required phase when the precoding matrices were calculated can be considered independent. The phase difference of the two transmitted signals at the user, if considered as a random variable, will have a variance that is the sum of the variances of the two abovementioned phases.

Therefore, the signal power loss for the scenario with directly connected reference clocks is 0.013 dB (calculated with σ_ϕ^2=0.0125). For optical back-to-back, the loss is 0.127 dB (calculated with σ_ϕ^2=0.1189). The calculated difference is much smaller than 0.7 dB. Since the two scenarios differed only in the reference clock provision, it is suspected that the extra phase noise introduced by the optical links had other impacts. For example, with directly connected reference clocks, the EVM of the received UL signal was about 0.4 dB better than the optical back-to-back case; this may have some influences on the estimation accuracy of the UL CFRs. However, this can only be confirmed if better CDRs are available.

The Necessity of Re-Calibration

Based on all the collected experimental results, the hardware-dependent parts in the calibration coefficients are almost static over time. The gains and path delays may change slightly and slowly with temperature. They can be calibrated hourly or less frequent.

The time-variant part should be calibrated more often because differences between several sets of results collected throughout the same day have been observed. If the frequency synthesizers work properly, frequent calibration is

unnecessary as demonstrated with our setup. One calibration phase every ten minutes seems sufficient. Since the time-variant phase differences only exist between RRUs, it is only necessary to re-calibrate the phase of one antenna for each RRU. The required calibration time and computation power can be largely decreased.

7.5 Conclusion

This chapter starts with the impact of phase inaccuracy on the performance of digital beamforming. Then, it focuses on the time-division duplex (TDD) reciprocity calibration process and the challenges of performing such calibration in a distributed antenna system. The calibration coefficients are analyzed based on the sources, e.g. the transceiver gain and delay path differences. More importantly, simulation and experimental results are provided to demonstrate the importance of TDD reciprocity calibration and the necessity of frequent re-calibration.

To conclude, TDD reciprocity calibration is indispensable if one wants to use estimated uplink channel frequency responses for precoding. To mitigate the overhead of the calibration process, the time-invariant and time-variant parts of the calibration coefficients can be separated and have different re-calibration cycles. If the frequency synchronization circuits work properly, even the time-variant parts do not need frequent calibration. However, this also implies that frequent calibration is unlikely to improve the performance; high-quality clock-and-data recovery modules (CDRs) and frequency synthesizers are important.

References

[1] C.-M. Chen *et al.*, "Distributed Massive MIMO: A Diversity Combining Method for TDD Reciprocity Calibration," in *Proc. 2017 IEEE Global Communications Conference (GLOBECOM)*, 2017, pp. 1–7.

[2] M. Sung *et al.*, "5G Trial Services Demonstration: IFoF-Based Distributed Antenna System in 28 GHz Millimeter-Wave Supporting Gigabit Mobile Services," *Journal of Lightwave Technology*, vol. 37, no. 14, pp. 3592–3601, 2019.

[3] C.-Y. Wu *et al.*, "Distributed Antenna System Using Sigma-Delta Intermediate-Frequency-over-Fiber for Frequency Bands above 24 GHz," *Journal of Lightwave Technology*, vol. 38, no. 10, pp. 2765–2773, 2020.

[4] ——, "A Bit-Interleaved Sigma-Delta-over-Fiber Fronthaul Network for Frequency-Synchronous Distributed Antenna Systems," *Applied Sciences*, no. 23, 2021.

[5] "Common Public Radio Interface (CPRI) Specification V7.0," 2015, last accessed on Jul. 6, 2022. Available on URL: http://www.cpri.info/spec.html

[6] "IEEE Standard for Local and Metropolitan Area Networks–Time-Sensitive Networking for Fronthaul," 2018, last accessed on Jul. 6, 2022. Available on URL: https://ieeexplore.ieee.org/document/8376066

[7] S. Wu and Y. Y. Bar-Ness, "A Phase Noise Suppression Algorithm for OFDM-Based WLANs," *IEEE Communications Letters*, vol. 6, no. 12, pp. 535–537, 2002.

[8] D. Gesbert *et al.*, "Shifting the MIMO Paradigm," *IEEE Signal Processing Magazine*, vol. 24, no. 5, pp. 36–46, 2007.

[9] D. Nojima *et al.*, "Performance Evaluation for Multi-User MIMO IEEE 802.11ac Wireless LAN System," in *Proc. 2012 14th International Conference on Advanced Communication Technology (ICACT)*, 2012, pp. 804–808.

[10] E. G. Larsson *et al.*, "Massive MIMO for Next Generation Wireless Systems," *IEEE Communications Magazine*, vol. 52, no. 2, pp. 186–195, 2014.

[11] T. L. Marzetta, "Noncooperative Cellular Wireless with Unlimited Numbers of Base Station Antennas," *IEEE Transactions on Wireless Communications*, vol. 9, no. 11, pp. 3590–3600, 2010.

[12] A. Bourdoux *et al.*, "Non-Reciprocal Transceivers in OFDM/SDMA Systems: Impact and Mitigation," in *Proc. 2003 Radio and Wireless Conference (RAWCON '03)*, 2003, pp. 183–186.

[13] C. Shepard *et al.*, "Argos: Practical Many-Antenna Base Stations," in *Proc. 18th Annual International Conference on Mobile Computing and Networking (Mobicom '12)*, 2012, pp. 53–64.

[14] F. Kaltenberger *et al.*, "Relative Channel Reciprocity Calibration in MIMO/TDD Systems," in *Proc. 2010 Future Network Mobile Summit*, 2010, pp. 1–10.

[15] J. Morte Palacios *et al.*, "Impact of Channel Non-Reciprocity in Cell-Free Massive MIMO," *IEEE Wireless Communications Letters*, vol. 9, no. 3, pp. 344–348, 2020.

[16] B. M. Lee, "Calibration for Channel Reciprocity in Industrial Massive MIMO Antenna Systems," *IEEE Transactions on Industrial Informatics*, vol. 14, no. 1, pp. 221–230, 2018.

[17] R. Chopra *et al.*, "Blind Channel Estimation for Downlink Massive MIMO Systems with Imperfect Channel Reciprocity," *IEEE Transactions on Signal Processing*, vol. 68, pp. 3132–3145, 2020.

[18] "Box plot (Wikipedia)," last accessed on Jul. 6, 2022. Available on URL: https://en.wikipedia.org/wiki/Box_plot

[19] "Matplotlib 3.5.1 documentation: matplotlib.pyplot.boxplot," last accessed on Jul. 6, 2022. Available on URL: https://matplotlib.org/stable/api/_as_gen/matplotlib.pyplot.boxplot.html

[20] J. Li *et al.*, "Impacts of Asynchronous Reception on Cell-Free Distributed Massive MIMO Systems," *IEEE Transactions on Vehicular Technology*, vol. 70, no. 10, pp. 11 106–11 110, 2021.

[21] A. N. Mody and G. L. Stuber, "Synchronization for MIMO OFDM Systems," in *Proc. 2001 IEEE Global Communications Conference (GLOBECOM '01)*, vol. 1, 2001, pp. 509–513.

8
Conclusions

8.1 Summary of the Results

The main focus of this dissertation is the combination of sigma-delta-over-fiber (SDoF) technologies and distributed antenna systems (DASs). Multiple solutions for radio-over-fiber (RoF) based radio access networks (RANs) have been proposed. This work demonstrated the performance of three DASs targetting different applications. Most importantly, the experimental results highlighted the importance of synchronization between remote radio units (RRUs).

The first part of the dissertation briefly introduced the RAN evolution and compared several RoF technologies. Although digitized RoF (DRoF) links continue to be deployed for 5G next-generation RANs (NG-RANs), SDoF technologies can be a potential key enabler for distributed / cell-free massive MIMO for 6G. SDoF technologies are appealing for their relaxed requirements on device linearities, high tolerance on the optical bit-error rate (BER), and the possibility of having simple RRUs. They provide more space for the trade-offs between optical bitrate efficiency and RRU complexities. When combined with DASs, they have some additional advantages: The SDoF-based networks are more centralized and make the coordination between RRUs easier. With clock-and-data recovery modules (CDRs), the frequency of multiple RRUs can be easily synchronized without extra reference clocks. Furthermore, the straightforward architectures guarantee time coherence.

In the second part, three DASs enabled by SDoF links were decribed. All DASs have frequency-synchronous RRUs.

Chapter 4 demonstrated a two-antenna DAS for the 3.5 GHz bands. The architecture is extremely centralized. By up-converting the downlink signals to the radio frequency at a central site, the RRUs are perfectly synchronized in (transmission) time, frequency, and phase. Compared with the single-input single-output (SISO) cases, the 2×2 multi-user multiple-input multiple-output (MIMO) cases had little performance degradation, implying that the wireless capacity was doubled. Therefore, the architecture is suitable to increase the channel capacity for hot-spot scenarios. Moreover, the centralized architecture makes the RRUs extremely simple and power-efficient. The perfect synchronism and the simple RRU architecture also make it a good candidate for localization applications.

Chapter 5 modified the distributed antenna system of Chapter 4 to allow for applications in the 28 GHz bands. For this architecture, sigma-delta modulated baseband signals are up-converted to an intermediate frequency (2.5 GHz) and transmitted over fiber. At each RRU, the clock information contained in the downlink non-return-to-zero (NRZ) bitstream is retrieved using a CDR. The frequency synchronism between RRUs is guaranteed with no extra reference clock signal provided. The more complicated RRUs bring two main benefits: improved optical bitrate efficiency and carrier-frequency flexibility. According to the experimental results, the two antennas provided an antenna gain and the distributed scheme improved the coverage. However, the separately located up-converters (to the millimeter-wave (mmWave) radio frequency) introduced asynchronous phase noise. The loss in the beamforming performance, due to the asynchronous phase noise, ranged from 0.35 dB to 0.83 dB. The system was also not possible to perform multi-user MIMO (MU-MIMO) transmission.

In Chapter 6, we focused on the scalability with respect to both the number of RRUs and the number of transceivers per RRU. The sigma-delta modulated baseband signals are time-interleaved, so each fiber can provide signals to more antennas or receive signals from more antennas. The architecture is therefore more scalable toward cell-free massive MIMO. To synchronize the frequencies of RRUs, this architecture also uses CDRs and requires no extra reference clock signal. With experimental results, the good signal qualities for both the downlink and uplink have been demonstrated.

The third part focused on the impact of asynchronism. Few distributed antenna systems can avoid all asynchronism—in frequency, time, and phase—between RRUs. Using 2×1 digital beamforming transmission as an example, the chapter began with the derivation of the expected performance degrada-

tion caused by inaccurate beamforming phases. Through simulation and experimental results, the importance of time-division duplex (TDD) reciprocity calibration and the impacts of time and phase asynchronism have been demonstrated.

The experimental results also show that the setup proposed in Chapter 6 does not require frequent TDD reciprocity calibration; the calibration frequency can be lower than once every ten minutes. Such stability makes it a viable candidate for cell-free massive MIMO networks. However, an unignorable performance loss has been observed between the more ideal and the more realistic synchronization schemes: with the CDR-retrieved clocks, the performance was much worse than that with directly connected reference clocks. Although the frequencies were stable and synchronized for both cases, the CDR-retrieved clocks introduced more phase noise into the system. To further evaluate the impact of phase asynchronism on MU-MIMO systems, a simplified derivation was provided based on the 2×2 MU-MIMO setup introduced in Chapter 4. The negative influence of asynchronous phase noise between RRUs showed more obviously on the performance of interference cancellation.

Chapter 7 showed both the feasibility and challenges if one wishes to exploit TDD reciprocity for distributed MIMO systems. It can be concluded that stricter phase noise requirements are necessary.

8.2 Future Work

Fig. 8.1 illustrates the topics which have been explored in this dissertation and the potential future work. An mmWave distributed MIMO system (the upper-right corner of Fig. 8.1) can be built based on the mmWave DAS proposed in Chapter 5. The concepts of intermediate-frequency signal over fiber (IFoF) and bit-interleaved sigma-delta-over-fiber (BI-SDoF) can be combined to further improve optical bitrate efficiency. The BI-SDoF-enabled DAS (Chapter 6) is currently being tested with more transceivers to form a cell-free massive MIMO system (the lower-left corner of Fig. 8.1). We also believe that high-quality CDRs can suppress the phase asynchronism between RRUs and further improve performance.

The last missing part of the puzzle—which was not covered by this work—is cell-free massive MIMO for mmWave applications [1]. The distributed scheme is expected to largely improve the coverage and capacity by combating the high path loss and lack of multi-paths for mmWave bands [2].

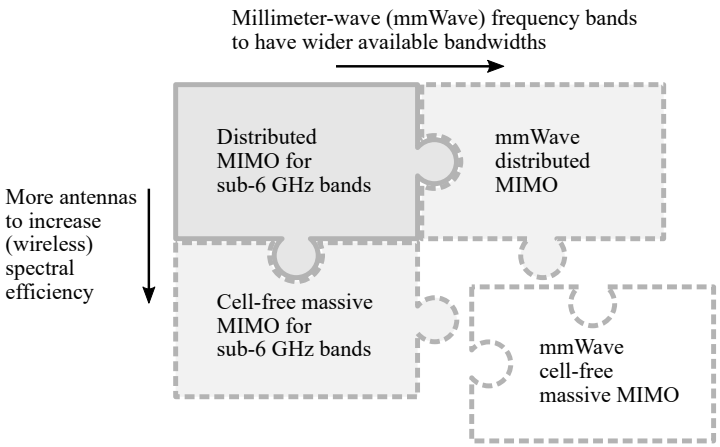

Figure 8.1: From distributed MIMO to cell-free massive MIMO and from sub-6 GHz bands to millimeter wave bands.

Deploying the optical networks to serve cell-free massive MIMO systems can be pricy. The concept of sequential fronthaul networks can avoid too much fiber installation [3]. However, we have demonstrated the importance of stable transmission and reception timings; the impact of the extra latency due to the sequential architecture is worth investigating.

References

[1] E. Björnson, L. Van der Perre, S. Buzzi, and E. G. Larsson, "Massive MIMO in Sub-6 GHz and mmWave: Physical, Practical, and Use-Case Differences," *IEEE Wireless Communications*, vol. 26, no. 2, pp. 100–108, 2019.

[2] S. Sun *et al.*, "MIMO for Millimeter-Wave Wireless Communications: Beamforming, Spatial Multiplexing, or Both?" *IEEE Communications Magazine*, vol. 52, no. 12, pp. 110–121, 2014.

[3] G. Interdonato, E. Björnson, H. Q. Ngo, P. Frenger, and E. Larsson, "Ubiquitous Cell-Free Massive MIMO Communications," *EURASIP Journal on Wireless Communications and Networking*, 2019.

Appendix

A
OFDM Signals

Self-defined orthogonal frequency-division multiplexing (OFDM) [1] baseband signals were used for all experiments mentioned in this dissertation for the ease of implementation and the possibility to experiment with physical (PHY) layer signal processing. The OFDM signals were either generated by MATLAB (for Chapters 4 and 5) or Python (for Chapter 6 and Part III).

A.1 Signal Parameters

Based on the a priori knowledge that the experiments would be carried out in indoor environments, the OFDM signal parameters were modified from the IEEE 802.11ac specification [2]. Table A.1 lists the related parameters.

To match the available analog-to-digital converter (ADC) and digital-to-analog converter (DAC) sample rates of the analog front-end evaluation kits (*Analog Device* FMCOMMS1-EBZ), the OFDM signals were generated with a subcarrier spacing (f_{sub}) of 320 kHz such that the OFDM bandwidths including the null band-edge subcarriers ($f_{\text{sub}} \times N_{\text{FFT}}$) equal simple fractions of 122.88 MHz.

The maximum signal bandwidth defined in the IEEE 802.11ac specification is 160 MHz, which is divided into 512 subcarriers; $N_{\text{FFT}} = 512$. For the frequency bands above 24 GHz, wide-bandwidth signals were generated. The signal bandwidths were limited by the supported sample rate of the ADCs used by the user / receiver in Chapter 5—*Analog Devices* AD9643 [3]. AD9643

Parameters	**Values**					
Cyclic prefix	1/4 (0.78 µs)					
Subcarrier spacing	320 kHz					
Bandwidth (MHz)	20.48	40.96	81.92	163.84	249.92	299.20
N_{FFT}[1]	64	128	256	512	1024	1024
N_{DC}[2]+ N_{Null}[2]	8	14	14	28	254	100
N_{Pilot}[2]	4	6	8	16	26	32
Data rate per user						
64-QAM (Mbps)	79.87	165.89	359.42	718.85	1142.78	1370.11
256-QAM (Mbps)	106.50	221.18	479.23	958.46	1523.71[3]	1826.82[3]

[1] N_{FFT}: number of subcarriers (FFT / IFFT size).
[2] N_{DC}, N_{Null}, and N_{Pilot}: number of DC, null, and pilot subcarriers.
[3] These values are listed to complete the table. However, no 256-QAM signal with a bandwidth larger than 163.84 MHz was tested.

Table A.1: OFDM signal parameters

claims sample rates of up to 250 MSps (megasamples per second). According to the datasheet, one can sample frequencies from DC to 300 MHz using appropriate filtering at the ADC inputs with little loss in the performance. The 249.92 MHz- and 299.20 MHz-bandwidth signals were generated by nulling the high-index subcarriers of the 1024-point inverse fast Fourier transform (IFFT). When the user received those signals, the ADC sample rate was 327.68 MSps. Both 249.92 MHz and 299.20 MHz are the bandwidths occupied by data subcarriers. Therefore, Chapter 5 uses the bandwidths occupied by data subcarriers (160.32 MHz, 249.92 MHz, and 299.20 MHz) for consistancy, instead of the full bandwidths including the null band-edge subcarriers ($f_{\text{sub}} \times N_{\text{FFT}}$), e.g. 163.84 MHz and 327.68 MHz.

A.2 Frequency-Interleaved OFDM Signals

Frequency-interleaved training sequences, illustrated in Figure A.1, were used for downlink (DL) channel estimation for the experiments in Chapters 4 and 5 and the time-division duplex (TDD) reciprocity calibration in Chapter 7.

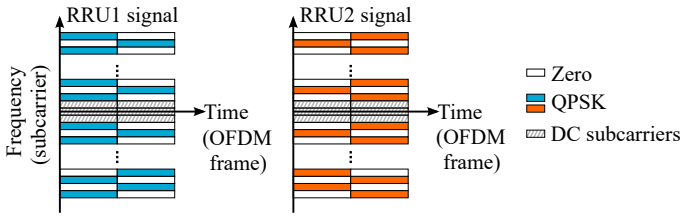

Figure A.1: Frequency-interleaved training sequence.

Without loss of generality, the scenario with two remote radio units (RRUs) is used as an example. For each subcarrier, within one given OFDM frame, either the first RRU (RRU1) or second RRU (RRU2) transmits QPSK data while the other one transmits nothing. To estimate the channel frequency responses (CFRs) of all subcarriers, the training sequences should last at least N OFDM frames for the case with N transmitters; N is an integer. In a noisy environment, using longer training sequences, i.e. averaging over multiple estimated CFRs, results in better channel estimation results.

References

[1] M. I. Rahman and S. Das, "OFDM Based WLAN Systems," 2004, last accessed on Jul. 6, 2022. Available on URL: https://www.semanticscholar.org/paper/OFDM-Based-WLAN-Systems-Rahman-Das/b494f23540390a608fd1e63e10ed0a024fcfd1d0

[2] "IEEE Standard for Information Technology–Telecommunications and Information Exchange between Systems Local and Metropolitan Area Networks—Specific Requirements–Part 11: Wireless LAN Medium Access Control (MAC) and Physical Layer (PHY) Specifications–Amendment 4: Enhancements for Very High Throughput for Operation in Bands below 6 GHz," 2013, last accessed on Jul. 6, 2022. Available on URL: https://ieeexplore.ieee.org/document/6687187

[3] *Analog Device*, "AD9643 Datasheet and Product Info," last accessed on Jul. 6, 2022. Available on URL: https://www.analog.com/en/products/ad9643.html

B

Error Vector Magnitude (EVM)

Error vector magnitude (EVM) values are commonly used as the signal quality metric. To compare the results with related publications, we measured the EVM values before the symbol detection (Fig. B.1), i.e. the QAM demodulation, as the reference point for EVM measurement mentioned in

"3GPP TS 38.104. New Radio (NR): Base Station (BS) Radio Transmission and Reception (Release 17) (V17.6.0)" (June 2022).

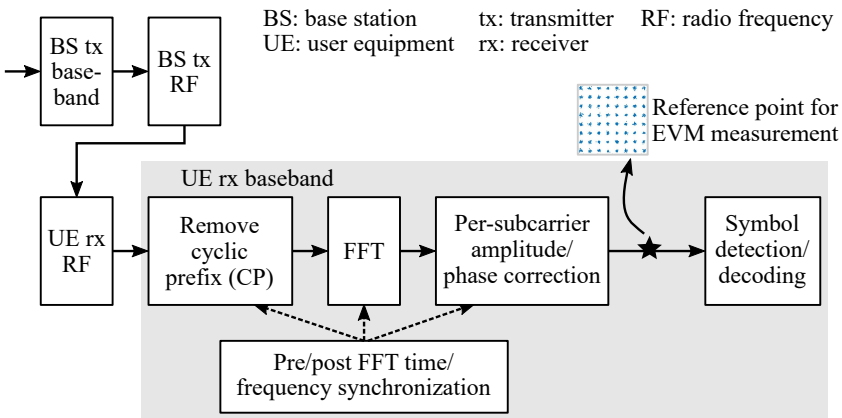

Figure B.1: Reference point for EVM Measurement.

Throughout this dissertation, the provided EVM values are calculated by: (1) calculating the distance between each received constellation point at the reference point ($I_{\mathrm{R},k} + jQ_{\mathrm{R},k}$) and the expected normalized constellation point ($I_k + jQ_k$), (2) calculating the root-mean-square (RMS) value over all data subcarriers and all orthogonal frequency-division multiplexing (OFDM) frames, and then (3) normalizing the value to the average constellation power.

$$\text{EVM (\%)} = \sqrt{\frac{\sum\limits_{\substack{\text{all OFDM}\\ \text{frames}}} \sum\limits_{k \in \mathbf{D}} \left((I_{\mathrm{R},k} - I_k)^2 + (Q_{\mathrm{R},k} - Q_k)^2 \right)}{N \cdot \text{average constellation power}}} \tag{B.1}$$

where k denotes the subcarrier index, $\mathbf{D}$ is the index set of all data subcarriers and N is the total number of collected constellation points. The EVM can also be expressed in dB:

$$\text{EVM (dB)} = 20\log\left(\frac{\text{EVM (\%)}}{100}\right). \tag{B.2}$$

The 3GPP EVM requirements for different modulation schemes are listed in Table B.1.

Modulation scheme	**EVM**	
QPSK	17.5%	(−15.14 dB)
16-QAM	12.5%	(−18.06 dB)
64-QAM	8%	(−21.94 dB)
256-QAM	3.5%	(−29.12 dB)
1024-QAM	2.5%[1]	(−32.04 dB)
	2.8%[2]	(−31.06 dB)

[1] Applicable for frequencies equal to or below 4.2 GHz.
[2] Applicable for frequencies above 4.2 GHz.

Table B.1: 3GPP EVM requirements for different modulation schemes.

C

Derivation of the Expectation of $cos(\phi)$ for $\phi \sim \mathcal{N}(0, \sigma_\phi^2)$

For a Gaussian random variable with zero mean and σ_ϕ^2 variance: $\mathcal{N}(0, \sigma_\phi^2)$, the expecation of $cos(\phi)$ [1] is:

$$\mathrm{E}\left[cos(\phi)\right] = \int cos(\phi) \frac{1}{\sqrt{2\pi}\sigma_\phi} e^{-\frac{1}{2}\left(\frac{\phi}{\sigma_\phi}\right)^2} d\phi \,. \tag{C.1}$$

Also, from the definition of the expectation of a complex random variable [2]:

$$\mathrm{E}\left[e^{j\phi}\right] = \mathrm{E}\left[cos(\phi)\right] + j\,\mathrm{E}\left[sin(\phi)\right] \,, \tag{C.2}$$

it can be derived that:

$$\mathrm{E}\left[cos(\phi)\right] = \mathcal{R}\left[\mathrm{E}\left[e^{j\phi}\right]\right] \,. \tag{C.3}$$

The moment generating function of a Gaussian random variable X is defined as:

$$M_X(t) = \mathrm{E}\left[e^{tX}\right] = \int e^{tx} \frac{1}{\sqrt{2\pi}\sigma_X} e^{-\frac{1}{2}\left(\frac{x-\mu_X}{\sigma_X}\right)^2} dx \tag{C.4}$$

where μ_X and σ_X^2 are the mean and variance of X [1]. Since the Gaussian distribution is the most important distribution, the result of the integral is provided

by [1]:

$$M_X(t) = \mathrm{E}\left[e^{tX}\right] = e^{\mu_X t + \frac{1}{2}\sigma_X^2 t^2} \,. \tag{C.5}$$

Replacing t by j and X by ϕ, Eq. (C.5) can be rewritten as:

$$\mathrm{E}\left[e^{j\phi}\right] = e^{-\frac{1}{2}\sigma_\phi^2} \,. \tag{C.6}$$

Therefore,

$$\mathrm{E}\left[cos(\phi)\right] = \mathcal{R}\left[\mathrm{E}\left[e^{j\phi}\right]\right] = e^{-\frac{1}{2}\sigma_\phi^2} \,. \tag{C.7}$$

References

[1] K. F. Riley, M. P. Hobson, and S. J. Bence, *Mathematical Methods for Physics and Engineering*, Chapter 30: Probability, Third ed. Cambridge University Press, 2006.

[2] K. I. Park, "Characterization of Random Variables," in *Fundamentals of Probability and Stochastic Processes with Applications to Communications*. Switzerland: Springer International Publishing, 2018, pp. 109–133.

D

Impact of Inaccurate Precoding Phases on a 2-by-2 Multi-User MIMO System

Chapter 7 included only the experimental results of a 2-by-1 distributed antenna system (DAS). Therefore, only the derivation based on the two-antenna system was provided in Section 7.2. This appendix analyzes the impact of inaccurate precoding phases on the distributed multi-user multiple-input multiple-output (MU-MIMO) system introduced in Chapter 4. Although the experimental results are not available, the derivation will confirm the importance of phase accuracy.

The derivation starts with the precoding matrix (for each subcarrier) defined by Eq. (4.2):

$$\begin{bmatrix} \mathrm{X}_1 \\ \mathrm{X}_2 \end{bmatrix} = \underbrace{\begin{bmatrix} \alpha & -\beta\frac{\hat{\mathrm{H}}_{21}\hat{\mathrm{H}}_{11}^*}{\hat{\mathrm{H}}_{11}^*\hat{\mathrm{H}}_{11}} \\ -\alpha\frac{\hat{\mathrm{H}}_{12}\hat{\mathrm{H}}_{22}^*}{\hat{\mathrm{H}}_{22}^*\hat{\mathrm{H}}_{22}} & \beta \end{bmatrix}}_{\text{Precoding matrix: } \mathbf{G}} \begin{bmatrix} \mathrm{S}_1 \\ \mathrm{S}_2 \end{bmatrix} \tag{D.1}$$

where X_i is the precoded data to be tranmitted by remote radio unit (RRU) transmitter i; $\hat{\mathrm{H}}_{ij}$ denotes the estimated channel frequency response (CFR) between transmitter i and user j during the latest training phase; S_j is the baseband data—the constellation points—expected to be received by user j; α and β are two real constants that have the same values for all subcarriers in an orthogonal frequency-division multiplexing (OFDM) frame.

The received data can be written as

$$\begin{bmatrix} \mathrm{R}_1 \\ \mathrm{R}_2 \end{bmatrix} = \underbrace{\begin{bmatrix} \mathrm{H}_{11} & \mathrm{H}_{21} \\ \mathrm{H}_{12} & \mathrm{H}_{22} \end{bmatrix}}_{\text{Channel matrix: } \mathbf{H}} \underbrace{\begin{bmatrix} \alpha & -\beta \frac{\hat{\mathrm{H}}_{21}\hat{\mathrm{H}}_{11}^*}{\hat{\mathrm{H}}_{11}^*\hat{\mathrm{H}}_{11}} \\ -\alpha \frac{\hat{\mathrm{H}}_{12}\hat{\mathrm{H}}_{22}^*}{\hat{\mathrm{H}}_{22}^*\hat{\mathrm{H}}_{22}} & \beta \end{bmatrix}}_{\text{Precoding matrix: } \mathbf{G}} \begin{bmatrix} \mathrm{S}_1 \\ \mathrm{S}_2 \end{bmatrix} . \tag{D.2}$$

H_{ij} and $\hat{\mathrm{H}}_{ij}$ are the overall CFRs and the estimated overall CFRs. The values include both the CFRs of the wireless and the hardware paths.

The signal received by user 1 is

$$\mathrm{R}_1 = \underbrace{\alpha \mathrm{S}_1 \left(\mathrm{H}_{11} - \mathrm{H}_{21} \frac{\hat{\mathrm{H}}_{12}\hat{\mathrm{H}}_{22}^*}{\hat{\mathrm{H}}_{22}^*\hat{\mathrm{H}}_{22}} \right)}_{\text{Signal}} + \underbrace{\beta \mathrm{S}_2 \left(\mathrm{H}_{21} - \mathrm{H}_{11} \frac{\hat{\mathrm{H}}_{21}\hat{\mathrm{H}}_{11}^*}{\hat{\mathrm{H}}_{11}^*\hat{\mathrm{H}}_{11}} \right)}_{\text{Interference}} . \tag{D.3}$$

If the downlink CFRs are accurately estimated and used for precoding within the coherence time of the wireless channel,

$$\mathrm{H}_{11} = \hat{\mathrm{H}}_{11}\, e^{j\phi_{11}} \tag{D.4}$$

and

$$\mathrm{H}_{21} = \hat{\mathrm{H}}_{21}\, e^{j\phi_{21}} \tag{D.5}$$

where ϕ_{ij} denotes the change of the phase difference between RRU transmitter i and user j from the moment when $\hat{\mathrm{H}}_{ij}$ is estimated to when the downlink data is transmitted. The time-variant phase differences come from the different frequency sources of the transmitter and receiver. Both the residual carrier frequency offset (CFO) and phase noise can result in the change.

For a co-located antenna system, because the transmitters share the same frequency source, $\phi_{11} = \phi_{21}$. Therefore, the interference part will be zero. For a DAS, the power of the interference depends on how fast the asynchonous phase noise changes between the two separately located transmitters. Only if $\phi_{11} \approx \phi_{21}$, the interference part will be close to zero. This may be achieved by frequently estimating the CFRs, i.e. decreasing the length of the data transmisison phase (Fig. 4.3).

For DASs exploiting time-division duplex (TDD) reciprocity, the workflow consists of three phases as introduced in Fig. 7.3. The calibration coefficients are estimated during the calibration phase. The uplink CFRs are estimated during the training phase. The downlink CFRs, calculated by combining the

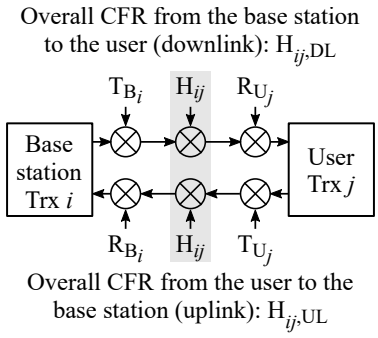

Figure D.1: The overall downlink and uplink channels between a base station transceiver and a user. (CFR: channel frequency response; Trx: transceiver.)

results estimated in the two abovementioned phases, are applied during the data transmission phase. The time duration between each estimation and application is essential. Therefore, different colors are used to mark during which phases the values are estimated: **blue**, **orange**, and **green** correpond to the calibration, training, and data transmission phases, respectively.

According to Eq. (7.21), the (relative) downlink CFRs can be calculated as follows:

$$\begin{aligned} \hat{H}_{11,DL} &= \hat{H}_{11,UL}\, \hat{c}_{1R}\,; \\ \hat{H}_{21,DL} &= \hat{H}_{21,UL}\, \hat{c}_{2R} = \hat{H}_{21,UL}\, \hat{c}_{1R}\, \hat{c}_{21}\,. \end{aligned} \tag{D.6}$$

c_{21} is the relative calibration coefficient between two base station transceivers. As illustrated in Fig. D.1, T, H, and, R denote the CFRs of the transmission (hardware), wireless, and reception (hardware) paths.

$$c_{21} = \frac{T_{B2} \cdot R_{B1}}{T_{B1} \cdot R_{B2}}. \tag{D.7}$$

The interference part of Eq. (D.3) becomes

$$\beta S_2 \left(H_{21,DL} - H_{11,DL} \frac{\hat{H}_{21,UL}\, \hat{c}_{1R}\, \hat{c}_{21}}{\hat{H}_{11,UL}\, \hat{c}_{1R}} \right).$$

$$
\begin{aligned}
&\beta \mathrm{S}_2 \left(\mathrm{H}_{21,\mathrm{DL}} - \mathrm{H}_{11,\mathrm{DL}} \frac{\hat{\mathrm{H}}_{21,\mathrm{UL}}\, \hat{c}_{21}}{\hat{\mathrm{H}}_{11,\mathrm{UL}}} \right) \\
=&\beta \mathrm{S}_2 \left(\mathrm{H}_{21,\mathrm{DL}} - \mathrm{H}_{11,\mathrm{DL}} \frac{\hat{\mathrm{R}}_{\mathrm{B2}}\, \hat{\mathrm{H}}_{21}\, \hat{\mathrm{T}}_{\mathrm{U1}}}{\hat{\mathrm{R}}_{\mathrm{B1}}\, \hat{\mathrm{H}}_{11}\, \hat{\mathrm{T}}_{\mathrm{U1}}}\, \hat{c}_{21} \right) \\
=&\beta \mathrm{S}_2 \left(\mathrm{T}_{\mathrm{B2}}\, \mathrm{H}_{21}\, \mathrm{R}_{\mathrm{U1}} - \mathrm{T}_{\mathrm{B1}}\, \mathrm{H}_{11}\, \mathrm{R}_{\mathrm{U1}} \frac{\hat{\mathrm{R}}_{\mathrm{B2}}\, \hat{\mathrm{H}}_{21}}{\hat{\mathrm{R}}_{\mathrm{B1}}\, \hat{\mathrm{H}}_{11}}\, \hat{c}_{21} \right) \\
=&\beta \mathrm{S}_2\, \mathrm{T}_{\mathrm{B2}}\, \mathrm{R}_{\mathrm{U1}} \left(\mathrm{H}_{21} - \mathrm{H}_{11} \frac{\hat{\mathrm{H}}_{21}}{\hat{\mathrm{H}}_{11}} \boxed{\frac{\mathrm{T}_{\mathrm{B1}}}{\mathrm{T}_{\mathrm{B2}}} \frac{\hat{\mathrm{R}}_{\mathrm{B2}}}{\hat{\mathrm{R}}_{\mathrm{B1}}}}\, \hat{c}_{21} \right)
\end{aligned}
\tag{D.8}
$$

If the uplink CFRs are accurately estimated, and the calculated downlink CFRs are used for precoding within the coherence time of the wireless channel, $\mathrm{H}_{11} \approx \hat{\mathrm{H}}_{11}$ and $\mathrm{H}_{21} \approx \hat{\mathrm{H}}_{21}$.

To suppress the interference, the term in the box must equal $1/\hat{c}_{21,k}$.

$$
\frac{\mathrm{T}_{\mathrm{B1}}}{\mathrm{T}_{\mathrm{B2}}} \frac{\hat{\mathrm{R}}_{\mathrm{B2}}}{\hat{\mathrm{R}}_{\mathrm{B1}}} = \frac{1}{\hat{c}_{21,k}} = \frac{\hat{\mathrm{T}}_{\mathrm{B1}}\, \hat{\mathrm{R}}_{\mathrm{B2}}}{\hat{\mathrm{T}}_{\mathrm{B2}}\, \hat{\mathrm{R}}_{\mathrm{B1}}} \tag{D.9}
$$

As shown by the measurement results of the relative calibration coefficeints ($\hat{c}_{21}$) in Chapter 7 (Fig. 7.4, Fig. 7.5, and Fig. 7.6(b)), only the phase of $\hat{c}_{21,k}$ changes overtime. Therefore, the mismatch between the left and right sides of Eq. (D.9) can be expressed as $e^{j\phi}$ where ϕ denotes the phase change of $\hat{c}_{21,k}$. The interference can be written as

$$
\beta \mathrm{S}_2\, \mathrm{T}_{\mathrm{B2}}\, \mathrm{R}_{\mathrm{U1}}\, \mathrm{H}_{21} \left(1 - e^{j\phi}\right) .
$$

Recall Eq. (D.3). The signal received by receiver 1 is

$$
\mathrm{R}_1 = \underbrace{\alpha \mathrm{S}_1 \left(\mathrm{H}_{11} - \mathrm{H}_{21} \frac{\hat{\mathrm{H}}_{12} \hat{\mathrm{H}}_{22}^*}{\hat{\mathrm{H}}_{22}^* \hat{\mathrm{H}}_{22}} \right)}_{\text{Signal}} + \underbrace{\beta \mathrm{S}_2\, \mathrm{T}_{\mathrm{B2}}\, \mathrm{R}_{\mathrm{U1}}\, \mathrm{H}_{21} \left(1 - e^{j\phi}\right)}_{\text{Interference}} . \tag{D.10}
$$

To provide some numerical approximations, R_1 is simplified as follows:

$$
\mathrm{R}_1 \approx \alpha\, \mathrm{S}_1\, \mathrm{H}_{11} + \beta\, \mathrm{S}_2\, \mathrm{H}_{21} \left(1 - e^{j\phi}\right) . \tag{D.11}
$$

Hence, the error vector magnitude (EVM) caused by the interference can be approximated by

$$\underbrace{\frac{|\beta\,\mathrm{H}_{21}|^2}{|\alpha\,\mathrm{H}_{11}|^2}}_{\text{Power ratio: }\gamma}\left|1-e^{j\phi}\right|^2=\gamma\left(2-2cos(\phi)\right) \tag{D.12}$$

If ϕ is modeled as a Gaussian random variable with zero mean and σ_ϕ^2 variance: $\mathcal{N}(0,\sigma_\phi^2)$, the expectation of Eq. (D.12) with respect to σ_ϕ^2 is:

$$\mathrm{E}\left[\gamma\left(2-2cos(\phi)\right)\right]=2\gamma\left(1-e^{-\frac{1}{2}\sigma_\phi^2}\right). \tag{D.13}$$

Appendix B provided the derivation. The EVM is related to both the variance of the phase change and the power differences between the main serving transceiver(s) and the rest.

Fig. D.2 plots Eq. (D.13) versus different σ_ϕ. Compared with the impact on the digital beamforming performance (Fig. 7.1), the phase accuracy is definitely more critical for interference suppression.

For two scenarios, with directly connected reference clocks and with back-to-back optical connections, the measured σ_ϕ are 4.53° and 12.97°. Even with directly connected reference clocks, the interference suppression for the 2-by-2 MU-MIMO system is only good enough for 64-QAM. With the optical links,

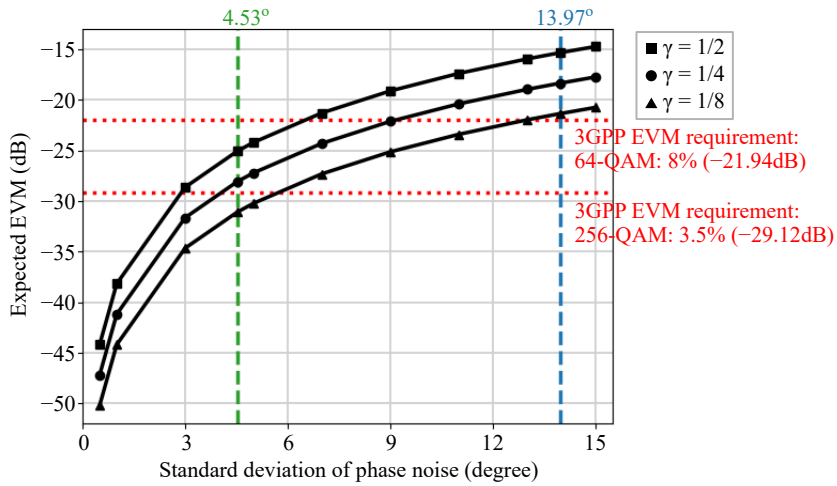

Figure D.2: Expectation of the approximated EVM (dB) caused by the interference versus the stadard deviation of ϕ (degree).

64-QAM transmission is only possible when γ is small, i.e. when each user is close to a different RRU and far from the other RRU. However, for hot-spot scenarios, multiple users are expected to be close to each other. Therefore, γ may be larger than 1/2.

If σ_ϕ is too large, the performance penalty brought by the distributed scheme may be larger than the gain owing to spatial diversity. In conclusion, to enable distributed MIMO and exploit TDD reciprocity, it is necessary to have a more strict phase noise requirement.